A Versatile Design Framework for Stable Reconfigurable Structures with Efficient Actuation

by

Maria Redoutey

A dissertation submitted in partial fulfillment
of the requirements for the degree of
Doctor of Philosophy
(Civil Engineering)
in the University of Michigan
2023

Doctoral Committee:

Assistant Professor Evgueni T. Filipov, Chair
Professor Jason McCormick
Associate Professor Jeffrey Scruggs
Professor Kon-Well Wang

Maria Redoutey
mariared@umich.edu
ORCID iD: 0009-0003-5617-9134

DEDICATION

Dedicated to my younger self

ACKNOWLEDGMENTS

First, I would like to acknowledge my PhD advisor, Professor Evgueni Filipov. Thank you for taking a chance on me as an undergraduate in the SURE program and again as a graduate student. You have been instrumental in helping me build my technical knowledge, research skills, and confidence over the years. Your support as I navigated graduate school and moving to Seattle has been invaluable. Thank you for supporting the lives of the DRSL students in the lab and outside of it - we are lucky to have you as our advisor!

Thank you also to my committee: Prof. Jason McCormick, Prof. Jeffery Scruggs, and Prof. Kon-Well Wang. Your insights helped shape this dissertation into what it is today, and it is much stronger for it!

Mom, Dad, Jenny, and Kristin, thank you for believing in me as I pursued this PhD, even if you didn't always know exactly what it entailed – most of the time, I didn't know either! I'm so grateful to have our family as my anchor as I grow my career and explore the world. I love you all very much!

Thank you also to my future in-laws, Lori-Beth and Dieu, and the whole Hua family for your constant support and enthusiasm. From the time I was accepted into graduate school, you celebrated my progress with all-caps emails and family text chains every step of the way and it means so much to me.

Special shoutout to my cousin Rob for always keeping up with my research - no matter how many times I switched projects! Love you Bobby!

Thank you to Dr. LZ Hershey, for paving the way through a PhD, and David, for paving the way through life in general. My grad school years in Ann Arbor and Seattle were infinitely better because of you two! (And the total hours of board games we played just might rival the hours I spent doing research. . .)

Alyssa B., Alyssa C., Elizabeth, Haley, Heidi, Kayla, Lauren, and Sophia: I'm so grateful to have such a powerhouse group of girls to lean on. Here's to 4/6 doctorates completed!!

To the DRSL group: thank you Steven, Wo, and Yi for letting me follow in your footsteps and for setting the bar so high. Hardik, thanks for being such a friendly face, especially at conferences this year. Yutong and Mira, I enjoyed learning from you and the knowledge you brought in from your respective programs. Anan, Anvay, Jacob, Kaley, and Wayne, it has been wonderful getting to know you this year. I trust that I am leaving the group in great hands! I also want to acknowledge the undergrads and visitors I got to work with throughout the past five years, especially Addy, Ann, Ariel, Bin, Bini, and Fekadu.

To my cats, Goose and Shark, for their consistent love and demands for attention no matter how my research was going that day.

Finally, thank you to my fiancé, Mike Hua. Most of this dissertation research was done while we were working from home together, sharing a home office. I will always treasure the memories of us working through research problems together, sharing in each other's triumphs (pretty MATLAB plots) and struggles (reviewer comments). I'm so happy I found a partner who will discuss potential energy gradients over pina coladas by the pool with me. You have been my biggest hype man since day one and I couldn't have weathered the ups and downs of the PhD without you. I'm so grateful that you encourage my ambition and also encourage me to rest when I need it. Thank you for taking us on our Seattle adventure – I can't wait to see where else life takes us! Now pronouncing… the Drs. Hua!

TABLE OF CONTENTS

LIST OF FIGURES

FIGURE

LIST OF TABLES

TABLE

LIST OF VIDEOS

VIDEO

ABSTRACT

Structures that move, deploy, and reconfigure offer many advantages, such as advanced functionality, the ability to stow and transport, and adaptability. Despite these advantages, traditional civil engineering structures such as bridges, shelters, and domes are not typically designed to reconfigure, due to several challenges that arise when designing at a civil engineering scale. These challenges include that the effect of gravity can hinder the actuation of a reconfigurable structure, the inherent flexibility of structures with multiple degrees of freedom (DOFs), and the difficulty of ensuring stability and stiffness in the final deployed state. This dissertation explores the design of reconfigurable structures to address these challenges and make the structures feasible for use at a civil engineering scale.

First, an open-source design framework for reconfigurable structures that are stable under gravity at any global orientation is established. Optimization is used to design springs that offset the potential energy due to gravity and transform reconfigurable structures into systems with *continuous equilibrium*. One set of springs can be designed to maintain continuous equilibrium, even when the structure is reoriented with respect to a global reference frame. Next, the design framework is extended to systems with more than one DOF. The spring properties are computed such that the multi-DOF system follows a specific motion path while remaining globally stable and in continuous equilibrium. Next, the practical implementation of continuous equilibrium structures in real-world applications is discussed. Mechanical models and physical prototypes are used to investigate the behavior of continuous equilibrium structures, and a reduction in actuation forces is observed when springs are used to counteract gravity. Finally, a novel dome-like reconfigurable structure is introduced. Despite having multiple DOFs, this structure has a unique infinitesimal mechanism which allows it to deform into a dome-like shape with high out-of-plane stiffness. The optimization framework is used to design the dome-like structure to have continuous equilibrium, making it stable under gravity and reducing the forces needed for deployment.

This dissertation presents methods for designing reconfigurable structures to have lower actuation forces, inherent stability, and robust stiffness. These methods are of importance in scenarios where gravity cannot be neglected, and in particular to the realization of large deployable and reconfigurable structures at the civil engineering scale.

CHAPTER 1

Introduction

Reconfigurable structures are systems with components that move, or *reconfigure*, along a prescribed path in order to achieve one or more functions. They are versatile and offer benefits in many fields, including civil engineering. Civil engineering scale reconfigurable structures, such as a retractable roof (Figure 1.1(A)) or deployable pedestrian bridge (Figure 1.1(B)) can enable the multi-purpose use of a space. Reconfigurable components can be incorporated into building facades and change in response to the environment, adjusting the amount of sunlight let into the building (Figure 1.1(C)).

For decades, research has focused on the kinematics, mobility, and stress states of reconfigurable structures [1, 2, 3, 4]. A fundamental challenge that remains is actuating them efficiently while preserving stiffness and stability, especially in applications where gravity has a significant effect, as it does for in civil engineering structures. In many cases, reconfiguration requires a large input of energy, resulting in inefficient, over-designed, and costly structures that are impractical to fabricate and operate.

In this dissertation, a framework is introduced to design structures that maintain stability as they *reconfigure* though their kinematic path and are *reoriented* with respect to a global reference frame. The method involves computing properties of springs that directly offset the potential energy due to gravity. Systems designed using this framework do not collapse due to gravity and can move along their kinematic path with only a small input force.

1.1 Linkage Systems

Linkages are reconfigurable structures consisting of rigid links connected by revolute pin joints. Such systems are used widely in engineering to transmit forces and enable complex motions. The simplest type of linkage is the planar four-bar linkage. Four-bar linkages are ubiquitous in engineering, found in robotics [6], biomechanics and bio-inspired design [7, 8, 9], automotive steering [10], surgical instruments [11], and many other fields. A planar four-bar linkage consists of four

Figure 1.1: Examples of civil-scale reconfigurable structures. (A) The retractable roof of Mercedes-Benz Stadium in Atlanta, GA. (B) Heatherwick's rolling bridge in London [5]. (C) The adaptive facade of the Al Bahr towers in Dubai.

rigid members connected with pinned joints, resulting in a one-DOF mechanism [12]. Although the kinematics [13, 14, 15], dynamics [16, 17], design [18], and inertia loads [19, 20] of four-bar linkages have been studied, the effect of gravity and self-weight on their mechanics is rarely considered in the literature. Static balancing of four-bar linkages involves counteracting gravity with springs, but previous approaches to static balancing are limited to specific linkages in a static orientation [11, 21, 22, 23]. Linkages made up of scissorlike elements (SLEs), or pantographs, are often used to create structures that deploy from a compact state [24, 25], such as a platform scissor lift (Figure 1.2(A)). Bipedal robots mimic the motion of human limbs and joints using linkages (Figure 1.2(B)). Some linkages can serve as a frame for a curved surface, such as the Bennett linkage (Figure 1.2(C)) and the Hoberman Sphere (Figure 1.2(D)). Linkages are essential in automotive design, where they are used in applications such as steering (Figure 1.2(E)).

1.2 Origami and Kirigami Systems

In recent years, origami has emerged as a way to rapidly assemble complex structural geometries from flat sheets [30, 31]. Origami-inspired reconfigurable structures are comprised of panels made from thin sheets connected by flexible crease lines. Origami principles are also scale independent, viable at the micro-scale in systems such as grippers [32, 33, 34, 35] (Figure1.3(A)), and at a civil engineering scale in systems such as deployable canopies [30, 36, 37] (Figure 1.3(B)). Assembling

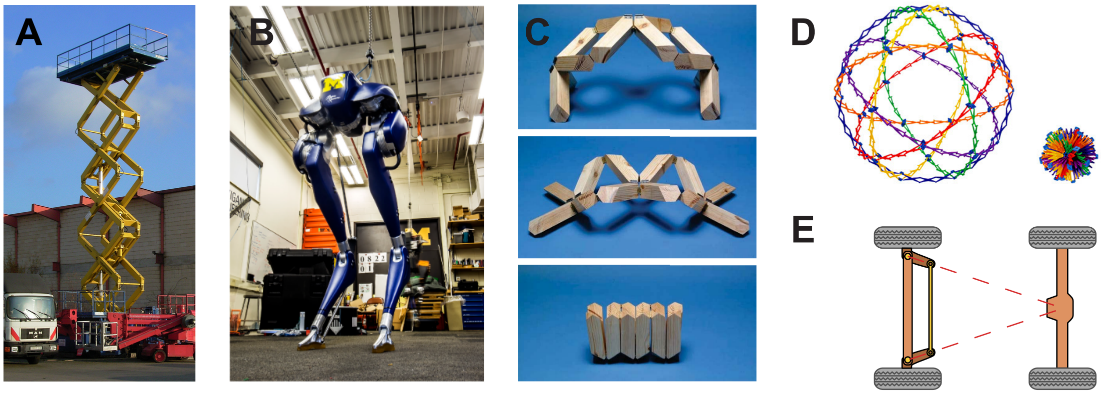

Figure 1.2: Examples of linkage-based reconfigurable structures. (A) A scissor lift [26]. (B) Bipedal Cassie robot [27]. (C) Bennett linkage [28]. (D) Hobermann sphere. (E) Ackermann steering linkage [29].

structures out of thin, flat sheets can also simplify the fabrication of complex structures, such as walking robots [38] (Figure 1.3(C)). Foldable structures inspired by origami and designed using engineering principles can be deployed quickly from compact or stowed configurations [39, 40, 41], as seen in the design of a deployable solar array which deploys in orbit [42] (Figure 1.3(D)). Kirigami, a related discipline where cuts are used in addition to folding, has been an inspiration for novel metamaterials [43], crawling robots [44], inflatables with programmed shapes [45], and pop-up dome-like structures [46] (Figure 1.3(E)).

Several challenges arise when fabricating origami-based structures at a civil engineering scale. First, it is difficult to reach high stiffness using origami and kirigami methods, because thin sheets are prone to bending and folding. Origami-based systems are inherently flexible due to their high number of degrees of freedom, and external supports or locking are often required to create load-bearing structures. Additionally, accommodations must be made for the finite thickness of structural materials in order to achieve the desired folding motions [47, 48]. Thin-sheet origami can be used to achieve complex geometries, such as curved surfaces [49], but many methods used are not viable for materials with significant thickness.

1.3 Multi-DOF Systems

Systems with multiple degrees of freedom (multi-DOFs) are multi-functional structures with applications in a wide variety of fields. Multi-DOF structures have a range of motion associated with each DOF, which allows for drastic and functional change in the geometry, as seen when an excavator digs and transports material (Figure 1.4(A)). Multiple DOFs can also enable complex

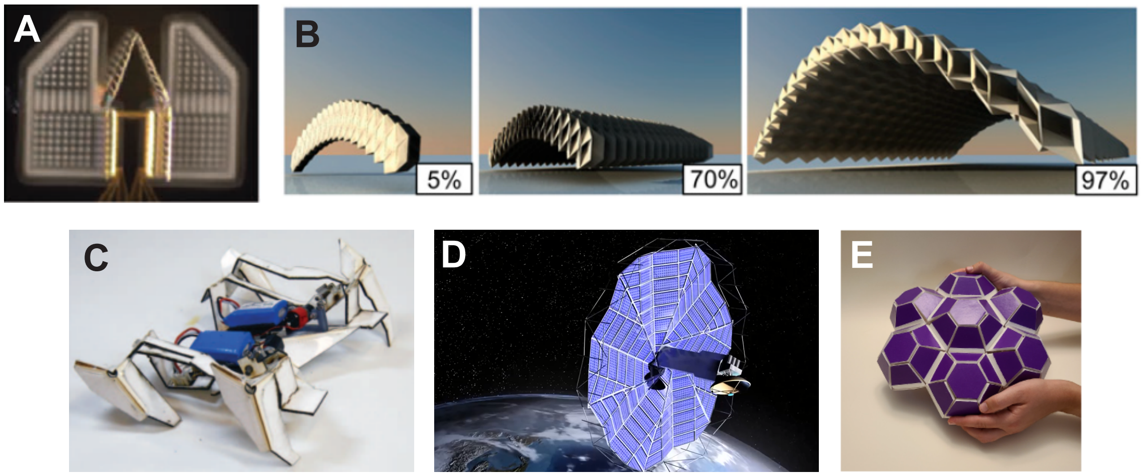

Figure 1.3: Examples of origami-based reconfigurable structures. (A) An origami micro-gripper [32]. (B) A deployable canopy consisting of Miura-ori zipper tubes [30]. (C) A centimeter-scale robot, fabricated from a flat sheet and assembled using origami principles [38] (D) A solar array designed to be deployed in orbit [42]. (E) A pop-up kirigami dome [46].

and varied motions, as seen in robotic arms that can stretch, bend, twist, and grasp objects (Figure 1.4(B)). Multi-DOF systems can also consist of one-DOF components connected in parallel, achieving multi-DOF motion as they work together, such as in the 6-DOF Stewart platform (Figure 1.4(C)). Mechanical metamaterials have also been fabricated to have multiple DOFs, leading to tunability in shape and stiffness [50] (Figure 1.4(D)). Multi-DOF systems are also found in robotic exoskeletons [51], space-saving furniture [52], in next-generation aircraft [53], and more.

From a technical perspective, while one-DOF systems have only one kinematic path, adding even a single other DOF results in a system with infinite paths for possible reconfiguration. As such, multi-DOF systems with a range of motion associated with each DOF have a kinematic space with dimension n for an n-DOF system. While multi-DOF reconfigurable structures offer enhanced motions and functionality, their implementation is hindered by two main challenges. First, the effect of gravity acting on these reconfigurable structures can result in destabilizing effects with unwanted motions (or even collapse), so counteracting gravity requires costly, complex, and inefficient actuation systems. Second, while infinite configurations are possible with multi-DOF systems, obtaining motion along a desired path or in a particular sequence is often difficult, requiring dedicated control to ensure motion and stability.

Programming motions into a multi-DOF reconfigurable structure allows certain paths to be favored and prohibits motion along unwanted directions. Programming can be achieved using discrete components, such as magnets and springs, or through continuous factors such as strain [57]. One type of motion path programming is self-assembly, which is often realized using origami-

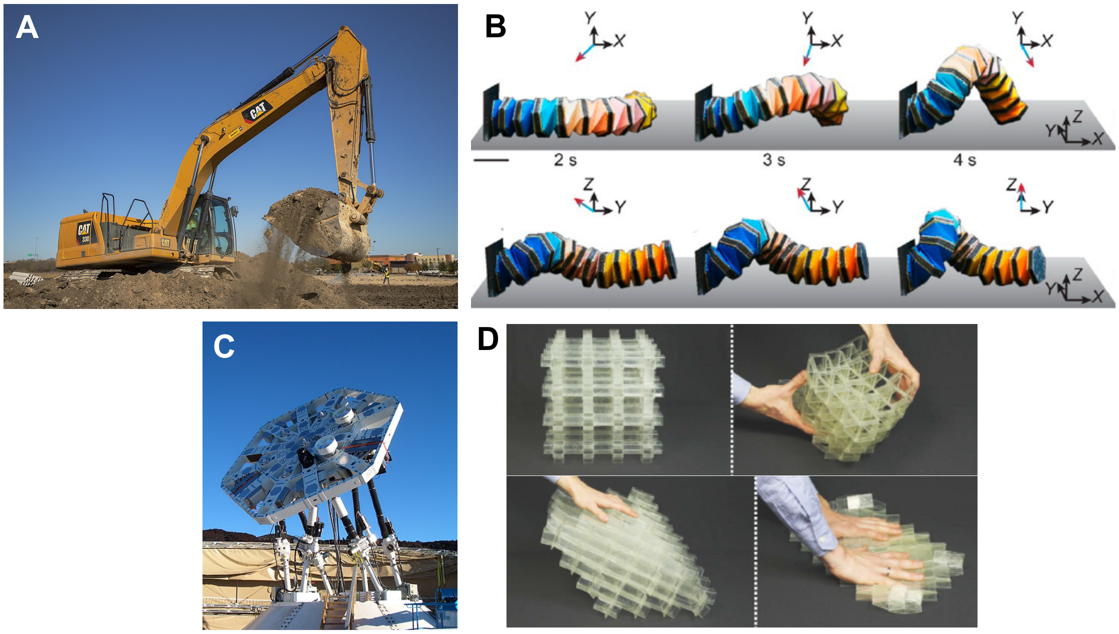

Figure 1.4: Examples of multi-DOF reconfigurable structures. (A) A construction excavator [54]. (B) A robotic arm that can stretch, bend, twist, and grasp objects [14]. (C) A 6-DOF Stewart platform [55]. (D) A mechanical metamaterial with tunable shape and stiffness [56].

inspired designs [34, 58, 59]. At the micro-scale, residual stresses [33, 60], thermal and chemical stimuli [61], hydrogel swelling [62], and Joule heating [32] combined with origami design principles have been shown to enable self-folding. Motion paths can also be programmed into reconfigurable structures through purposeful self-contact [63]. In soft material systems, shape programming has been achieved using stimuli-responsive materials [64, 65], and compressive buckling [66]. Most of these techniques are not viable beyond the micro-scale because gravity causes unwanted deformations in soft materials [67] and the forces developed for self-folding are not large enough to overcome gravity. Additionally, fabrication methods such as lithography are not applicable for the large components needed to build reconfigurable structures at a civil-engineering scale.

1.4 Continuous Equilibrium

Continuous equilibrium systems are a subset of reconfigurable structures with a kinematic mode that allows them to reconfigure with a negligible input of energy. Continuous equilibrium is also described as neutral stability or zero stiffness, and is characterized by a constant potential energy curve throughout reconfiguration [68, 69, 70]. Advantages of systems with continuous equilibrium

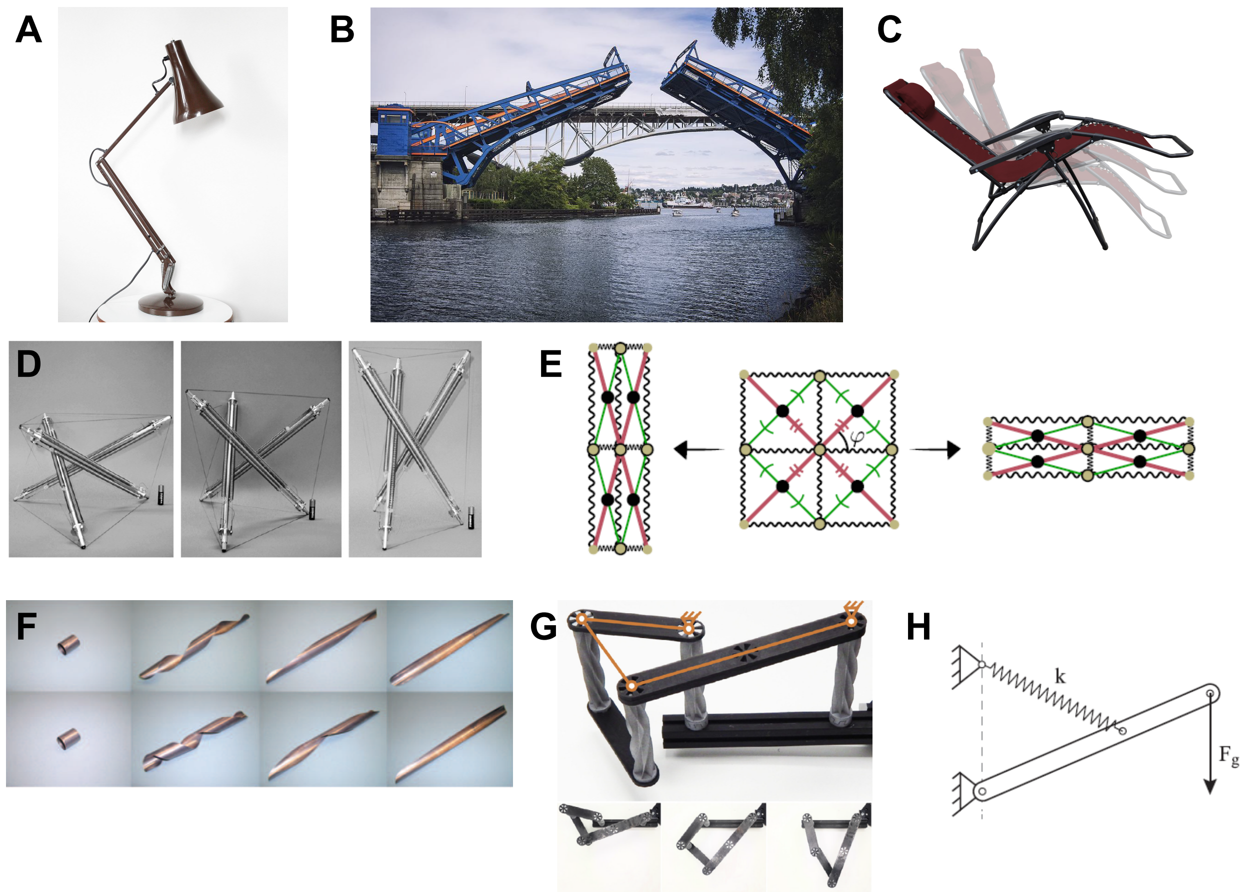

Figure 1.5: Examples of continuous equilibrium systems. (A) Anglepoise desk lamp [71]. (B) Fremont bascule bridge in Seattle, WA [72]. (C) Zero-gravity recliner [73]. (D) Zero-stiffness tensegrity structure [74]. (E) Totimorphic assemblies [75]. (F) Neutrally stable cylindrical shell [76]. (G) Reconfigurable linkage made with neutrally stable helicoidal shell joints [77]. (H) A simple statically balanced system [70].

include low energy required for actuation and an inherently stable reconfiguration path that avoids instabilities and dynamic snap-through behaviors.

Under gravity, most reconfigurable structures do not have a constant potential energy curve; rather, the potential energy is affected by gravity as the structure moves through its kinematic path. The potential energy curve of a system is also affected by elements such as counterweights, springs, or magnets [57, 78]. Continuous equilibrium is attained when the potential energy contributions of these components offset the potential energy due to gravity. Examples include the Anglepoise desk lamp, in which pre-stressed springs allow the lamp to be easily repositioned [79] (Figure 1.5(A)), bascule bridges which utilize a counterbalance to open [80, 81] (Figure 1.5(B)), and chairs which can be easily adjusted to recline at any angle [73] (Figure 1.5(C)).

Continuous equilibrium has been attained in structures through the addition of springs, where the potential energy of the springs counteract each other and large shape changes can occur [74, 75] (Figure 1.5(D-E)). Structures can be designed to match a prescribed energy landscape (including a landscape corresponding to continuous equilibrium) by numerically computing the appropriate spring properties [43] An initial plastic deformation can also be used to imbue pre-stress into material [76, 82], such as a cylindrical shell that is stable as it unwinds and winds again in the opposite direction (Figure 1.5(F)). Coupled components with offsetting deformations can also be used to achieve continuous equilibrium [83, 77], particularly in the design of linkage joints (Figure 1.5(G)). A temperature gradient [84] or thermal residual stresses [85] have also been used to obtain continuous equilibrium. Despite these examples, there is currently no comprehensive framework to transform structures into systems with continuous equilibrium while considering gravity. In most previous studies, gravity has been ignored, systems are trivial to design (such as the simple rigid link shown in Figure 1.5(H)), are designed by trial and error, or only achieve continuous equilibrium for a small range of motion [70]. Additionally, all previous work has focused on achieving continuous equilibrium in only one specific orientation. If the entire structure is *reoriented* with respect to the ground (thus changing the potential energy curve due to gravity), continuous equilibrium is not maintained. Finally, continuous equilibrium has not been explored for origami structures or systems with multiple DOFs.

1.5 Scope of Thesis

In this dissertation, we present a framework to design structures that maintain continuous equilibrium as they *reconfigure* though their kinematic path and are *reoriented* with respect to a global reference frame. The method involves using optimization to compute properties of springs that directly offset the potential energy due to gravity. The open-source computer codes used to generate the results presented in Chapters 2 and 3 are made available on GitHub. The dissertation is organized as follows:

Chapter 2 introduces the design framework for transforming reconfigurable structures into systems with continuous equilibrium. We first use planar four-bar linkages to demonstrate our method. We formulate an objective function that minimizes the fluctuation in potential energy over the entire kinematic path. When torsional springs are added to the linkages, the total potential energy curve is flattened and continuous equilibrium is attained. The framework can be used to design structures that maintain continuous equilibrium even as the system is reoriented with respect to a global reference frame. We explore the effects of four types of springs: torsional, extensional, internal, and external, investigate the effect of symmetry on the final total potential energy curve, and establish guidelines for choosing the most effective spring types. Finally, we expand the framework to the design of more complex structures that carry external loads and to a three-dimensional origami arch.

Chapter 3 expands the continuous equilibrium design framework to systems with more than one DOF. First, we use the framework to design Watt's linkages with one-, two-, and three-DOFs that are in continuous equilibrium throughout their entire kinematic space. Next, we explore various ways to program motions in multi-DOF systems using the principle of continuous equilibrium. The result is systems that have continuous equilibrium along desired motion paths which are globally stable. Multiple paths can be programmed, along with stable configurations, for sequential motion. We conclude this chapter with design examples where the framework is used to design more complex multi-DOF structures.

Chapter 4 discusses considerations for the practical implementation of continuous equilibrium reconfigurable structures. We use mechanical models to quantify the forces required for reconfiguration under gravity when optimized springs are added. These concepts are demonstrated further through the fabrication of physical models. In this chapter we discuss the fabrication methods used and some preliminary results from experimental testing.

Chapter 5 presents a culminating example of a reconfigurable, three-dimensional, multi-DOF system: a novel pop-up, dome-like kirigami structure. The structure is made from flat panels and can be fabricated with thickness. When deployed, it forms a domed surface that has high stiffness. We discuss variations of the geometry of the initial kirigami pattern and perform a parametric study to investigate the effect on the final dome-like structure. Next, we use an established mechanism analysis method to identify the internal mechanism that results in the dome-forming motion. By activating the dome-forming motion, all other flexible deformation modes are eliminated, and the result is a structure with high stiffness. A stiffness analysis shows that the structure has 1,000 to 5,000 times higher stiffness as compared to a singly-curved sheet with the same material thickness. Finally, the design framework presented in chapters 2 and 3 is used to design the pop-up dome with continuous equilibrium.

Chapter 6 concludes the dissertation with a discussion of the main findings and outlines areas for future work.

CHAPTER 2

Designing Continuous Equilibrium Structures that Counteract Gravity in any Orientation

This chapter presents a framework to transform reconfigurable structures into systems with continuous equilibrium. The method involves adding springs that counteract gravity to achieve a system with a nearly flat potential energy curve. The resulting structures can move, or *reconfigure*, effortlessly through their kinematic paths and remain stable in all configurations. Remarkably, the framework can design systems that maintain continuous equilibrium during *reorientation*, so that the system maintains a nearly flat potential energy curve even when it is rotated with respect to a global reference frame. This ability to reorient while maintaining continuous equilibrium enhances the versatility of deployable and reconfigurable structures by ensuring they remain efficient and stable for use in different scenarios. In this chapter, the framework is applied to several planar linkages and the effect of spring placement, spring types, and system kinematics on the optimized potential energy curves is explored. Next, the generality of the method is demonstrated through more complex linkage systems that carry external masses and with a three-dimensional origami-inspired deployable structure. The framework introduced in this chapter enables the stable and efficient actuation of reconfigurable structures under gravity, regardless of their global orientation. These principles have the potential to revolutionize the design of robotic limbs, retractable roofs, furniture, consumer products, vehicle systems, and more.

The work presented in this chapter is adapted from [86].

2.1 Introduction

In this chapter, we present a framework to design structures that maintain continuous equilibrium as they *reconfigure* though their kinematic path and are *reoriented* with respect to a global reference frame. The method involves using optimization to compute the properties of springs that directly offset the potential energy due to gravity. We first discuss the optimization setup used to find

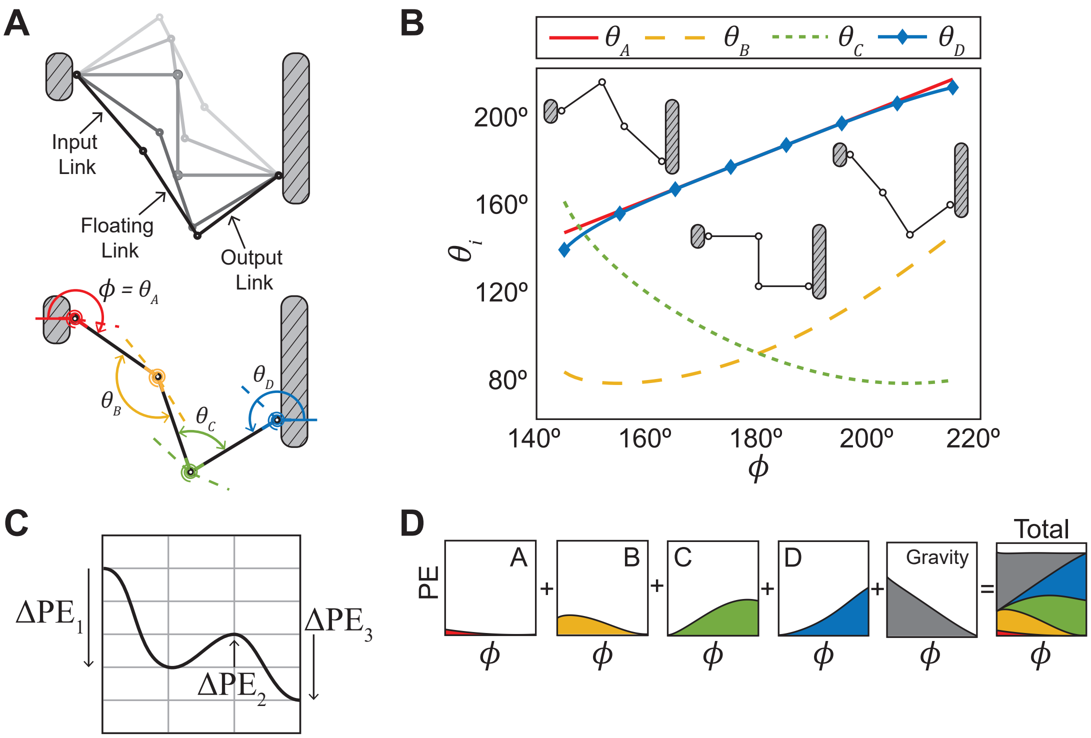

Figure 2.1: Designing the Watt's linkage to have continuous equilibrium. (A) The kinematics of the linkage are defined by the angle of the input link ϕ. We define four locations for torsional springs, with angles $\theta_A, \theta_B, \theta_C$, and θ_D. (B) The angles of the four springs vary with ϕ. (C) Illustration of the fluctuation in potential energy for an arbitrary PE_T curve. The fluctuation is equal to $\Delta PE_1 + \Delta PE_2 + \Delta PE_3$. (D) Potential energy contributions of four internal torsional springs (A, B, C, and D). When the spring contributions are summed with the contribution from gravity, the fluctuation of the potential energy curve is reduced.

spring properties that transform a simple linkage into a continuous equilibrium system. Next, we explore how continuous equilibrium can be maintained as systems are reoriented with respect to a global reference frame. Finally, we apply the method to more complex systems and demonstrate how it can be used to design practical structures. The computer codes used to generate the results presented in this chapter are provided on GitHub.

2.2 Potential Energy of a Four-bar Linkage

A four-bar linkage is a simple reconfigurable mechanism used in many engineering fields. The four-bar linkage that we focus on in depth is the Watt's linkage. This variation of the Watt's linkage consists of three bars of equal length (the imaginary fourth "bar," or fixed link, connects the two support nodes). The four bars are identified as the input link, output link, coupler (floating) link, and ground (fixed) link, which is an imaginary bar connecting the two support nodes (Figure 2.1(A)). The left end of the input link is pinned one bar length above the right end of the output link. The kinematics of the Watt's linkage are defined by the angle ϕ, and we consider only a section of the kinematic path: $\phi_{min} = 145° \leq \phi \leq \phi_{max} = 215°$ (Figure 2.1(B)). We focus on this range of ϕ because within this range, the midpoint of the floating link traces a nearly straight vertical path, a property which is exploited in applications such as vehicle suspension systems. In this dissertation, we limit the kinematics of all linkages to a range where no link rotates a full 360° with respect to an adjacent link.

The potential energy of a bar i due to gravity is defined as $\mathrm{PE}_{\mathrm{G}i}(\phi) = m_i * g * h_i(\phi)$, where m_i is the mass of bar i, $g = 9.81$ m/s^2, and h_i is the height of the center of mass of bar i. The height is computed from a reference point 1 m below the support point of the output link. As the linkage moves through its kinematic path, the height of each bar changes, and so does the potential energy due to gravity; thus, $\mathrm{PE}_{\mathrm{G}i}$ is a function of ϕ. We assume the bars of all linkages have a length of 0.3 m and a uniform mass distribution of 1 kg/m unless otherwise noted.

Our approach to achieving continuous equilibrium is to offset the potential energy due to gravity by adding springs, thus resulting in a **flat total potential energy curve.** We first add a torsional spring *j*, which has a linear stiffness k_j (units: N-m/rad) and a rest angle α_j (units: rad). The potential energy contribution of a torsional spring j is $\mathrm{PE}_{\mathrm{S}j}(\phi) = \frac{1}{2}k_j(\theta_j(\phi) - \alpha_j)^2$. The potential energy in the spring is zero when the current angle of the spring θ_j is equal to the rest angle α_j.

For a given configuration (ϕ), the total potential energy of a linkage system with n bars and m springs is expressed as

$$\mathrm{PE}_{\mathrm{T}}(\phi) = \sum_{i}^{n} \mathrm{PE}_{\mathrm{G}i}(\phi) + \sum_{j}^{m} \mathrm{PE}_{\mathrm{S}j}(\phi). \tag{2.1}$$

For an ideal system in continuous equilibrium, the PE_{T} curve is perfectly flat. To quantify the "flatness" of the total potential energy curve, we first compute the change in potential energy along the kinematic path, expressed as

$$\Delta\mathrm{PE}_{\mathrm{T}} = \frac{d\,\mathrm{PE}_{\mathrm{T}}(\phi)}{d\phi}. \tag{2.2}$$

To compute the total change in potential energy, we integrate the absolute value of the difference along the kinematic path, expressed as

$$\Sigma\left|\Delta\mathrm{PE}_{\mathrm{T}}\right| = \int_{\phi_{min}}^{\phi_{max}} \left|\frac{d\,\mathrm{PE}_{\mathrm{T}}(\phi)}{d\phi}\right| d\phi. \tag{2.3}$$

The quantity $\Sigma|\Delta\mathrm{PE}_{\mathrm{T}}|$ is a measure of the fluctuation in the PE_{T} curve, where $\Sigma|\Delta\mathrm{PE}_{\mathrm{T}}| = 0$ corresponds to a perfectly flat line. Figure 2.1(C) illustrates how $\Sigma|\Delta\mathrm{PE}_{\mathrm{T}}|$ is calculated.

2.3 Optimizing Spring Properties for Continuous Equilibrium

We aim to minimize the $\Sigma|\Delta\text{PE}_\text{T}|$ of a system by finding appropriate spring properties (stiffnesses and rest angles) that result in springs that counteract the effect of gravity. To compute the spring properties, we minimize the $\Sigma|\Delta\text{PE}_\text{T}|$ using the MATLAB function **fmincon**. We identify four possible locations for internal torsional springs on the Watt's linkage, labelled A, B, C, and D in Figure 2.1(A). The design parameters for the optimization problem are the four spring stiffnesses (k_A, k_B, k_C, k_D) and four rest angles ($\alpha_A, \alpha_B, \alpha_C, \alpha_D$). The lower bound for the stiffness terms is 0 N-m/rad, and the range for the rest angle α_j is limited to the range of the corresponding angle θ_j (Figure 2.1(B)). There are no additional constraints placed on the optimization problem, which is expressed as

$$\begin{aligned} &\min \left(\sum \left|\Delta\text{PE}_\text{T}(\phi)\right|\right) \\ &\text{s.t.} \quad k_j > 0 \\ &\qquad\ \alpha_j \in [\theta_{j\text{min}}, \theta_{j\text{max}}]. \end{aligned} \tag{2.4}$$

The result of the optimization for the Watt's linkage with internal torsional springs at all four locations is shown in Figure 2.1(D). The individual plots show the potential energy contributions of each spring and the total PE plot shows the aggregate result of all contributions, including gravity. The optimized spring parameters are $k_A = 0.396$ N-m/rad, $\alpha_A = 199°$; $k_B = 1.18$ N-m/rad, $\alpha_B = 142°$; $k_C = 1.23$ N-m/rad, $\alpha_C = 158°$; and $k_D = 2.04$ N-m/rad, $\alpha_D = 139°$. Qualitatively, the potential energy curve due to bar gravity appears flattened with the addition of the potential energy stored in the springs. Quantitatively, we compare the optimized $\Sigma|\Delta\text{PE}_\text{T}|$ to the same measure considering only gravity, $\Sigma|\Delta\text{PE}_\text{G}|$. The $\Sigma|\Delta\text{PE}_\text{G}| = 2.07$ is reduced to $\Sigma|\Delta\text{PE}_\text{T}| = 0.065$ with the addition of springs; the fluctuation in PE_T curve is reduced by 96.9% from the fluctuation in the PE_G curve.

We compare all possible combinations of springs at locations A, B, C, and D that can be used in the design of the Watt's linkage (Figure 2.2(A)). Certain combinations are more effective than others at flattening the potential energy curve. For example, when designing the linkage with only a single spring, placing the spring at location D reduces $\Sigma|\Delta\text{PE}_\text{T}|$ more than placing it at locations A or B (Figure 2.2(B)). As a result, when designing a linkage with more than one spring, the stiffness of springs A and B approach zero for combinations AD, BD, and ABD; the same $\Sigma|\Delta\text{PE}_\text{T}|$ can be achieved by placing a spring only at location D. Combination BCD offers effectively the same level of reduction as using all four springs. Results for all combinations are included in Table 2.1.

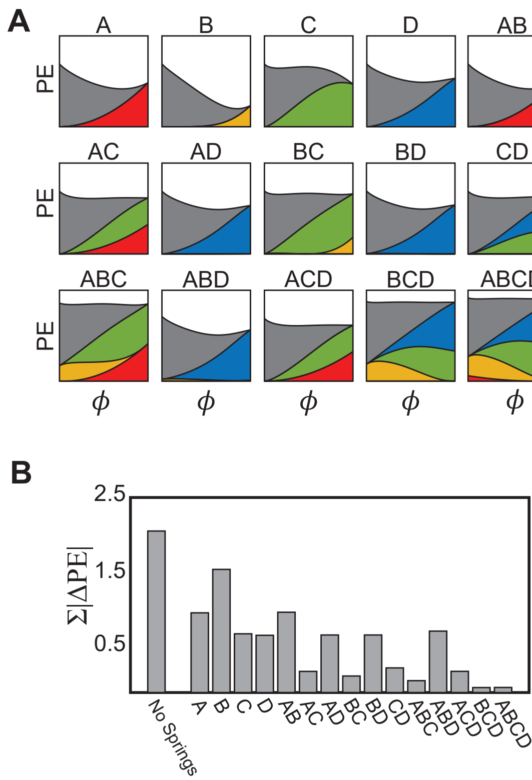

Figure 2.2: Comparing internal torsional spring locations on the Watt's linkage. (A) Optimized potential energy curves for all possible combinations of internal torsional springs added to the Watt's linkage. Placing springs at only locations B, C, and D is as effective as using all four springs. (B) Bar graph of the measure of the fluctuation in potential energy, $\Sigma|\Delta PE_T|$, for each spring combination case.

Table 2.1: Spring properties and $\Sigma|\Delta PE_T|$ values for all possible location combinations of internal torsional springs on the Watt's linkage.

	Rest Angle				Stiffness [N-m/rad]				
	α_A	α_B	α_C	α_D	k_A	k_B	k_C	k_D	$\Sigma\|\Delta PE_T\|$ [N-m]
No Springs									2.07
A	145.2°				1.96				1.03
B		76.9°				1.02			1.58
C			159.2°				1.40		0.75
D				137.5°				1.93	0.73
AB	146.1°	115.8°			2.01	0.071			1.06
AC	145.2°		159.2°		1.32		0.87		0.27
AD	168.5°			138.3°	0.072			1.93	0.77
BC		88.6°	158.7°			1.17	1.44		0.21
BD		130.3°		137.5°		0.031		1.95	0.74
CD			158.8°	137.8°			0.73	1.33	0.32
ABC	159.8°	133.3°	156.7°		2.18	1.40	1.75		0.19
ABD	168.4°	130.2°		137.5°	0.014	0.030		1.94	0.74
ACD	145.2°		159.2°	153.4°	1.31		0.866	0.0084	0.27
BCD		141.4°	157.8°	138.7°		1.01	1.01	2.00	0.064
ABCD	198.9°	142.2°	158.2°	138.5°	0.396	1.18	1.23	2.04	0.065

2.4 Reorientation of Linkages

In addition to reconfiguration through the kinematic path, structures can be *reoriented*, or rotated with respect to a global reference frame. For applications that require smooth motion in more than one orientation, such as robotics, it would be ideal to have one set of springs that ensure continuous equilibrium at all desired orientations. As the orientation of a system changes, the effect of gravity changes as well. Take for example a car door which opens effortlessly when the car is parked on flat ground, but swings closed when parked on a steep hill. To maintain functionality at multiple orientations, this change in gravity must be taken into account. We define an orientation angle ψ to describe the angle between a horizontal ground reference and the direction in which $\phi = 0°$ (Figure 2.3(A)). To change the orientation, the linkage is rotated about the support attached to the input link. In this chapter, we consider a range of orientations $\psi = 0°$ to $90°$.

Figure 2.3(B) shows the potential energy curves and contributions for the Watt's linkage at three orientations: $\psi = 0°$, $45°$, and $90°$. The potential energy due to gravity (gray plots) now changes with the orientation of the linkage as well as the configuration (i.e., $PE_G(\phi, \psi)$). For $\psi = 0°$ and $45°$, the system has a potential energy minimum at the end of the kinematic path; thus, the linkage collapses under gravity (Videos A.3 and A.5, Appendix A). For $\psi = 90°$, the linkage

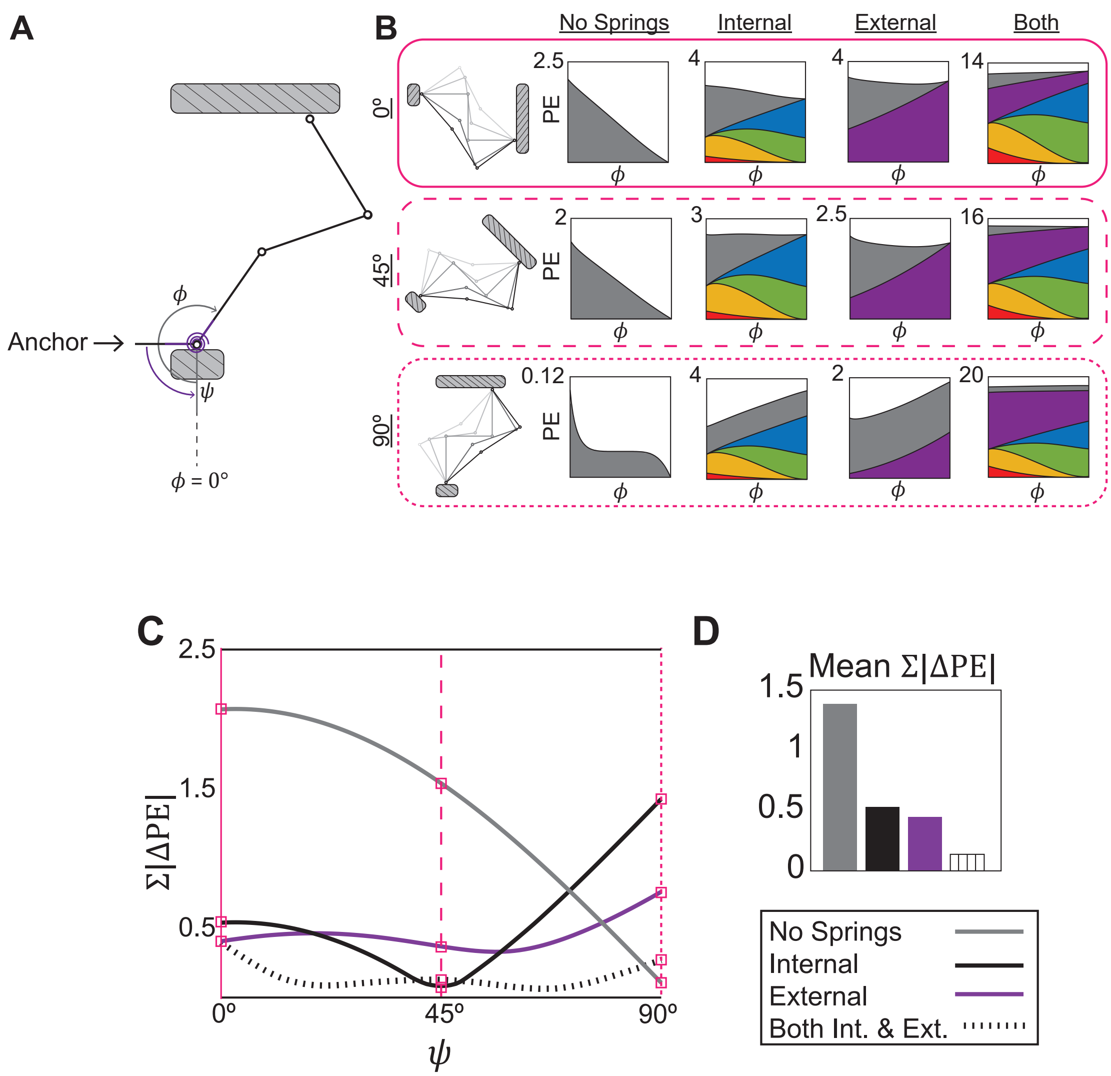

Figure 2.3: Reorientation of the Watt's linkage. (A) The orientation of the Watt's linkage is defined by the angle ψ. An external torsional spring is connected to the input link and to an external horizontal anchor. (B) Potential energy curves for three orientations of the Watt's linkage ($\psi = 0°$, $\psi = 45°$, $\psi = 90°$). The linkage is optimized for cases with four internal torsional and/or one external torsional spring. (C) The measure of the fluctuation in the potential energy curve over the kinematic path with respect to orientation ψ. (D) When considering more than one orientation, the mean($\Sigma|\Delta PE_T|$) is minimized. The case with both internal and external torsional springs results in the lowest mean($\Sigma|\Delta PE_T|$).

has a region of constant potential energy in the middle of the kinematic path. However, if the linkage is pushed outside of this range, it also collapses (Video A.6).

To evaluate the system performance over different orientations, we plot the value of $\Sigma|\Delta \mathrm{PE_T}|$ with respect to the orientation ψ (Figure 2.3(C)). Taking the mean of $\Sigma|\Delta \mathrm{PE_T}|$ over the range of ψ gives a measure of how close the structure is to continuous equilibrium at multiple orientations. As such, mean($\Sigma|\Delta \mathrm{PE_T}|$) = 0 indicates a structure with flat potential energy curves in *all* orientations. First, we use four internal torsional springs at locations A, B, C, and D to counteract gravity across multiple orientations. We define the optimization problem as:

$$\begin{aligned} \min \ & \left(\text{mean}\left(\sum \left|\Delta \mathrm{PE_T}(\phi,\psi)\right|\right)\right) \\ \text{s.t.} \ & k_j > 0 \\ & \alpha_j \in [\theta_{j\min}, \theta_{j\max}]. \end{aligned} \tag{2.5}$$

The design variables for the optimization problem are again the spring stiffnesses k_j and the rest angles α_j. The potential energy in the internal springs does not change with respect to ψ, so their energy contributions are always the same, regardless of the orientation of the linkage ('Internal' column in Figure 2.3(B)). As a result, $\Sigma|\Delta \mathrm{PE_T}|$ is reduced more for some orientations than for others. The internal springs minimize $\Sigma|\Delta \mathrm{PE_T}|$ most effectively for $\psi = 45°$, where the resulting $\mathrm{PE_T}$ curve is nearly flat (Figure 2.3(B-C)). For $\psi = 90°$, however, adding internal springs makes the potential energy curve less flat than it was initially ($\Sigma|\Delta \mathrm{PE_T}|$ is increased). Because the objective is to minimize the mean($\Sigma|\Delta \mathrm{PE_T}|$), the optimization does not necessarily lead to the smallest $\Sigma|\Delta \mathrm{PE_T}|$ for each individual orientation. However, across the range of orientations, adding internal springs reduces the mean($\Sigma|\Delta \mathrm{PE_T}|$) by 58%, from 1.382 N-m when no springs are used to 0.578 N-m with internal springs (Figure 2.3(D)).

Because the potential energy due to gravity is dependent on ψ, it would be beneficial to add a spring that also depends on ψ. Thus, we next add a single external torsional spring with one end attached to an external, horizontal anchor and one end attached to the input link of the Watt's linkage (Figure 2.3(A)). The potential energy of this external spring depends on both ϕ and ψ, because the rest angle α_E is defined with respect to the horizontal ground reference. The potential energy in the external spring is $\mathrm{PE_E} = \frac{1}{2}k_\mathrm{E}(\phi - \alpha^*)^2$, where $\alpha^* = \alpha_\mathrm{E} + \psi$ accounts for the orientation of the linkage. The total potential energy for a system with an external torsional spring under gravity is expressed as

$$\mathrm{PE_T}(\phi,\psi) = \sum_{i}^{n} \mathrm{PE}_{\mathrm{G}i}(\phi,\psi) + \mathrm{PE_E}(\phi,\psi), \tag{2.6}$$

and the optimization problem can be rewritten as

$$\begin{aligned} \min \ & \left(\text{mean}\left(\sum \left|\Delta \text{PE}_\text{T}(\phi,\psi)\right|\right)\right) \\ \text{s.t.} \ & k_\text{E} \ > \ 0 \\ & \alpha_\text{E} \ \epsilon \ [0, 2\pi], \end{aligned} \tag{2.7}$$

where the design variables are the stiffness of the spring k_E and the rest angle α_E. The stiffness is required to be > 0, and the range of α_E is limited to the range between 0 and 2π. The Watt's linkage optimized with one external torsional spring leads to a more effective minimization of the mean($\Sigma|\Delta \text{PE}_\text{T}|$) than the case with only internal torsional springs (Figure 2.3(B)). For $\psi = 90°$, $\Sigma|\Delta \text{PE}_\text{T}|$ is still higher than the case with no springs (Figure 2.3(C)), but not as high as the internal spring case. The case with only one external spring reduces the mean($\Sigma|\Delta \text{PE}_\text{T}|$) by 67.8% to 0.445 N-m (Figure 2.3(D)).

Finally, we consider adding both the four internal torsional springs and one external torsional spring. The total potential energy in the system for this case is expressed as

$$\text{PE}_\text{T}(\phi,\psi) = \sum_i^n \text{PE}_{\text{G}i}(\phi,\psi) + \sum_j^m \text{PE}_{\text{S}j}(\phi) + \text{PE}_\text{E}(\phi,\psi). \tag{2.8}$$

The design variables of the optimization problem are the stiffnesses and rest angles of all springs, internal and external, and the objective is again to minimize the mean($\Sigma|\Delta \text{PE}_\text{T}|$) over all desired orientations.

$$\begin{aligned} \min \ & \left(\text{mean}\left(\sum \left|\Delta \text{PE}_\text{T}(\phi,\psi)\right|\right)\right) \\ \text{s.t.} \ & k_j \ > \ 0 \\ & \alpha_j \ \epsilon \ [\theta_{j\text{min}}, \theta_{j\text{max}}] \\ & k_\text{E} \ > \ 0 \\ & \alpha_\text{E} \ \epsilon \ [0, 2\pi] \end{aligned} \tag{2.9}$$

Adding both internal and external torsional springs significantly improves upon the results from the other two cases. The potential energy curves are nearly flat for $\psi = 0°, 45°$, and $90°$ (Figure 2.3(B)), and the $\Sigma|\Delta \text{PE}_\text{T}|$ is decreased for nearly all orientations (Figure 2.3(C)). By adding both sets of torsional springs, we reduce mean($\Sigma|\Delta \text{PE}_\text{T}|$) to 0.137 N-m, a 90% reduction from the case with no springs (Figure 2.3(D)). The optimized spring properties for all cases are included in Table

Table 2.2: Spring properties and mean($\Sigma|\Delta\mathrm{PE_T}|$) values for the Watt's linkage, optimized for $\psi = 0°$ to $90°$ with four internal torsional springs, one external torsional spring, and both four internal and one external torsional spring. For the structure with no springs, the mean($\Sigma|\Delta\mathrm{PE_G}|$) = 1.382 N-m.

Springs		Rest Angle					Stiffness [N-m/rad]					
Int. Tors.	Ext. Tors.	α_A	α_B	α_C	α_D	α_E	k_A	k_B	k_C	k_D	k_E	Mean($\Sigma|\Delta\mathrm{PE_T}|$)
✓		202.3°	139.3°	155.3°	147.7°		3.01	3.69	3.49	2.61		0.578 N-m
	✓					22.1°					0.569	0.445 N-m
✓	✓	203.5°	143.9°	159.2°	137.3°	306.8°	4.64	5.66	5.50	6.68	1.10	0.137 N-m

Table 2.3: Spring properties and mean($\Sigma|\Delta\mathrm{PE_T}|$) values for the Watt's linkage, optimized for various ranges of ψ.

	Rest Angle					Stiffness [N-m/rad]					
Range	α_A	α_B	α_C	α_D	α_E	k_A	k_B	k_C	k_D	k_E	Mean($\Sigma|\Delta\mathrm{PE_T}|$)
0° to 90°	203.5°	143.9°	159.2°	137.3°	306.8°	4.64	5.66	5.50	6.68	1.10	0.137 N-m
0° to 60°	209.9°	144.0°	159.2°	137.3°	333.0°	4.12	5.16	5.02	6.48	0.77	0.0905 N-m
0° to 30°	214.3°	144.0°	159.3°	137.3°	355.4°	2.86	3.80	3.72	5.12	0.42	0.0602 N-m

2.2.

It is possible to reduce the mean($\Sigma|\Delta\mathrm{PE_T}|$) further by limiting the system to a smaller range of ψ; for instance, the mean($\Sigma|\Delta\mathrm{PE_T}|$) is 0.0602 N-m for a range of $\psi = 0°$ to $30°$. The optimized spring properties for several ranges of ψ are included in Table 2.3.

2.5 Effect of Spring Kinematic Relationships on System Performance

This section explores how system kinematics influence the performance of different spring types when optimizing for continuous equilibrium. We use the MATLAB function **fit** to determine the order of the spring kinematics when they are plotted against the kinematic angle ϕ. We use the coefficient of determination (R^2 value) to determine the polynomial that best fits the kinematic curve. The maximum possible R^2 value is 1.

The angle kinematics for the Watt's linkage are plotted in Figure 2.1(A). We define θ_A as equal to ϕ, so a linear fit provides an R^2 value of 1. The angles θ_B, θ_C, and θ_D reach R^2=1 with a fourth-order polynomial fit (Table 2.4). As we will see in this section, the lack of symmetry in the Watt's linkage leads to an effective minimization of $\Sigma|\Delta\mathrm{PE_T}|$.

Table 2.4: R^2 values for polynomial fits of Watt's Linkage angle kinematics.

Fit Type	θ_A	θ_B	θ_C	θ_D
Linear	1	0.8935	0.8738	0.9946
Quadratic		0.9989	0.9970	0.9990
Cubic		0.9998	0.9987	0.9993
Quartic		1	1	1

Table 2.5: R^2 values for polynomial fits of Scissor Mechanism angle kinematics.

Fit Type	θ_A	θ_B	θ_C	θ_D
Linear	1	1	1	1
Quadratic				
Cubic				
Quartic				

Scissor Mechanism

The Scissor Mechanism is another simple four-bar linkage that is often found in construction and engineering [25]. On the Scissor Mechanism, internal torsional springs can be placed in four locations, (A, B, C, and D in Figure 2.4(A)). When optimized, the PE_T curve is not as flat as the optimal result for the Watt's linkage, and quantitatively $\Sigma|\Delta\text{PE}_\text{T}|$ is only reduced by 88%, from 1.77 N-m to 0.214 N-m (Figure 2.4(B)). This smaller reduction is because the Scissor Mechanism is a symmetric linkage with all spring angles being linearly related: $\theta_A = \theta_B$, $\theta_C = \theta_D$, and $\theta_C = 180° - \theta_A$ (Figure 2.4(A), Table 2.5). Thus, the potential energy due to the internal springs consists of four quadratic (2nd-order) terms; in fact, using any combination of springs results in roughly the same overall performance (Figure 2.4(C) and Table 2.6).

Due to symmetry in the system kinematics, this is the best result that we can achieve with torsional springs. For further improvement to the continuous equilibrium performance, we can also add *extensional springs*. The potential energy of an *internal extensional spring* x is $\text{PE}_x = \frac{1}{2}k_x(L_x - L_{0x})^2$, where k is the spring stiffness (units: N/m), $L_x(\phi)$ is the length of the spring which depends on the kinematics of the structure, and L_0 is the rest length (units: m). On the Scissor Mechanism, there are two locations for internal extensional springs: one connecting adjacent nodes, and one spanning across the linkage (Springs 1 and 2, Figure 2.5(A)). The extensional springs have sinusoidal relationships with ϕ and are not symmetric with each other (Table 2.7). The length of extensional spring 1 is directly related to ϕ: $l_1 = L\sin\phi$, where L is the member length, so a one-term sinusoidal fit results in an R^2 value of 1. The length of extensional spring 2 requires a three-term sinusoidal fit for an R^2 value of 1. This variation in kinematic relationships allows the extensional springs to minimize $\Sigma|\Delta\text{PE}_\text{T}|$ to 0.004 N-m (a 99.8% reduction), a much

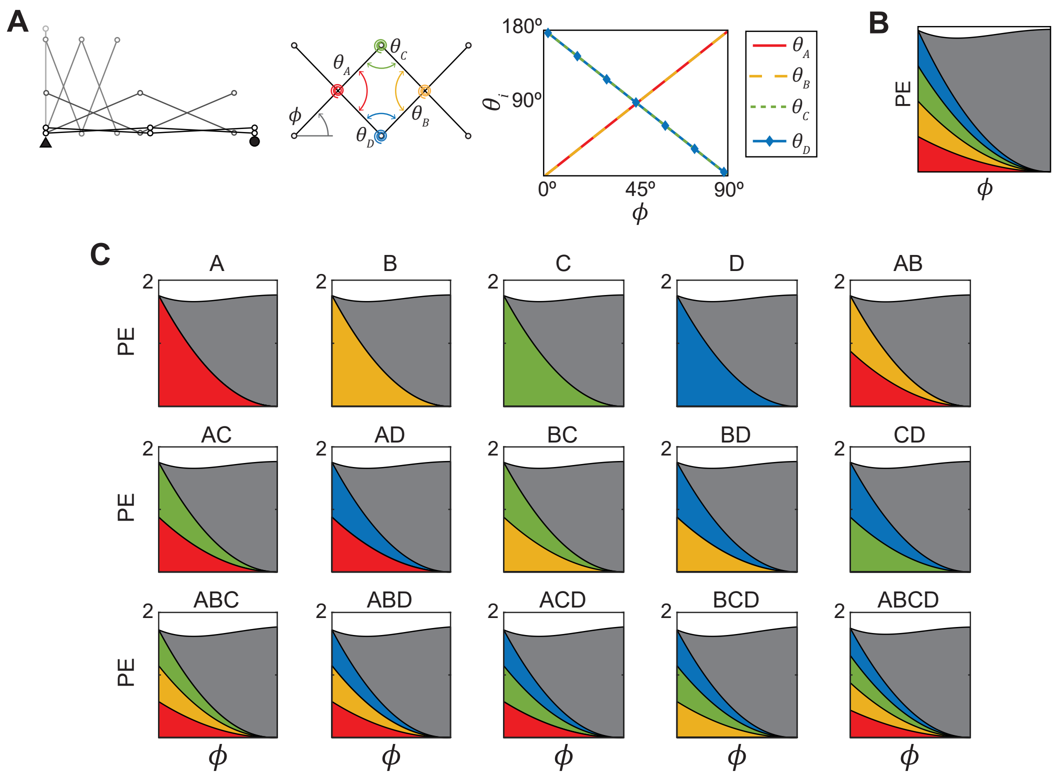

Figure 2.4: Designing the Scissor Mechanism to have continuous equilibrium. (A) The Scissor Mechanism has two sets of symmetric angles that are linearly related. (B) Adding four internal torsional springs at locations A, B, C, and D reduces the fluctuation in potential energy by 88%. (C) Potential energy breakdowns for all possible location combinations of internal torsional springs on the Scissor Mechanism, optimized for $\psi = 0°$. Due to symmetry in the system geometry, the total potential energy curve is nearly equivalent for all cases.

Table 2.6: Spring properties and $\Sigma|\Delta\mathrm{PE_T}|$ values for all possible location combinations of internal torsional springs on the Scissor Mechanism.

	Rest Angle				Stiffness [N-m/rad				
	α_A	α_B	α_C	α_D	k_A	k_B	k_C	k_D	$\Sigma\|\Delta\mathrm{PE_T}\|$ [N-m]
No Springs									1.77
A	179.5°				0.36				0.202
B		179.5°				0.36			0.202
C			0.49°				0.36		0.202
D				0.49°				0.36	0.202
AB	179.0°	179.0°			0.18	0.18			0.206
AC	179.0°		0.98°		0.18		0.18		0.206
AD	179.0°			0.98°	0.18			0.18	0.206
BC		179.0°	0.98°			0.18	0.18		0.206
BD		179.0°		0.98°		0.18		0.18	0.206
CD			0.98°	0.98°			0.18	0.18	0.206
ABC	173.2°	173.2°	6.76°		0.13	0.13	0.13		0.255
ABD	173.2°	173.2°		6.76°	0.13	0.13		0.13	0.255
ACD	173.2°		6.76°	6.76°	0.13		0.13	0.13	0.255
BCD		173.2°	6.76°	6.76°		0.13	0.13	0.13	0.255
ABCD	178.1°	178.1°	1.93°	1.93°	0.09	0.09	0.09	0.09	0.214

Table 2.7: R^2 values for sinusoidal fits of the Scissor Mechanism internal extensional spring lengths.

Fit Type	L_1	L_2
Sinusoidal (1-term)	1.0000	0.9886
Sinusoidal (2-term)		0.9992
Sinusoidal (3-term)		1.0000

more effective minimization than with torsional springs.

Another possibility is adding an *external extensional spring*, with one end attached to the Scissor Mechanism and the other end anchored to an external support (Spring 3, Figure 2.5(B)). In this case, the design parameters of the optimization problem are the (X,Y) coordinates of the external anchor point along with the stiffness and rest length of the spring. The potential energy of the external extensional spring is $\mathrm{PE}_X = \frac{1}{2}k_X(\sqrt{(u-X)^2+(v-Y)^2} - L_{0X})^2$, where k_X is the spring stiffness (units: N/m), L_{0X} is the rest length (units: m) and $(u(\phi), v(\phi))$ is the point where the spring is attached to the Scissor Mechanism. Adding only this external extensional spring reduces $\Sigma|\Delta\mathrm{PE_T}|$ from 1.77 N-m to 0.0065 N-m (a 99.6% reduction). Table 2.8 provides the design variable values for the optimized Scissor Mechanism with internal torsional springs, internal extensional springs, and an external extensional spring.

We also consider the reorientation of the Scissor Mechanism from $\psi = 0°$ to 90° (Figure 2.6).

Table 2.8: Spring properties and mean($\Sigma|\Delta\mathrm{PE_T}|$) values for the Scissor Mechanism, optimized for $\psi = 0°$.

Springs			Rest Angle				Stiffness [N-m/rad]				Rest Length [m]			Stiffness [N/m]			
Int. Tor.	Int. Extens.	Ext. Extens.	α_A	α_B	α_C	α_D	k_A	k_B	k_C	k_D	L_1	L_2	L_3	k_1	k_2	k_3	Mean($\Sigma\|\Delta\mathrm{PE_T}\|$)
✓			178.1°	178.1°	1.93°	1.93°	0.09	0.09	0.09	0.09							0.214 N-m
	✓										0.503	0.024		11.66	4.125		0.004 N-m
		✓											1.26			10.6	0.0065 N-m

Table 2.9: Spring properties and mean($\Sigma|\Delta\mathrm{PE_T}|$) values for the Scissor Mechanism, optimized for $\psi = 0°$ to $90°$.

Springs				Rest Angle					Stiffness [N-m/rad]					Rest Length [m]			Stiffness [N/m]			
Int. Tor.	Ext. Tor.	Int. Extens.	Ext. Extens.	α_A	α_B	α_C	α_D	α_E	k_A	k_B	k_C	k_D	k_E	L_1	L_2	L_3	k_1	k_2	k_3	Mean($\Sigma\|\Delta\mathrm{PE_T}\|$)
✓				54.0°	54.0°	126.0°	126.0°		0.157	0.157	0.157	0.157								1.41 N-m
	✓							71.3°								2.28				0.287 N-m
✓	✓			89.7°	89.7°	90.3°	90.3°	71.3°	0	0	0	0	2.28							0.287 N-m
		✓												1.12	0.647		2.96	31.5		1.5378 N-m
			✓													1.46			15.5	0.794 N-m
✓		✓		45.3°	45.3°	134.7°	134.7°		0.133	0.133	0.133	0.133		0.125	0.326		11.5	3.88		1.41 N-m
	✓		✓					67.1°					2.21			0.754			2.76	0.232 N-m
✓	✓	✓	✓	82.7°	82.7°	97.3°	97.3°	31.9°	0	0	0	0	0.0063	0	3.44	0	26.7	0.0031	8.92	0.0013 N-m

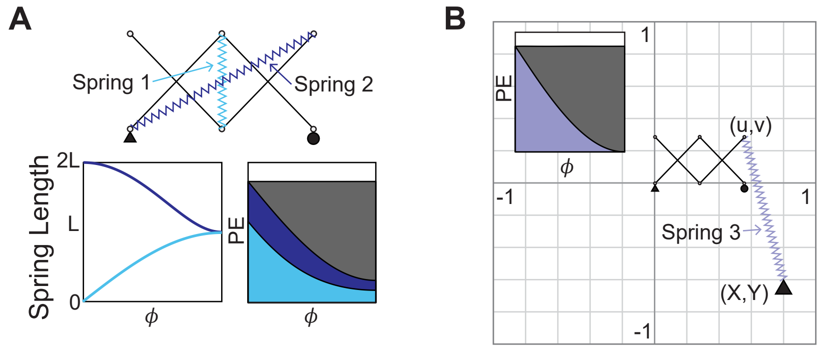

Figure 2.5: Scissor Mechanism with extensional springs. (A) Adding two internal extensional springs or (B) one external extensional spring to the Scissor Mechanism results in total potential energy curves that are flatter than the case with four internal torsional springs.

Similar to the Watt's linkage, adding an external torsional spring and attaching it to a horizontal ground reference is more effective than internal torsional springs at providing continuous equilibrium at different orientations because its potential energy is dependent on both configuration ϕ and orientation ψ (Figure 2.6(A)). The same is true when considering extensional springs, where a single external extensional spring provides a substantial advantage for obtaining continuous equilibrium in all orientations (Figure 2.6(B-D)). Using all potential spring types in the optimization framework allows for near perfect continuous equilibrium performance in all orientations of the Scissor Mechanism (note the logarithmic scale in Figure 2.6(C)). In reality, the case with only the external torsional spring and external extensional spring may suffice, as this combination provides a 89% reduction in the mean($\Sigma|\Delta \mathrm{PE_T}|$). Table 2.9 provides the design variable values for the optimized Scissor Mechanism from $\psi = 0°$ to $90°$ with internal torsional springs, external torsional springs, internal extensional springs, and an external extensional spring.

Double Rocker Linkage

A contrasting example is a non-symmetric Double Rocker linkage, a four-bar linkage with unequal bar lengths. The Double Rocker linkage has four angles with kinematic paths that are not symmetric nor linearly related (Figure 2.7(A)). The angle θ_A is linearly related to ϕ: $\theta_A = \pi - \phi$, so the R^2 value for the linear fit is equal to 1. The angles θ_B and θ_C have third-order (cubic) fits with respect to ϕ, and θ_D has a fourth-order (quartic) fit (Table 2.10).

This variety of higher order terms in $\mathrm{PE_T}$ gives the system more freedom to offset the effect of gravity and leads to a more effective minimization of $\Sigma|\Delta \mathrm{PE_T}|$. Adding four internal torsional springs to the Double Rocker linkage reduces the $\Sigma|\Delta \mathrm{PE_T}|$ by over 99%, from 0.372 N-m to 0.003 N-m (Figure 2.7(B)). Because there is no symmetry, adding more internal torsional springs

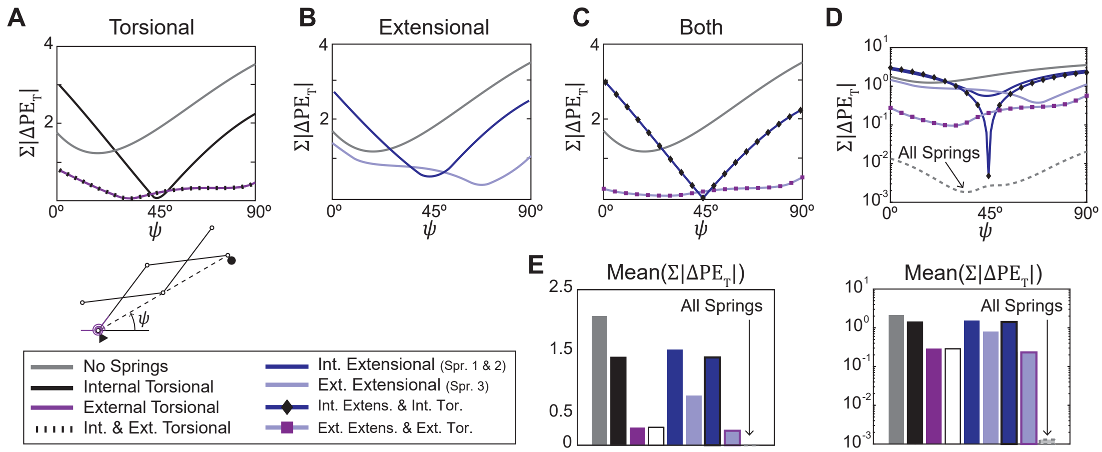

Figure 2.6: Reorientation of the Scissor Mechanism. (A) The external torsional spring is better at minimizing the mean($\Sigma|\Delta PE_T|$) than internal torsional springs; when both are added, the internal springs do not have an effect. (B) An external extensional spring is more effective at minimizing mean($\Sigma|\Delta PE_T|$) than internal extensional springs. (C) When torsional and extensional springs are both used, the case with an external extensional spring and an external torsional spring is the best combination. (D) When all springs are added, $\Sigma|\Delta PE_T|$ is significantly reduced for all orientations (note the log scale). (E) Bar plots of the mean($\Sigma|\Delta PE_T|$) for all cases.

Table 2.10: R^2 values for polynomial fits of Double Rocker angle kinematics.

Fit Type	θ_A	θ_B	θ_C	θ_D
Linear	1	0.9965	0.9916	0.9792
Quadratic		0.9965	0.9949	0.9992
Cubic		0.9995	0.9987	0.9993
Quartic		1.0000	1.0000	1.0000

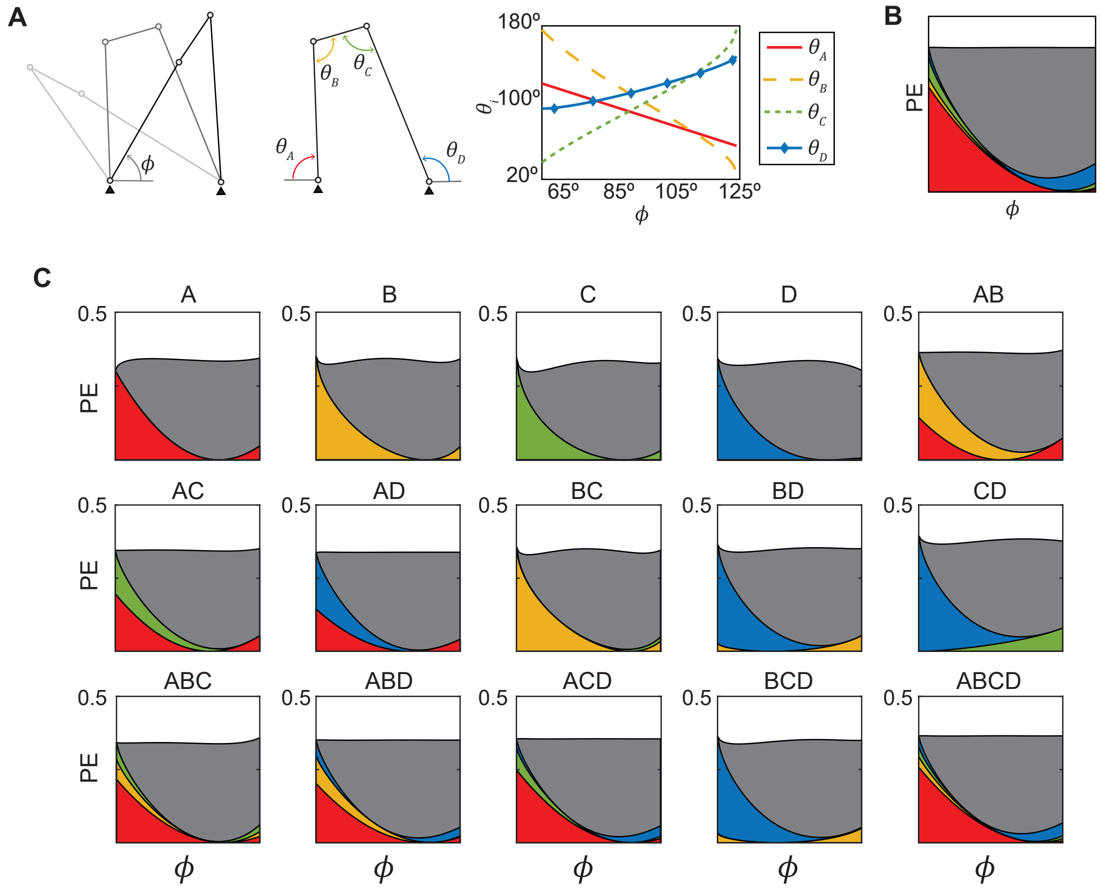

Figure 2.7: Designing the Double Rocker linkage to have continuous equilibrium. (A) The Double Rocker linkage is a four-bar linkage with three links of unequal lengths. Four locations for internal torsional springs are defined with angles θ_A, θ_B, θ_C, and θ_D. There is no symmetry in the spring angle kinematics. (B) Adding four internal torsional springs reduces the $\Sigma|\Delta \mathrm{PE_T}|$ by over 99%. (C) Potential energy breakdowns for all possible location combinations of four internal torsional springs on the Double Rocker linkage.

generally improves the result, but some combinations are better than others. Table 2.11 contains the optimized rest angles α_j, stiffnesses k_j, and $\Sigma|\Delta \mathrm{PE_T}|$ values for all location combinations for internal torsional springs added to the Double Rocker linkage. Figure 2.7(C) illustrates the potential energy contributions for each location combination.

Similarly to the Scissor Mechanism, we can add internal extensional springs to the Double Rocker linkage (Springs 1 and 2, Figure 2.8(A)). The internal extensional springs have sinusoidal relationships with respect to ϕ (Table 2.12), and they minimize $\Sigma|\Delta \mathrm{PE_T}|$ to 0.0018 N-m (a 99.5% reduction).

We can also an external extensional spring in a similar manner as the Scissor Mechanism (Spring 3, Figure 2.8(B)). Adding only this external extensional spring reduces $\Sigma|\Delta \mathrm{PE_T}|$ from

Table 2.11: Spring properties and $\Sigma|\Delta PE_T|$ values for all possible location combinations of internal torsional springs on the Double Rocker linkage.

	Stiffness [N-m/rad]				Rest Angle				
	α_A	α_B	α_C	α_D	k_A [N-m/rad]	k_B [N-m/rad]	k_C [N-m/rad]	k_D [N-m/rad]	$\Sigma|\Delta PE_T|$ [N-m]
No Springs									0.372
A	101.6°				0.91				0.0598
B		136.8°				0.19			0.073
C			69.6°				0.20		0.0998
D				100.1°				0.98	0.073
AB	92.9°	172.3°			0.66	0.069			0.018
AC	97.8°		45.9°		0.702		0.058		0.014
AD	97.4°			95.8°	0.53			0.46	0.004
BC		140.6°	124.7°			0.18	0.012		0.073
BD		91.2°		94.2°		0.049		0.75	0.045
CD			162.6°	94.0°			0.033	0.88	0.054
ABC	98.1°	107.9°	45.8°		0.70	0.0033	0.056		0.015
ABD	108.7°	132.3°		116.5°	0.50	0.042		0.41	0.003
ACD	109.4°		83.9°	120.2°	0.57		0.048	0.31	0.002
BCD		95.6°	118.0°	94.2°		0.048	0.0039	0.74	0.046
ABCD	111.4°	129.8°	86.9°	122.4°	0.53	0.023	0.028	0.35	0.003

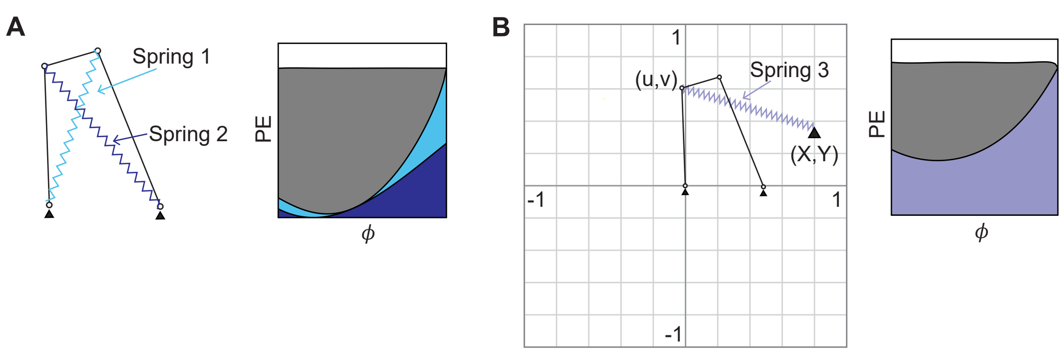

Figure 2.8: Adding extensional springs to the Double Rocker linkage. (A) Adding internal extensional springs reduces the $\Sigma|\Delta PE_T|$ by 99.5%. (B) Using an external extensional spring reduces the $\Sigma|\Delta PE_T|$ by 92%.

Table 2.12: R^2 values for sinusoidal fits of Double Rocker internal extensional spring lengths.

Fit Type	L_1	L_2
Sinusoidal (1-term)	0.9992	1.0000
Sinusoidal (2-term)	0.9998	
Sinusoidal (3-term)	1.0000	

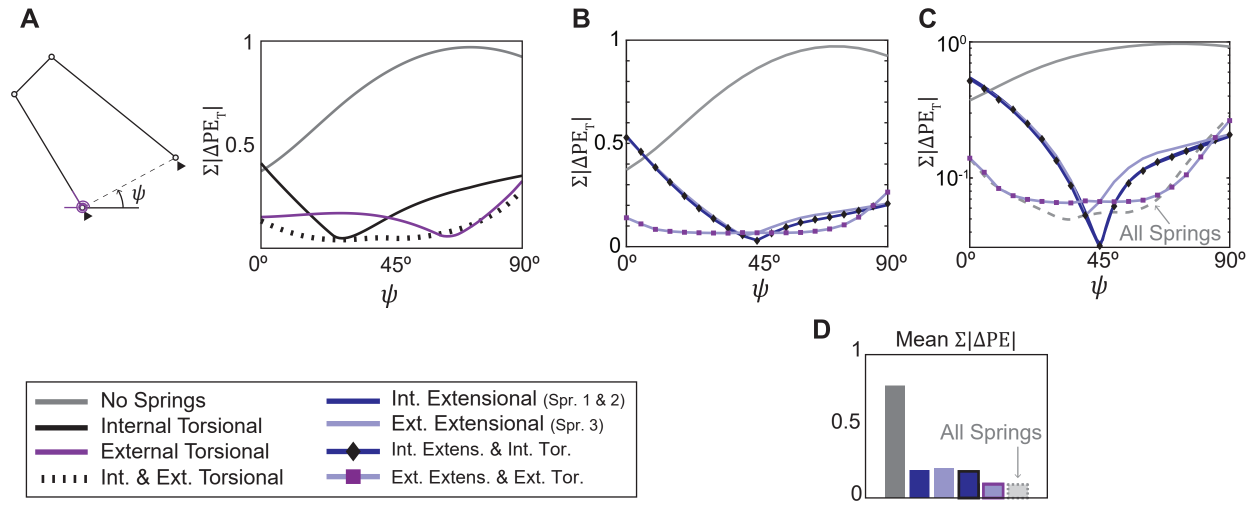

Figure 2.9: The Double Rocker linkage at orientations $\psi = 0°$ to $90°$. (A) When considering torsional springs, the case with both internal and external torsional springs minimizes mean($\Sigma|\Delta \mathrm{PE_T}|$) most effectively. (B) Adding an external torsional spring and an external extensional spring improves the minimization. (C) Using every type of spring marginally reduces the mean($\Sigma|\Delta \mathrm{PE_T}|$) from the case with external torsional and extensional springs. (D) Bar plot showing the mean($\Sigma|\Delta \mathrm{PE_T}|$) for each case.

0.372 N-m to 0.03 N-m (a 92% reduction). Table 2.13 provides the design variable values for the optimized Double Rocker linkage with internal torsional springs, internal extensional springs, and an external extensional spring.

We can also explore which type of springs are most effective when the Double Rocker linkage is reoriented between $\psi = 0°$ to $90°$. For the system with only torsional springs, the combination of internal and external torsional springs reduces the fluctuation in potential energy the most (Figure 2.9(A)). Due to the lack of symmetry in the kinematics, the internal torsional springs have an effect, unlike the Scissor Mechanism (Figure 2.6(A)). The case with external torsional and external extensional springs reduces the mean($\Sigma|\Delta \mathrm{PE_T}|$) nearly as much as the case with all springs (Figure 2.9(C-D)). Table 2.14 contains the spring parameters for all spring cases of the Double Rocker linkage for orientations $\psi = 0°$ to $90°$.

Table 2.13: Spring properties and mean($\Sigma|\Delta \text{PE}_\text{T}|$) values for the Double Rocker linkage, optimized for $\psi = 0°$.

Springs			Rest Angle				Stiffness [N-m/rad]				Rest Length [m]			Stiffness [N/m]			
Int. Tor.	Int. Extens.	Ext. Extens.	α_A	α_B	α_C	α_D	k_A	k_B	k_C	k_D	L_1	L_2	L_3	k_1	k_2	k_3	Mean($\Sigma|\Delta \text{PE}_\text{T}|$)
✓			111.4°	129.8°	86.9°	122.4°	0.53	0.02	0.03	0.35							0.003 N-m
	✓										0.30	0.27		19.8	21.1		0.0018 N-m
		✓											1.20			38.6	0.030 N-m

Table 2.14: Spring properties and mean($\Sigma|\Delta \text{PE}_\text{T}|$) for the Double Rocker linkage, optimized for $\psi = 0°$ to $90°$.

Springs				Rest Angle					Stiffness [N-m/rad]					Rest Length [m]			Stiffness [N/m]			
Int. Tor.	Ext. Tor.	Int. Extens.	Ext. Extens.	α_A	α_B	α_C	α_D	α_E	k_A	k_B	k_C	k_D	k_E	L_1	L_2	L_3	k_1	k_2	k_3	Mean($\Sigma|\Delta \text{PE}_\text{T}|$)
✓				199.9°	175.4°	76.5°	161.0°		0.90	0.04	0.001	0.003								0.219 N-m
	✓							67.9°					0.55							0.150 N-m
✓	✓			90.1°	93.2°	81.5°	152.2°	46.5°	0.012	0.043	0.044	0.014	0.434							0.088 N-m
		✓												1.86	0.20		1.66	18.3		0.185 N-m
			✓													1.24			10.1	0.199 N-m
✓		✓		84.1	93.4	105.0	145.5		0.047	0.024	0.077	0.075		0.19	0.13		2.54	28.1		0.185 N-m
	✓		✓					40.6					0.44			1.01			91.3	0.0941 N-m
✓	✓	✓	✓	90.5	53.3	135.8	136.9	125.1	6.91	0.27	0.18	1.11	0.43	0.06	0.35	0.27	48.3	33.0	45.6	0.089 N-m

2.6 Extension to Various Design Cases

The optimization method can be expanded from simple four bar linkages to more complex structures. We use the framework to design a scissor lift, a model of a knee, and an origami arch. These examples add complexity by including an external mass carried along a linear path, radial path, and expanding the principles to a three-dimensional origami structure, respectively.

2.6.1 Scissor Lift

The scissor lift is a larger version of the Scissor Mechanism at $\psi = 90°$ with equivalent kinematics and the addition of an external mass. We model the linkage with all member lengths of 1 m, uniform mass distribution equal to 10 kg/m, and an external mass that is carried along a linear path (to represent the weight of the basket and occupants) of M = 200 kg, with its center located at the midpoint of the last scissor unit (Figure 2.10(A)). Based on the results in Figure 2.6, we chose to use an external torsional spring and two internal extensional springs to obtain continuous equilibrium. This combination of springs reduces the mean($\Sigma|\Delta \mathrm{PE_T}|$) for orientations between $45°$ and $90°$ by 96.5% (Figure 2.10(B)). The mean($\Sigma|\Delta \mathrm{PE_T}|$) for the case with no springs is 9640 N-m, and the mean($\Sigma|\Delta \mathrm{PE_T}|$) with springs is 336.2 N-m. The spring properties are as follows: $k_1 = 5043.5$ N/m, $L_1 = 0.235$ m, $k_2 = 639.8$ N/m, $L_2 = 0.284$ m, $k_E = 3665.0$ N-m/rad, $\alpha_E = 0°$. The same set of springs reduces the fluctuation in potential energy at each orientation (Figure 2.10(C)).

2.6.2 Knee Exoskeleton

Next, we model a knee exoskeleton as a planar linkage with two members of equal length (45 cm) resembling the human leg connected to a "foot" which is anchored to the ground. We add four shorter bars of equal length (15 cm) positioned at the knee joint (Figure 2.11(A)). The lower "calf" member defines the orientation ψ of the system, while the upper "thigh" member reconfigures with kinematics defined by the angle ϕ with respect to the calf member. The self-weight of the members (2.5 kg each) is applied at their centroids and an external mass $M = 30$ kg is applied at the top of the thigh member and is carried along a radial path. After exploring different combinations, we chose to use four internal torsional springs and one internal extensional spring to obtain continuous equilibrium. The internal extensional spring is connected to location B on the linkage and to the heel joint of the structure. The internal torsional springs have kinematics that are symmetric and linearly related while the internal extensional spring has a sinusoidal relationship with ϕ (Figure 2.11(B)). The magnitude of the potential energy due to gravity of the system changes with the orientation ψ, but the *shape* of the $\mathrm{PE_G}$ curve does not, so internal springs are sufficient to minimize

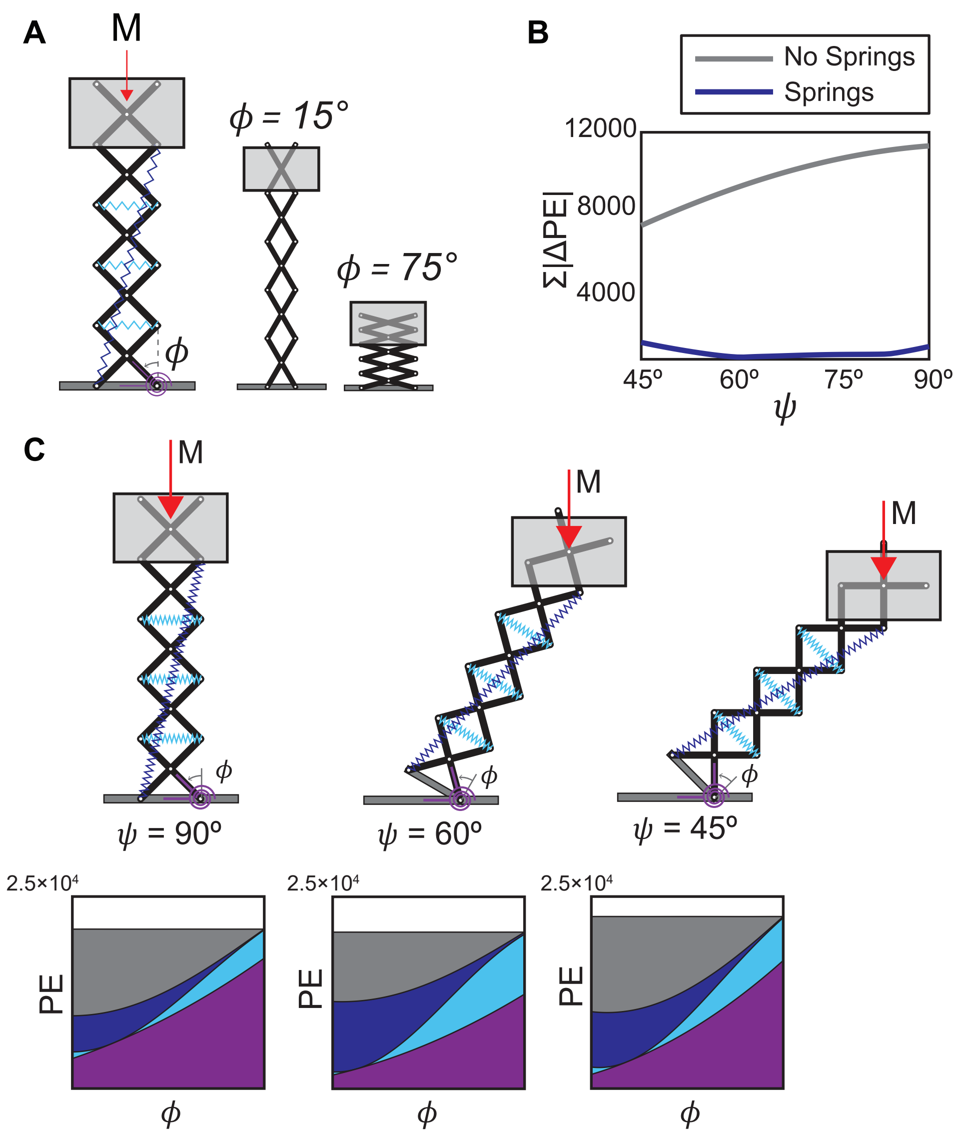

Figure 2.10: A scissor lift designed to have continuous equilibrium in any orientation between $\psi = 45°$ and $90°$. (A) The scissor lift carries an external mass along a linear path. (B) Adding internal extensional springs and an external torsional spring significantly reduces the mean($\Sigma|\Delta PE_T|$) over the range of orientations. (C) The $\Sigma|\Delta PE_T|$ curve is flattened at each orientation.

the mean($\Sigma|\Delta \mathrm{PE_T}|$). Adding springs reduces the mean($\Sigma|\Delta \mathrm{PE_T}|$) by 98% for orientations $70° < \psi < 105°$, from 128.7 N-m to 2.65 N-m. Figure 2.11(C) shows the plot of the potential energy contributions at several orientations. The optimized spring parameters for the knee model at $\psi =$ 70° to 105° are $\alpha_A = 88.3°$, $\alpha_B = 90.9°$, $\alpha_C = 86.1°$, $\alpha_D = 90.9°$, $k_A = 16.8$ N-m/rad, $k_B = 33.8$ N-m/rad, $k_C = 7.11$ N-m/rad, $k_D = 33.7$ N-m/rad, $L_1 = 0.354$ m, $k_1 = 3856.2$ N/m. With the structure optimized for continuous equilibrium, the external mass is now counterbalanced both during reconfiguration of the knee joint and as the structure reorients about the ankle joint.

2.6.3 Origami Arch

The three-dimensional origami arch is made from a variation of the Miura-ori unit cell, which is the base for many origami structures [87]. The arch is a single DOF mechanism consisting of sixty-four origami panels that fold from a flat state, with kinematics defined by the fold angle ϕ [88]. We consider a range of $100° < \phi < 175°$ (Figure 2.12(A)). The potential energy for a three-dimensional system with n panels is $\mathrm{PE_G} = \sum_i^n m_i * A_i * g * h_i$, where m_i is the mass distribution (units: N/m^2), A_i is the area, $g = 9.81$ m/s^2, and h_i is the height of the center of mass of panel i. We model the structure with a uniform mass distribution of 1 kg/m^2 and panel areas of approximately 0.1 m^2. To keep the design simple, we limit possible spring connection points to locations within each cell made up of four panels, and we choose to use three internal torsional springs at the fold lines of the pattern (θ_A, θ_B, and θ_C) and two internal extensional springs on each cell. The kinematics of the fold angles are not symmetric or linearly related to each other, and the length of the extensional spring has a quadratic relationship with ϕ (Figure 2.12(B)). These factors result in the internal springs effectively minimizing the $\Sigma|\Delta \mathrm{PE_T}|$ by 96.1%, from 43.0 N-m to 1.69 N-m as it deploys from $\phi = 175°$ to 100° (Figure 2.12(C)) The optimized spring parameters are $\alpha_A = 140.1°$, $k_A = 0.3572$ N-m/rad, $\alpha_B = 123.9°$, $k_B = 0.6526$ N-m/rad, $\alpha_C = 81.0°$, $k_C = 1.443$ N-m/rad, $L_1 = 0.136$ m, $k_1 = 12.4$ N/m. This example demonstrates that the principles from our work can be readily extended to an arbitrary three-dimensional system. While we limit the design to springs internal to each unit cell, the arch structure could be optimized using springs that interconnect any of the sixty-four panels. All of the possible spring connection points could be explored using a method similar to the ground structure approach used in topology optimization [89]. While we have not optimized this system for reorientation, the origami arch could also be rotated about a given axis and optimized for a range of orientations. When considering a range of orientations, we expect that external springs would be needed.

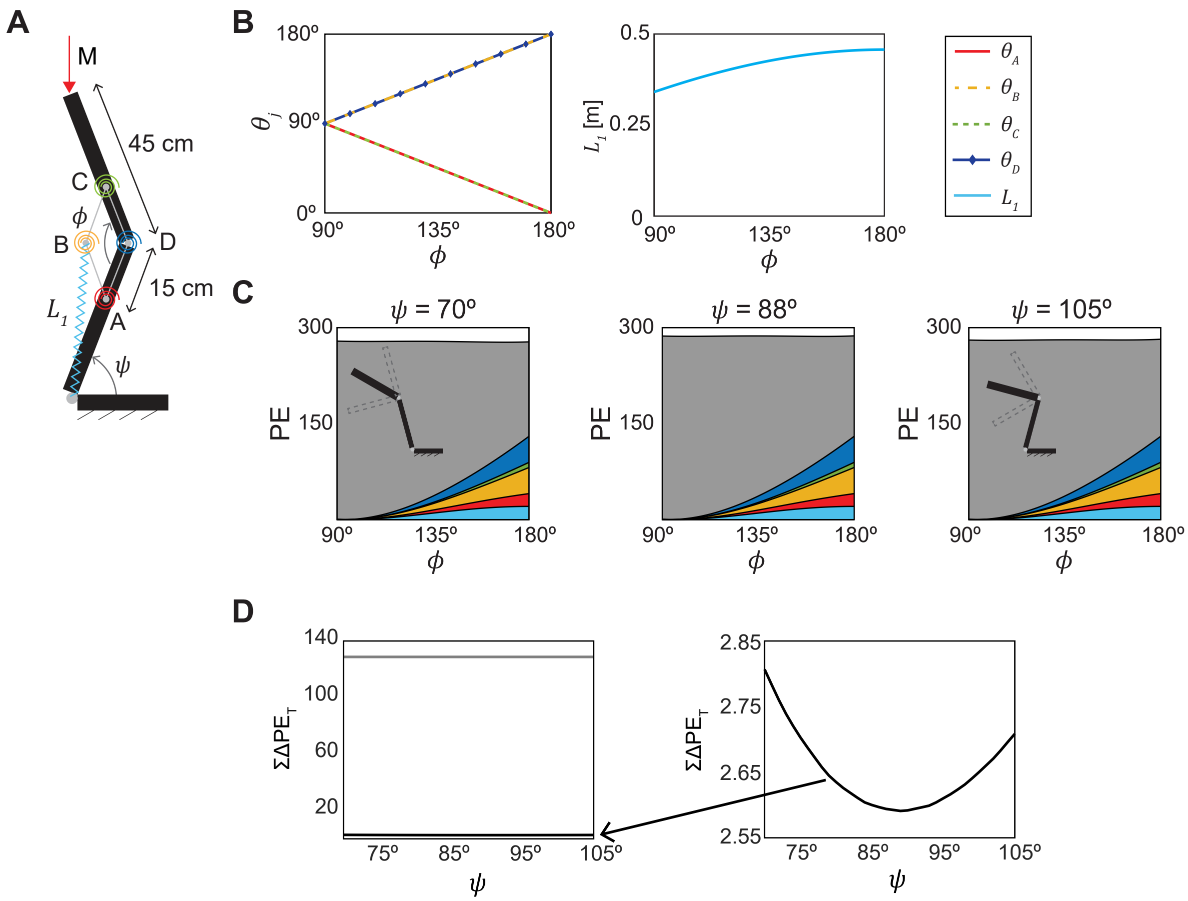

Figure 2.11: A model of a knee exoskeleton designed to have continuous equilibrium. (A) The exoskeleton supports a vertical load for different radial paths that change with orientation. The knee is modeled as two members connected to a "foot" which is anchored to the ground. A symmetric four-bar linkage is placed at the knee. (B) The internal torsional springs are linearly related to ϕ, while the internal extensional spring has a sinusoidal relationship with ϕ. (C) The magnitude of the potential energy due to gravity changes slightly for different orientations, but the overall shape of the curve remains constant. (D) The mean($\Sigma|\Delta \mathrm{PE_T}|$) is reduced by 98% for orientations between $70° < \psi < 105°$.

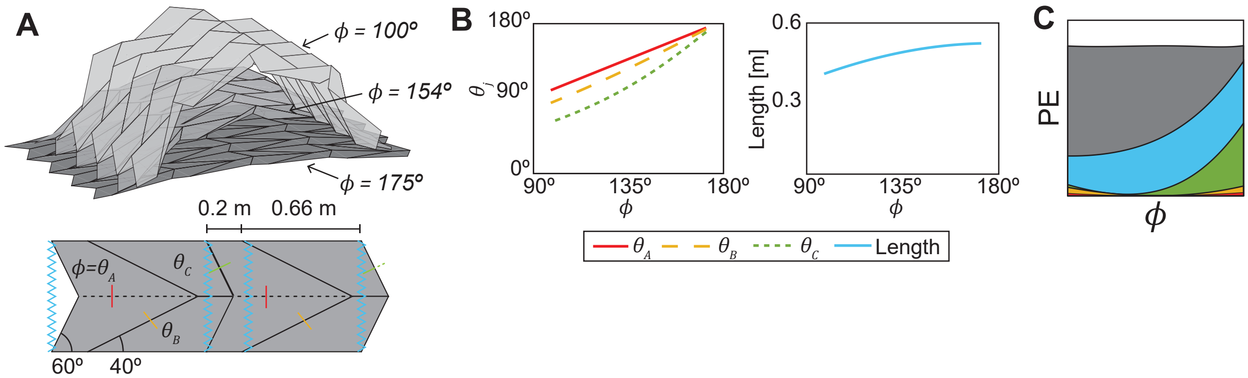

Figure 2.12: Designing a three-dimensional origami arch to have continuous equilibrium. (A) The arch structure deploys from a flat state. Three internal torsional springs are added to the system at θ_A, θ_B, and θ_C, and two extensional springs are included in each cell. (B) The angles of the origami arch are not symmetric or linearly related. The length of the extensional spring is also not linearly related to the angles with respect to the kinematics defined by ϕ. (C) The fluctuation in potential energy is reduced by 96%.

2.7 Concluding Remarks

In this chapter, we introduced a comprehensive method for designing reconfigurable structures that maintain continuous equilibrium under gravity. Our method involves optimizing the properties of internal, external, torsional, and extensional springs that counteract gravity to minimize the fluctuation of the potential energy curve throughout the kinematic path. The optimization framework can be used to design structures for a range of orientations, leading to one design that has continuous equilibrium properties even as the orientation of the structure changes. Combinations of springs with asymmetric kinematics tend to result in better performance, and external springs are the most effective when considering a structure at multiple orientations. We demonstrated how our design framework can be applied to real-world systems including a linkage with an external mass carried along a linear path, a linkage with a mass carried along a radial path, and a three-dimensional deployable origami arch. Using optimization to design for continuous equilibrium results in reconfigurable structures that are more stable, efficient, and versatile for any application scenario. The framework presented in this work will expand the ability of designers and engineers to create versatile, multi-functional systems to be used in many engineering fields.

CHAPTER 3

Programming Stable Motions in Multi-DOF Systems

Many reconfigurable structures, such as retractable roofs, robotic exoskeletons, and deployable bridges, have more than one degree of freedom (DOF) which allows for enhanced, sequential, and varied motions. However, designing such systems at a civil engineering scale is difficult because the effect of gravity is significant. Multi-DOF systems require complex controls to achieve desired motion paths and ensure stability, and their actuation requires large energy inputs to counteract gravity, often resulting in over-engineered designs. This chapter presents a method for transforming multi-DOF reconfigurable structures into systems with continuous equilibrium, allowing them to be unconditionally stable and reconfigured with a negligible input of energy. The continuous equilibrium systems are achieved through the addition of springs with properties that are optimized to directly counteract gravity as the structure moves with respect to the different DOFs. The method can design a multi-DOF system to have continuous equilibrium throughout its entire kinematic space, or alternatively, to program specific continuous equilibrium paths so that the structure can move in a desired way while maintaining stability. Planar linkages and three-dimensional origami structures are used to demonstrate the method and show that the principles are applicable to structures with any number of DOFs. This chapter furthers the ability of structural designers to create reconfigurable structures that are efficient to actuate, achieve desired motions, and remain stable under gravity.

The work presented in this chapter has been submitted for publication and is under review [90].

3.1 Introduction

In this chapter, we use springs with optimized properties to program stable configurations, stable paths, and sequential stable paths into multi-DOF structures by using the principle of *continuous equilibrium*. An n-DOF structure in continuous equilibrium has a potential energy space with dimension n that is nearly constant. This property results in a system that is perpetually stable and requires negligible energy to move from one configuration to another. Examples in the literature

[74, 75, 43, 76, 77, 91] are limited to single-DOF systems, and most do not consider the effect of gravity. In this chapter, we extend our previous work on one-DOF systems [86] to multi-DOF reconfigurable structures and demonstrate how desired paths can be programmed as continuous equilibrium motions.

This chapter is organized as follows: Section 3.2 describes the design method for creating multi-DOF structures with continuous equilibrium. Section 3.3 focuses on designing structures with programmed continuous equilibrium states, such as stable configurations and paths. Section 3.4 gives examples of how the design method can be expanded to practical and more complex structures. The computer codes used to generate the results presented in this chapter are provided on GitHub.

3.2 Designing a Multi-DOF Planar Linkage for Continuous Equilibrium

In this section, we discuss how springs can be designed and added to a multi-DOF linkage to convert it into a system that counteracts gravity. We design variations of the Watt's linkage such that they will have continuous equilibrium by adding torsional springs that counteract the effect of gravity. We assume the structure is a planar linkage made of rigid bars and rotational joints. For an $n-$DOF system, the kinematics are defined by independent parameters $\phi_1, ..., \phi_n$. The potential energy due to gravity for a planar system with B bars is

$$\mathrm{PE_G}(\phi_1, ..., \phi_n) = \sum_b^B m_b * L_b * g * h_b(\phi_1, ..., \phi_n), \tag{3.1}$$

where m_b is the uniform mass distribution (units: N/m), L_b is the bar length, $g = 9.81$ m/s^2, and h_b is the height of the center of mass of bar b. For the Watt's linkage examples, we assume that all bars have a length of 1 m and a uniform mass distribution of 1 kg/m.

We use optimization to compute the torsional spring properties (rest angle and stiffness) that counteract gravity most effectively. The potential energy in a torsional spring depends on one or more of the degrees of freedom ($\phi_1, ..., \phi_n$ for an n-DOF system); as the configuration of the structure changes, each spring will move towards or away from its rest position and will release or store energy. In a system with S torsional springs, the potential energy stored in the springs is

$$\mathrm{PE_S}(\phi_1, ..., \phi_n) = \sum_s^S \frac{1}{2} k_s(\theta_s(\phi_1, ..., \phi_n) - \alpha_s)^2, \tag{3.2}$$

where k_s is the linear stiffness (units: N-m/rad), θ_s is the kinematic angle of the spring (which can be a function of one or more of the DOFs, depending on the system kinematics), and α_s is the rest angle of the spring, where the stored potential energy is zero. The total potential energy of the system of bars and springs is

$$\mathrm{PE_T}(\phi_1, ..., \phi_n) = \mathrm{PE_S}(\phi_1, ..., \phi_n) + \mathrm{PE_G}(\phi_1, ..., \phi_n). \tag{3.3}$$

3.2.1 Optimization Setup

A system in continuous equilibrium has constant potential energy. To formulate an objective function for our design problem, we elect to minimize the fluctuation in total potential energy ($\mathrm{PE_T}$) of the system across the entire kinematic space.

In Chapter 2, we used the quantity $\Sigma|\Delta\mathrm{PE_T}|$ to measure the fluctuation in potential energy along the kinematic path of a one-DOF structure. In this chapter, we use a root-mean-square deviation (RMSD) to quantify the fluctuation in potential energy. The formula for RMSD is:

$$RMSD = \sqrt{\frac{\sum(\mathrm{PE_T} - \mathrm{mean}(\mathrm{PE_T}))^2}{N}}, \tag{3.4}$$

where N is the number of points used to sample $\mathrm{PE_T}$. With adequate discretization in sampling, the normalized sum in Equation 3.4 is equivalent to the integral over the entire $\mathrm{PE_T}$ space, regardless of the dimension. Thus, this formulation is applicable to any n-DOF system. The two measures of fluctuation are both valid objective functions, but we found that using the RMSD led to more consistent convergence for multi-DOF systems. For example, using the $\Sigma|\Delta\mathrm{PE_T}|$ to design the three-DOF Watt's linkage (discussed in detail in section 3.2.4) requires four rounds of optimization to converge (Figure 3.1(A)), and using RMSD requires only one (Figure 3.1(B)). After one round of optimization, the fluctuation in potential energy is significantly more reduced when using RMSD (Figure 3.1(C-D), note that the contour lines are equivalently spaced at 2 N-m in both (C) and (D)). Therefore, all examples in this chapter use RMSD as the objective function.

The bounds placed on the design variables ensure that the stiffness of each spring is positive ($k_s \geq 0$) and restricts the rest angle of a torsional spring to the interval $[0,\ 2\pi]$. There are no additional constraints placed on the optimization problem, which is defined as:

$$\min\left(\sqrt{\frac{\sum(\mathrm{PE_T} - \mathrm{mean}(\mathrm{PE_T}))^2}{N}}\right) \tag{3.5}$$

$$\text{s.t. } k_s \geq 0 \tag{3.6}$$

$$\alpha_s \in [0,\ 2\pi]. \tag{3.7}$$

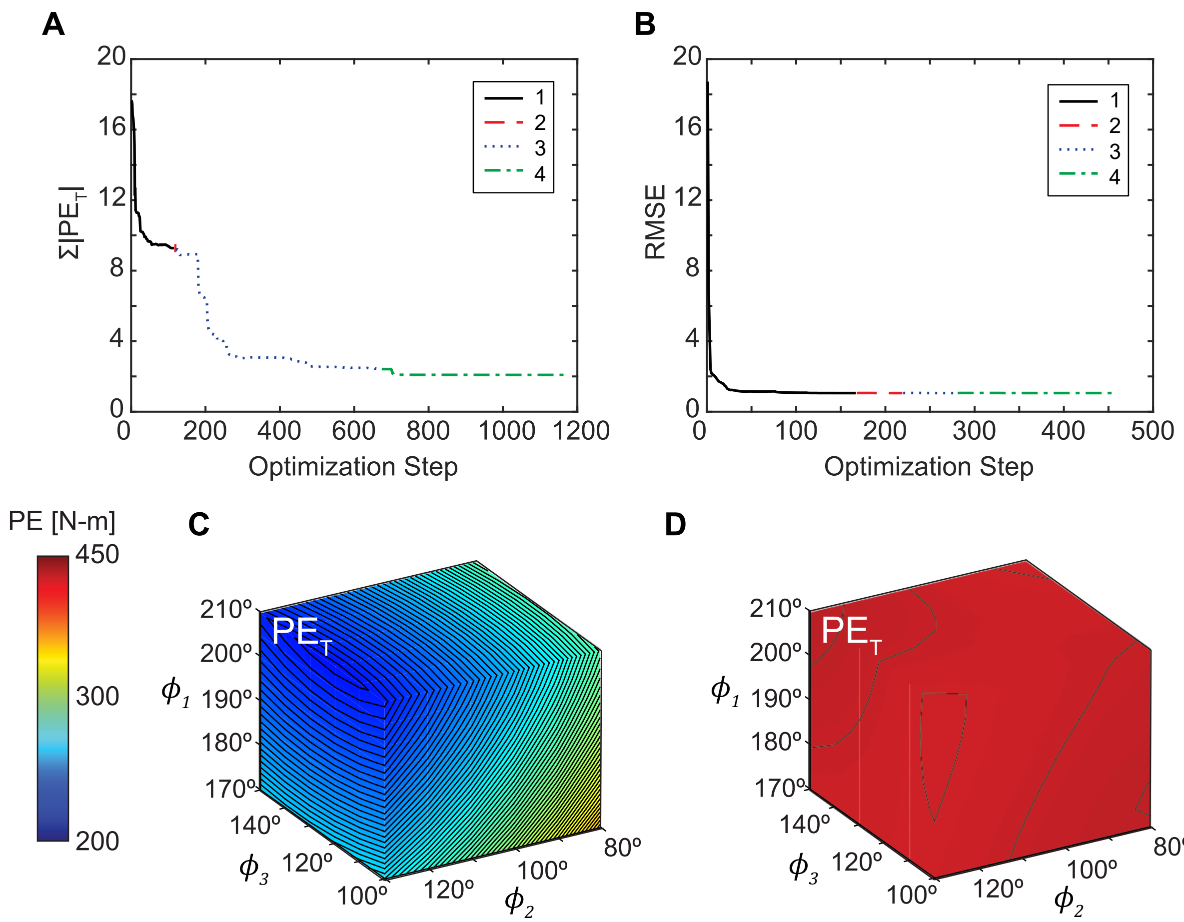

Figure 3.1: Comparing two objective functions used to minimize the fluctuation in total potential energy in a three-DOF system. (A) Using the objective function $\Sigma|\Delta PE_T|$ requires four rounds of optimization to converge. At the end of each round, the design variable output is used as the input for the next round. (B) Using the RMSD as the objective function converges after one round of optimization. (C) The total potential energy for a three-DOF system after one round of optimization using the $\Sigma|\Delta PE_T|$ objective function (contour line interval = 2 N-m). (D) The total potential energy for a three-DOF system after one round of optimization using the RMSD objective function (contour line interval = 2 N-m).

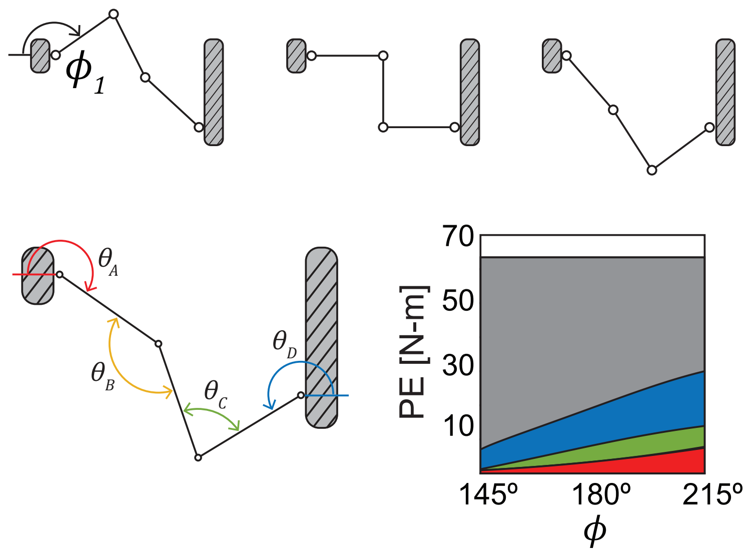

Figure 3.2: Optimizing the one-DOF Watt's linkage for continuous equilibrium. The one-DOF Watt's linkage has kinematics defined by ϕ_1. Adding internal torsional springs at locations A, B, C, and D reduces the fluctuation in PE_T by 99.97%.

3.2.2 One-DOF Watt's linkage

The system kinematics of the one-DOF Watt's linkage are defined by the angle ϕ_1 (Figure 3.2. The fluctuation in potential energy due to gravity is equal to 6.8 N-m. To achieve continuous equilibrium, we add four internal torsional springs at locations A, B, C, and D. The optimization problem given in Equation 3.5 is used to compute the spring properties ($k_s,\ \alpha_s$) that minimize the fluctuation in PE_T. Adding the four springs results in a fluctuation of 0.0021 N-m, a 99.97% reduction from the fluctuation without springs. The resulting PE_T curve is nearly flat, indicating that the system is in continuous equilibrium. The spring properties for the one-DOF Watt's linkage are given in Table 3.1.

3.2.3 Two-DOF Watt's linkage

The two-DOF Watt's linkage has kinematics defined by the independent angles ϕ_1 and ϕ_2. The potential energy due to gravity varies with both DOFs and can be visualized as a two-dimensional surface (Figure 3.3). To achieve continuous equilibrium, we add five internal torsional springs at locations A, B, C, D, and E. The total potential energy of the system is written as

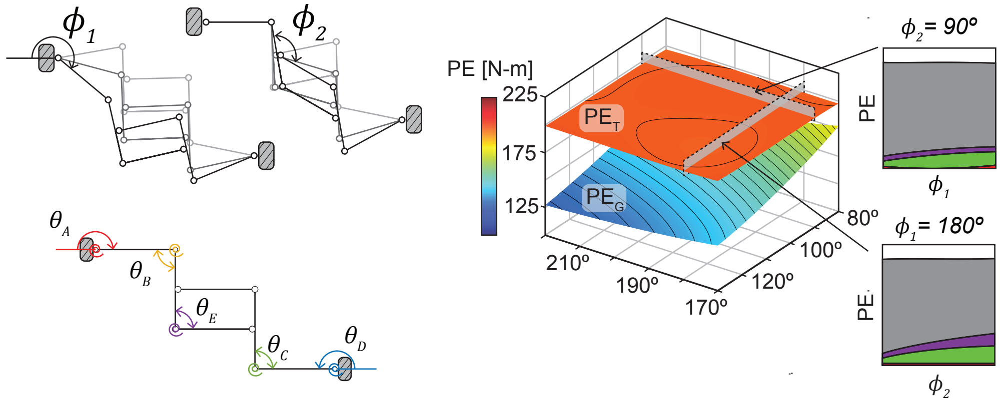

Figure 3.3: Optimizing the two-DOF Watt's linkage for continuous equilibrium. The two-DOF Watt's linkage has kinematics defined by ϕ_1 and ϕ_2. Adding five internal torsional springs minimizes the fluctuation in the PE_T surface by 97.3% (contour line interval = 2 N-m). Cross-sections of the PE_T surface show nearly flat potential energy curves.

$$\mathrm{PE_T}(\phi_1,\phi_2) = \frac{1}{2}k_A(\theta_A(\phi_1,\cancel{\phi_2}) - \alpha_A)^2 + \frac{1}{2}k_B(\theta_B(\phi_1,\phi_2) - \alpha_B)^2 + \frac{1}{2}k_C(\theta_C(\phi_1,\phi_2) - \alpha_C)^2 + \tag{3.8}$$
$$\frac{1}{2}k_D(\theta_D(\phi_1,\phi_2) - \alpha_D)^2 + \frac{1}{2}k_E(\theta_E(\cancel{\phi_1},\phi_2) - \alpha_E)^2 + \mathrm{PE_G}(\phi_1,\phi_2).$$

Springs B, C, and D have kinematics that depend on both DOFs, while spring A depends only on ϕ_1 and spring E depends only on ϕ_2. Using Equation 3.5, we compute the spring properties that will counteract gravity and result in continuous equilibrium throughout the entire two-dimensional potential energy space. With the springs, the fluctuation in PE_T is reduced by 97.3% from 10.8 N-m to 0.29 N-m, resulting in a nearly flat surface. Two cross-sections of the PE_T surface are shown in Figure 3.3 for $\phi_1 = 180°$ and $\phi_2 = 90°$. Along the cross-section where $\phi_1 = 180°$, the fluctuation in PE_T is reduced by 97.9% from 2.62 N-m to 0.05 N-m. For $\phi_2 = 90°$, the fluctuation is reduced by 99.8% from 1.36 N-m to 0.003 N-m. The optimized spring stiffnesses and rest angles for the two-DOF Watt's linkage are given in Table 3.1.

3.2.4 Three-DOF Watt's linkage

The three-DOF Watt's linkage has kinematics defined by three independent angles, ϕ_1, ϕ_2, and ϕ_3 (Figure 3.4. The potential energy due to gravity PE_G depends on all three DOFs and is visualized as a volume. To achieve continuous equilibrium, we add internal torsional springs at locations A,

Table 3.1: Optimized spring properties for the one-, two-, and three-DOF Watt's linkage.

	Rest Angle						Stiffness [N-m/rad]					
	α_A	α_B	α_C	α_D	α_E	α_F	k_A	k_B	k_C	k_D	k_E	k_F
One-DOF	108°	81°	184°	26°			4.29	0.51	3.55	3.08		
Two-DOF	157°	197°	166°	196°	116°		35.3	0	26.5	0	23.6	
Three-DOF	0°	142°	360°	197°	0°	159°	12.0	0	8.21	0	7.64	12.8

B, C, D, E, and F and optimize their properties. Springs B, C, and D depend on all three DOFs, while spring A depends only on ϕ_1, spring E depends only on ϕ_2, and spring F depends only on ϕ_3. The fluctuation in PE_T throughout the entire volume is reduced by 94.2%, from 18.1 N-m to 1.06 N-m with the addition of optimized springs. Three cross-sections of the potential energy volume are shown in Figure 3.4, showing that the potential energy surfaces corresponding to $\phi_1 = 180°$, $\phi_2 = 90°$, and $\phi_3 = 120°$ are nearly flat; the fluctuation in PE_T is reduced across the surfaces by 91.9%, 95.4%, and 96.5%, respectively. Extracting further, cross-sections of the surfaces illustrate that the PE_T curves are nearly flat for several combinations of ϕ_1, ϕ_2, and ϕ_3. For the cross-section where $\phi_1 = 180°$ and $\phi_3 = 110°$ (where ϕ_2 varies), the fluctuation in PE_T is reduced from 11.4 N-m to 1.3 N-m; for $\phi_3 = 120°$ and $\phi_2 = 100°$, it is reduced from 26 N-m to 0.33 N-m. However, for the case where $\phi_2 = 90°$ and $\phi_1 = 200°$, the fluctuation increases from 1.04 N-m to 1.44 N-m. Along this path, the potential energy due to gravity is nearly constant, meaning that the linkage is already counterbalanced simply based on the bar masses and the geometry of the structure. The optimized spring properties for the three-DOF Watt's linkage are given in Table 3.1.

3.3 Programming Continuous Equilibrium Motions

Programming specific motions into a reconfigurable structure allows certain paths to be favored and prohibits motion in unwanted directions. Programming a continuous equilibrium motion would allow a highly flexible system with many DOFs to navigate effortlessly along a desired path without requiring external forces to keep it on the path. We use a similar approach as described in Section 3.2 to design systems that, with the addition of springs with optimized properties, follow a programmed continuous equilibrium motion under gravity.

In this section, we begin by demonstrating how adding springs with optimized properties to the two-DOF Watt's linkage can be used to program a stable, continuous equilibrium path. Next, we show how additional springs can be used to program a stable configuration along a path. Finally, we explore how sequential continuous equilibrium paths can be programmed. The optimized spring properties for all examples in this section are provided in Table 3.2.

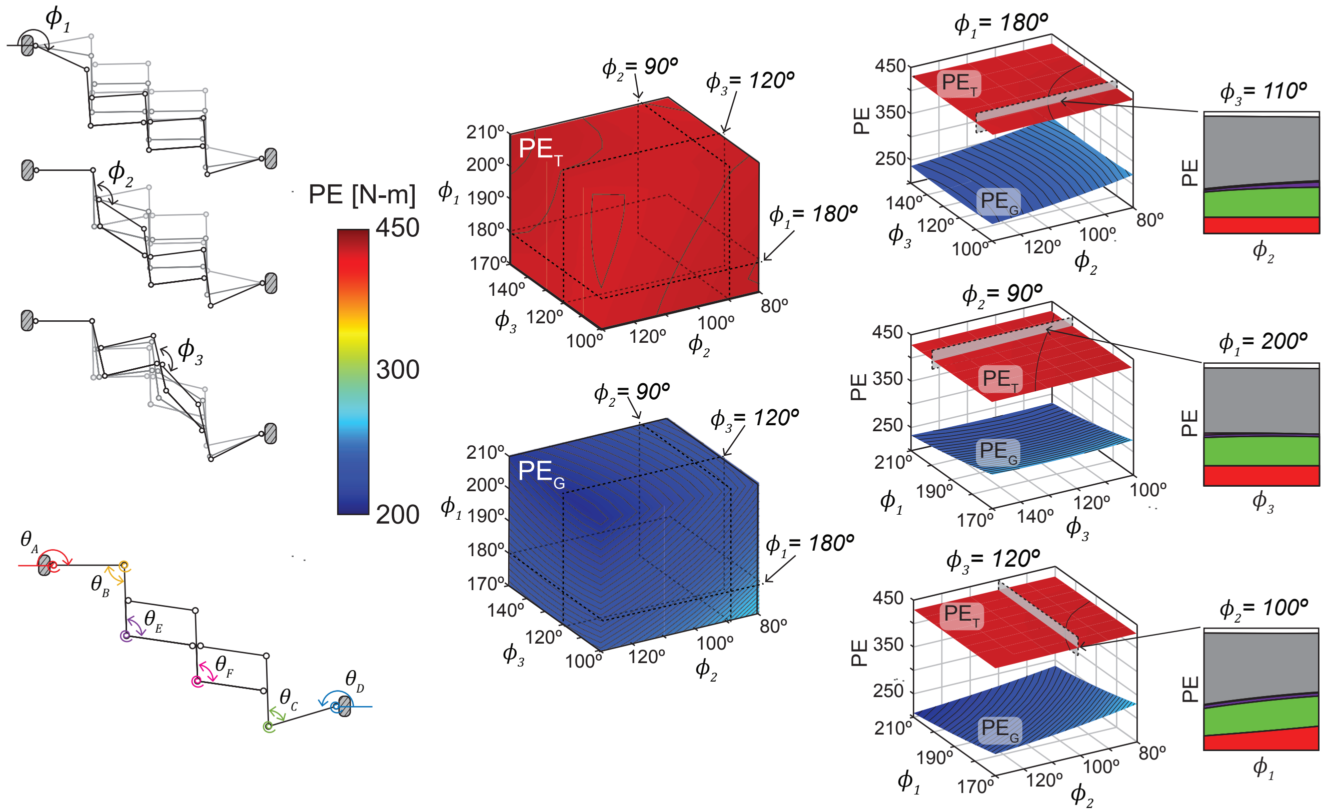

Figure 3.4: Optimizing the two-DOF Watt's linkage for continuous equilibrium. The three-DOF Watt's linkage is defined by angles ϕ_1, ϕ_2, and ϕ_3. The potential energy is visualized as a volume (contour line interval = 2 N-m). Taking cross sections of the volume shows that the $\mathrm{PE_T}$ surfaces at the cross-sections are nearly flat (contour line interval 2 = N-m). Cross-sections of the $\mathrm{PE_T}$ surfaces show nearly flat potential energy curves.

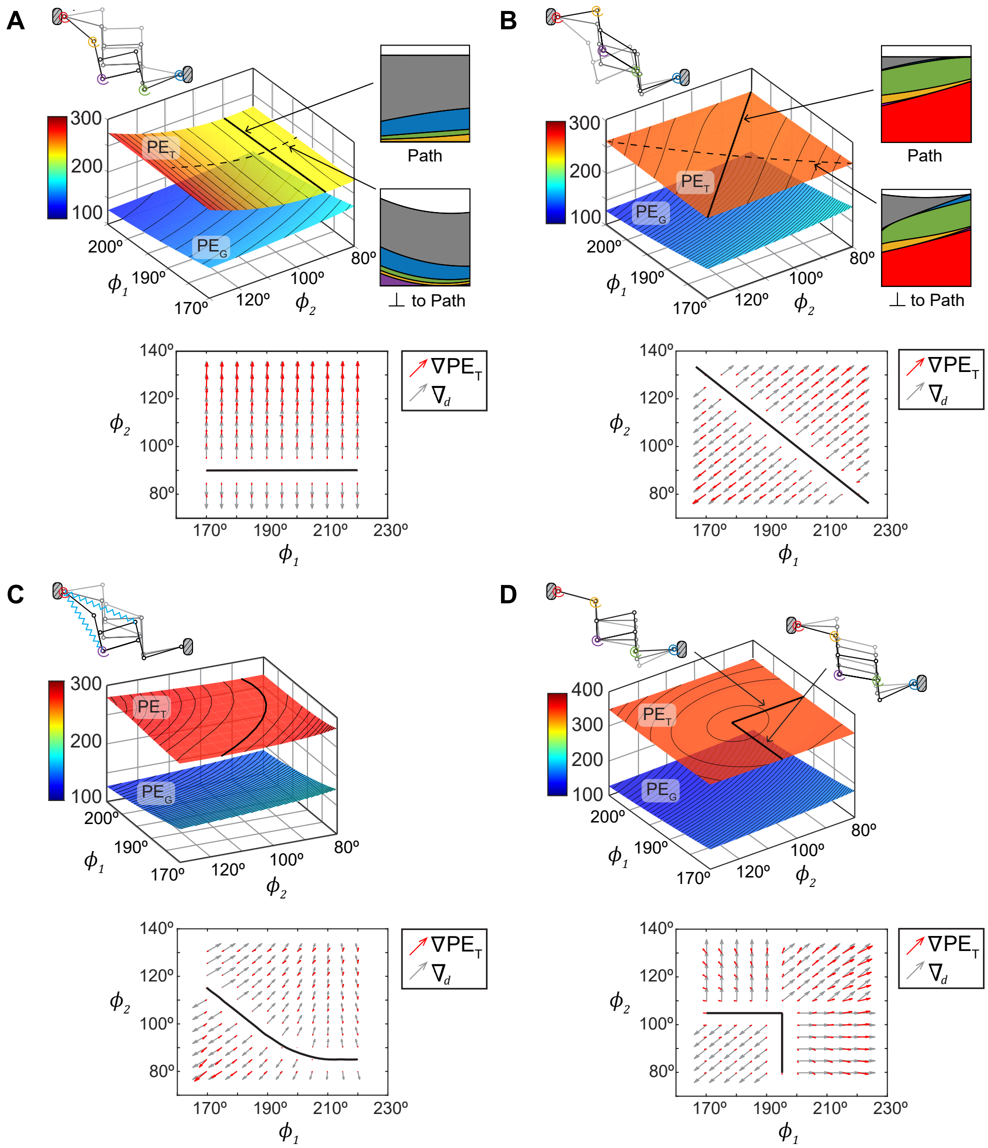

Figure 3.5: Designing the two-DOF Watt's linkage to have different stable paths. (A) To program a stable path along $\phi_2 = 90°$, we add five internal torsional springs. Along the path, the fluctuation in potential energy has been reduced by 99.7% (contour line interval = 5 N-m). Perpendicular to the path, the potential energy has a valley centered on $\phi_2 = 90°$. The gradient of the potential energy is aligned with the desired gradient field ∇_d. (B) Stable path along the line $\phi_2 = 300° - \phi_1$ (contour line interval = 1 N-m). The fluctuation in potential energy is reduced by 98.9% along the path. The potential energy valley is shallow, but the gradient of the potential energy is aligned with ∇_d. (C) For a curved path, we add two identical extensional springs to the linkage, and the fluctuation in potential energy along the path is reduced by 99.5% (contour line interval = 1 N-m). (D) Designing the two-DOF Watt's linkage to have two sequential stable paths, one along $\phi_1 = 180°$ and one along $\phi_2 = 90°$. The paths are placed into potential energy valleys by splitting ∇_d into four regions. Along the paths, the fluctuation is reduced by 93% (contour line interval = 1 N-m).

3.3.1 Programming a Stable Path

The objective for designing the two-DOF Watt's linkage with a stable path is to minimize the fluctuation of the $\mathrm{PE_T}$ *along the path*. We again use the RMSD as the objective function, formulated as:

$$\begin{aligned} &\min\left(\sqrt{\frac{\sum\left(\mathrm{PE}_{\mathrm{T}_{\mathrm{path}}}-\mathrm{mean}(\mathrm{PE}_{\mathrm{T}_{\mathrm{path}}})\right)^2}{N_{\mathrm{path}}}}\right) \\ &\text{s.t. } k_s \geq 0 \\ &\quad \alpha_s \in [0,\ 2\pi] \end{aligned} \tag{3.9}$$

where N_{path} is the number of sampling points along the path. Using this objective function, the path is designed to have continuous equilibrium, but the stability of the path is not enforced. For example, a system could be designed to have a perfectly flat path, but a small perturbation moving the system off of the path would lead to collapse. In order to ensure that the programmed continuous equilibrium path is stable, we implement additional constraints to the optimization problem.

To be stable, the desired path must be a global potential energy minimum (valley in two-dimensional space); the gradient of the potential energy ($\nabla\mathrm{PE_T}$) must be orthogonal to the path [78]. To ensure a stable path, we use constraints to align $\nabla\mathrm{PE_T}$ with a desired gradient field, denoted as ∇_d. For a two-DOF system with a given path defined as $\phi_2 = f(\phi_1)$, where $[u, v]$ is the tangent vector to the path, ∇_d is formulated as

$$\nabla_d = \begin{cases} [v, -u] & \phi_2 < f(\phi_1) \\ [-v, u] & \phi_2 > f(\phi_1), \end{cases} \tag{3.10}$$

describing the gradient field pointing orthogonal to the path. Once we have established ∇_d, we can compute the angle between it and $\nabla\mathrm{PE_T}$ at points across the entire $\mathrm{PE_T}$ space. The constraint requires the angle to be smaller than some positive value δ. The constraint is formulated as

$$\cos^{-1}(\nabla\mathrm{PE_T} \cdot \nabla_d) - \delta \leq 0, \tag{3.11}$$

and is applied to all sampled points in the kinematic design space. If $\nabla\mathrm{PE_T}$ is perfectly aligned with ∇_d, then the angle between them is zero, the constraint is satisfied, and the path is stable. The results presented in Figure 3.5 use a tolerance of $\delta = \pi/2$, meaning that the $\mathrm{PE_T}$ vector will point anywhere from orthogonal to the path (the ideal case) to parallel to the path. Further improvements to the optimization method could likely allow for smaller values of δ to be used in the constraint and thus provide a stricter assurance of path stability. Nevertheless, the results illustrate good

Table 3.2: Optimized spring properties for the two-DOF Watt's linkage, for various stable paths.

	Rest Position							Stiffness						
	Angle					Rest [m]		[N-m/rad]					[N/m]	
Path	α_A	α_B	α_C	α_D	α_E	L_{01}	L_{02}	k_A	k_B	k_C	k_D	k_E	k_1	k_2
$\phi_2 = 90°$	0°	0°	199°	0°	94°			0	6.3	5.9	8.7	200		
$\phi_2 = 300° - \phi_1$	0°	201°	266°	180°	93°			11.1	5.9	6.2	20.9	13.8		
$\phi_2 = (212° - \phi_1)^2 + 86°$	21.2°	77.5°				0.84	1.4	26.7	209				34.3	49.9
$\phi_2 = 105°;\ \phi_1 = 195°$	0°	360°	136°	235°	65°			20.8	6.5	14.6	0	24.5		

agreement between $\nabla \mathrm{PE_T}$ and ∇_d despite the large δ used. Equations 3.10 and 3.11 are presented here for a two-DOF system and could be extended for higher-DOF systems in the future.

Using the objective function given in Equation 3.9 and the constraint in Equation 3.11, we designed the two-DOF Watt's linkage to have a stable path at $\phi_2 = 90°$ (Figure 3.5(A)). The desired gradient field ∇_d is written as

$$\nabla_d = \begin{cases} [0, -1], & \phi_2 < 90° \\ [0, 1], & \phi_2 > 90°, \end{cases} \tag{3.12}$$

to enforce the stability of the path. We add five internal torsional springs, and the fluctuation in potential energy along the path is reduced by 99.7% compared to the system without springs. Comparing the plots of $\nabla \mathrm{PE_T}$ and ∇_d shows that these vectors are aligned, and there is a global potential energy valley along the path where $\phi_2 = 90°$. If the system experiences a small perturbation, it will naturally return to the path along $\phi_2 = 90°$.

For a path where $\phi_2 = 300° - \phi_1$ (Figure 3.5(B)), ∇_d is defined as:

$$\nabla_d = \begin{cases} [-1, -1], & \phi_2 < 300° - \phi_1 \\ [1, 1], & \phi_2 > 300° - \phi_1 \end{cases} \tag{3.13}$$

With five internal torsional springs, the potential energy is reduced by 98.9% along the path and there is a $\mathrm{PE_T}$ valley centered on the path. For this path, the valley is less pronounced than the previous example, but the stability of the path is still ensured due to the alignment of $\nabla \mathrm{PE_T}$ and ∇_d.

In addition to linear paths, we can design a curved path to have continuous equilibrium (Figure 3.5(C)). The equation of the path is $\phi_2 = (212° - \phi_1)^2 + 86°$. The tangent vector $[u, v]$ is thus equal to $[1, 2u - 424°]$ and ∇_d is defined as

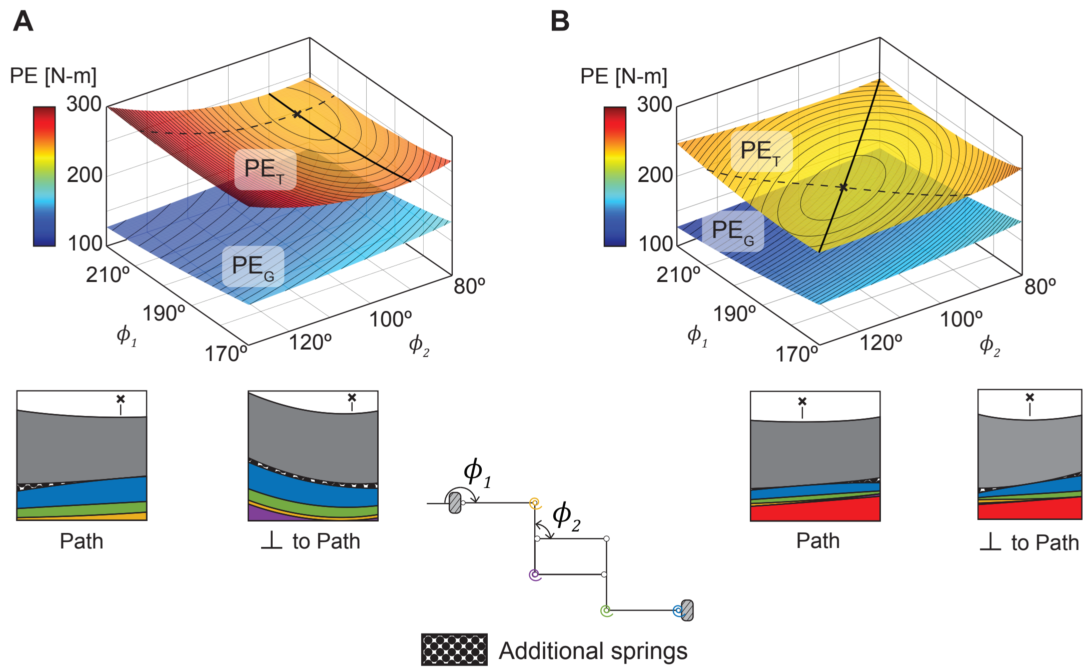

Figure 3.6: Adding stable configurations to stable paths using superposition. (A) Stable configuration at $\phi_1 = 210°$ and $\phi_2 = 90°$, along the path $\phi_2 = 90°$ (contour line interval = 2 N-m). (B) Stable configuration at $\phi_1 = 190°$ and $\phi_2 = 110°$, along the path $\phi_2 = 300° - \phi_1$ (contour line interval = 1 N-m).

$$\nabla_d = \begin{cases} [2\phi_1 - 424°, -1], & \phi_2 < (212° - \phi_1)^2 + 86° \\ [-2\phi_1 + 424°, 1], & \phi_2 > (212° - \phi_1)^2 + 86° \end{cases} \tag{3.14}$$

For this example we placed two identical extensional springs on the two-DOF Watt's linkage (Figure 3.5(C)) in addition to two torsional springs and used the optimization method to compute their properties. The potential energy in an extensional spring x is $\mathrm{PE}_x = \frac{1}{2}k_x(L_x - L_{0x})^2$, where k_x is the spring stiffness (units: N/m), L_x is the deformed length of the spring, and L_{0x} is the rest length, where the energy stored in the spring equals zero. With the extensional springs, the fluctuation in potential energy is reduced by 99.5% along the curved path, and the path is placed in a global $\mathrm{PE_T}$ valley. The gradient plot shows good agreement between $\nabla\mathrm{PE_T}$ and ∇_d.

3.3.2 Programming a Stable Configuration Using Superposition

For certain applications, it may be beneficial to add a stable configuration to a system that has already been designed to have a stable continuous equilibrium path. For one-DOF systems, constraints can be used to create one or more stable states at target configurations [78], and a similar

Table 3.3: Optimized spring properties for the two-DOF Watt's linkage, designed to have a stable configuration along a stable path.

	Rest Angle					
Path	Configuration	α_A	α_B	α_C	α_D	α_E
$\phi_2 = 90°$	$\phi_1 = 210°,\ \phi_2 = 90°$	210°	128°	77.5°	200°	90°
$\phi_2 = 300° - \phi_1$	$\phi_1 = 190°,\ \phi_2 = 110°$	190°	105°	70.5°	205°	110°

approach could be adapted to design multi-stable states in the multi-DOF systems. Here, we discuss a method for adding a stable configuration to a multi-DOF system with a continuous equilibrium path using superposition. To add a stable configuration, we implement an additional set of springs and set their rest angles to correspond with the desired configuration. The potential energy contribution of the additional set of springs is then superimposed with the potential energy due to gravity and the original optimized springs, resulting in a $\mathrm{PE_T}$ surface with a stable path and a stable configuration along that path. The stiffness of the additional springs affects how steeply $\mathrm{PE_T}$ increases when moving away from the stable configuration; high stiffness results in a steeper gradient. We designed the two-DOF Watt's linkage for a stable configuration where $\phi_1 = 210°$ and $\phi_2 = 90°$ along the path $\phi_2 = 90°$ (Figure 3.6(A)). While the path is still globally stable as originally designed, there is now a minimum in $\mathrm{PE_T}$ at the desired configuration. We also designed the Watt's linkage to have a stable configuration at $\phi_1 = 190°$ and $\phi_2 = 110°$ along the path $\phi_2 = 300° - \phi_1$ (Figure 3.6(B)). The spring properties for these examples are given in Table 3.3.

3.3.3 Programming Sequential Stable Paths

Being able to design multiple paths that occur in sequence is critical for the design of multi-functional systems, where distinct motions involving different combinations of DOFs are needed to accomplish a task. We designed the two-DOF Watt's linkage to have continuous equilibrium along two paths: first, ϕ_1 increases from 170° to 195° while ϕ_2 remains constant at 105°, then ϕ_1 stays at 195° as ϕ_2 decreases to 80° (Figure 3.5(D)). For this case, the desired gradient field ∇_d is divided into four regions:

$$\nabla_d = \begin{cases} [-1,-1], & \phi_1 < 195,\ \phi_2 < 105 \\ [0,1], & \phi_1 < 195,\ \phi_2 > 105 \\ [1,0], & \phi_1 > 195,\ \phi_2 < 105 \\ [1,-1], & \phi_1 > 195,\ \phi_2 > 105. \end{cases} \tag{3.15}$$

We add five internal torsional springs to the Watt's linkage and use the optimization framework

Table 3.4: Toolbox for various design scenarios.

<table>
<tr><th></th><th>Objective Function</th><th>Bounds</th><th>Constraints</th></tr>
<tr><td>Continuous Equilibrium</td><td>Eqn. 3.5</td><td rowspan="4">Eqn. 3.6, Eqn. 3.7</td><td>-</td></tr>
<tr><td>Stable Configuration</td><td>-</td><td>-</td></tr>
<tr><td>Stable C.E. Path</td><td>Eqn. 3.9</td><td>Eqn. 3.11</td></tr>
<tr><td>Seq. Stable C.E. Paths</td><td>Eqn. 3.9</td><td>Eqn. 3.11</td></tr>
</table>

to compute their properties. While the potential energy along the two paths is not perfectly constant, the fluctuation is still reduced to 93% of the case with no springs. Actuating the structure along these paths will require less energy, and the system will remain stable, as $\nabla \mathrm{PE_T}$ is aligned with ∇_d. This example focuses on designing two sequential paths for continuous equilibrium and does not specify the order or directionality of the paths, which can be controlled by adding stable states into the potential energy landscape as well as stable paths (this concept is explored more in Chapter 5).

3.4 Design examples

In this section, we demonstrate our design methodology through two examples. The first example expands upon the planar linkage results discussed in Section 3.3, where we model an excavator as a linkage with a continuous equilibrium path. The next example is a three-dimensional, five-fold origami vertex. Origami serves as design inspiration for many deployable and reconfigurable structures, and these examples demonstrate how such systems could be designed to have continuous equilibrium properties. These examples show how we can program a combination of stable states and stable paths. Table 3.4 summarizes the various design scenarios and which objective functions and constraints are used for each.

3.4.1 Excavator

A typical excavator has three DOFs, with hydraulic actuators used to move the boom, arm, and bucket [92]. We model an example of an excavator as a two-DOF linkage (Figure 3.7). We approximate the members of the excavator arm as rigid links connected by a four bar linkage. We designed the system to have continuous equilibrium along the path $\phi_2 = 5/12 * \phi_1 + 99.17°$, a typical motion that would be used for digging (Figure 3.7(B)). We added four torsional springs and two extensional springs to the system and optimized their properties to minimize the fluctuation of

$\mathrm{PE_T}$ along the path. The desired gradient field (used to formulate the stability constraint) is written as

$$\nabla_d = \begin{cases} [-1,1], & \phi_2 > 5/12\phi_1 + 99.17^\circ \\ [1,-1], & \phi_2 < 5/12\phi_1 + 99.17^\circ. \end{cases} \tag{3.16}$$

The dimensions of the excavator linkage are given in Figure 3.7(A). The members are modeled as rigid links with masses $m_{\text{Boom}} = 1710$ kg and $m_{\text{Arm}} = 1300$ kg respectively. The bucket is modeled as a lumped mass of $m_{\text{Bucket}} = 787$ kg. The weights of the four bar linkage and springs are neglected. The springs used to achieve continuous equilibrium (labels shown in Figure 3.7(C)) have the following properties: $\alpha_A = 0^\circ$, $\alpha_B = 146^\circ$, $\alpha_C = 360^\circ$, $\alpha_D = 360^\circ$, $\alpha_E = 13^\circ$, $k_A = 0$ N-m/rad, $k_B = 24506$ N-m/rad, $k_C = 0$ N-m/rad, $k_D = 15733$ N-m/rad, $k_E = 88464$ N-m/rad, $L_{01} = 1.95$ m, $L_{02} = 15$ m, $k_1 = 20759$ N/m, $k_2 = 4385$ N/m.

The resulting $\mathrm{PE_T}$ surface is flat compared to $\mathrm{PE_G}$, with a shallow valley along the desired path (Figure 3.7(B). Along the path, the fluctuation in $\mathrm{PE_T}$ is reduced by 66% from 22,152 N-m to 7,543 N-m. While the desired gradient is not matched well by $\nabla\mathrm{PE_T}$, the constraint is still satisfied, meaning that $\mathrm{PE_T}$ is in the range of directions from parallel to orthogonal to the path. While the path is not perfectly flat, the overall kinematic space is flattened, meaning reconfiguration along the path will require lower energy than the case without springs; additionally, if motions away from the path are desired, they can be reached with a small external force and the system will return to the path when the force is removed.

3.4.2 Five-fold Origami Vertex

The five-fold origami vertex shown in Figure 3.8 is a rigid-foldable origami structure with two DOFs defined by crease angles ϕ_1 and ϕ_2. We assume the structure consists of rigid panels connected by frictionless rotational hinges. The potential energy for a three-dimensional system with n panels is $\mathrm{PE_G} = \sum_i^n m_i * A_i * g * h_i$, where m_i is the mass distribution (units: N/m^2), A_i is the area, $g = 9.81$ m/s^2, and h_i is the height of the center of mass of panel i. Certain combinations of ϕ_1 and ϕ_2 are not viable due to panel contact (Figure 3.8(B)). The five-fold origami vertex is modeled as a 2 m-by-2 m sheet with uniform thickness. We assume the material to have a uniform mass density of 1 kg / m^2.

To design the five-fold vertex to have continuous equilibrium, we added four internal torsional springs along its crease lines, at locations A, B, C, and D (Figure 3.8(A)). Adding a spring along the fifth crease does not improve results and thus is omitted from this design. The optimized spring rest angles are $\alpha_A = 273^\circ$, $\alpha_B = 129^\circ$, $\alpha_C = 89^\circ$, and $\alpha_D = 62^\circ$; the optimized stiffnesses are $k_A = 7.99$, $k_B = 1.60$, $k_C = 0.00$, and $k_D = 2.64$ N-m/rad. The resulting $\mathrm{PE_T}$ surface is nearly

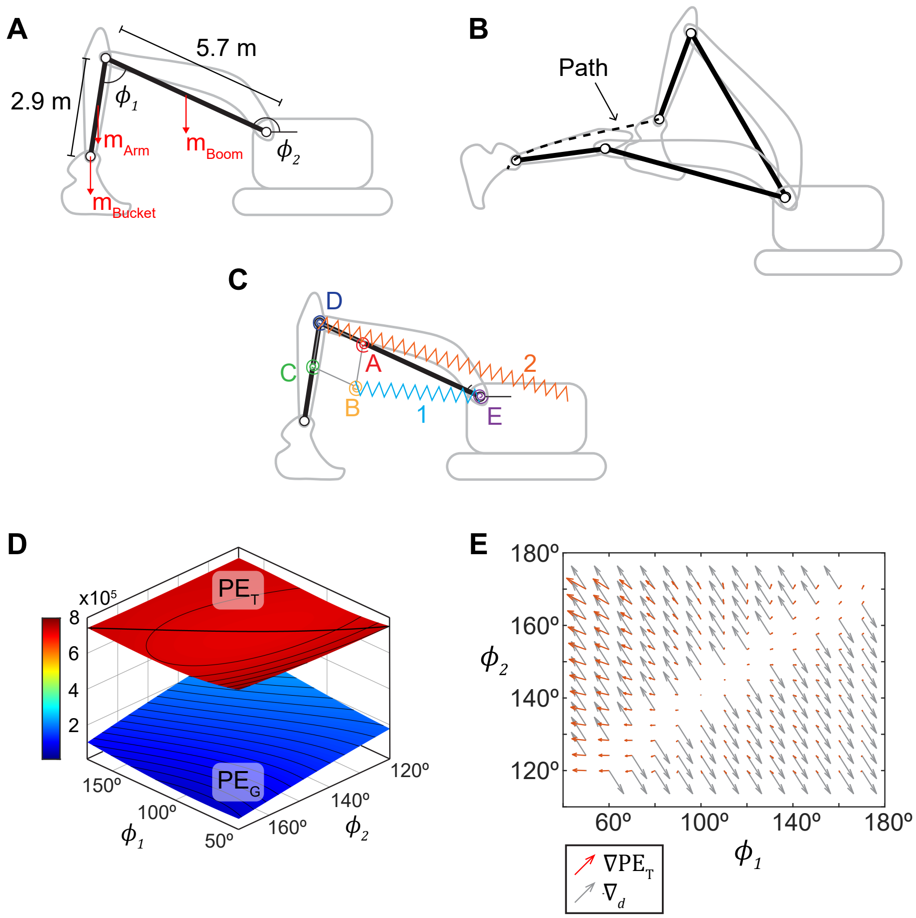

Figure 3.7: Designing a two-DOF excavator to have a continuous equilibrium path. (A) We model the excavator using rigid links with kinematics defined with ϕ_1 and ϕ_2. (B) We specify a path that represents a typical digging motion. (C) We add internal torsional, external torsional, internal extensional, and external extensional springs to the system and optimize their properties to achieve continuous equilibrium. (D) The total potential energy PE_T has a shallow valley along the desired path. The fluctuation in PE_T along the path is reduced by 66% (contour line interval = 10 kN-m). (E) The gradient field ∇_d represents the constraint applied to the optimization problem to ensure the stability of the path. The gradient of PE_T is aligned with ∇_d, especially for small ϕ_1 and large ϕ_2.

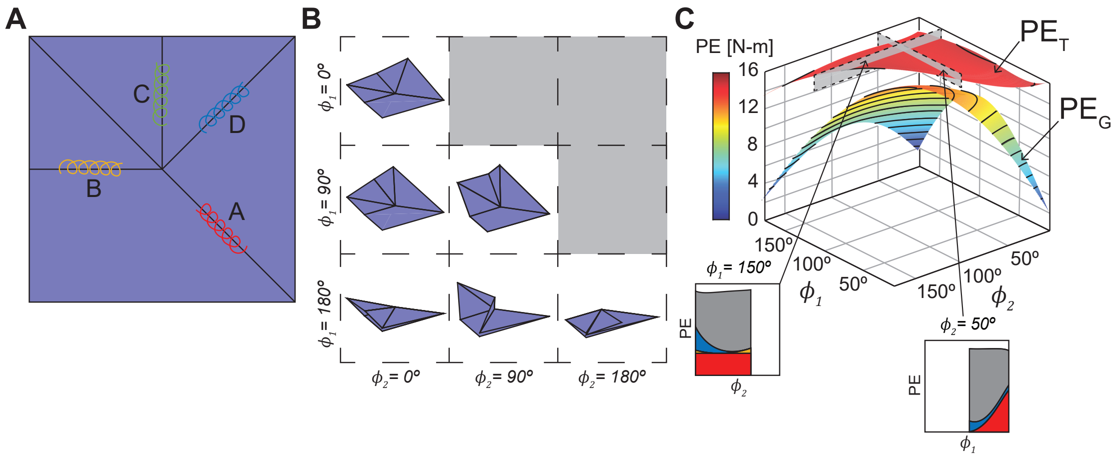

Figure 3.8: Designing a five-fold origami vertex to have continuous equilibrium. (A) Four internal torsional springs A, B, C, and D are placed on the crease lines of the origami vertex. (B) The five-fold origami vertex has two degrees of freedom, defined by ϕ_1 and ϕ_2. The kinematic space is limited due to panel contact and the boundary is illustrated here. (C) Adding the four optimized springs minimizes the fluctuation in total potential energy by 90%, resulting in a nearly flat PE_T surface (contour line interval = 1 N-m).

flat (Figure 3.8(C)), and the fluctuation in potential energy is reduced by 90% from the case with no springs.

3.5 Concluding Remarks

In this chapter, we presented a method for programming continuous equilibrium motions in multi-DOF systems. Using optimization, we can compute spring properties that minimize the fluctuation in potential energy throughout the kinematic space or along a desired path. The method can be used to design systems with stable paths, stable configurations, and sequential stable paths. We first demonstrate the method on one-, two-, and three-DOF Watt's linkages and design them to have continuous equilibrium throughout their entire kinematic space. We then focus on the two-DOF system, demonstrating the capability to program stable paths and configurations. We formulate an optimization constraint that is used to ensure the stability of a path by aligning the gradient of the potential energy space with a desired gradient field. With this constraint, small perturbations away from the path will not cause the system to deviate from the desired path and collapse. The examples shown in Section 3.4 demonstrate how the method can be used to design practical two- and three- dimensional systems.

The concepts in this paper provide a foundation for the design of multi-DOF reconfigurable structures that require significantly less energy for stable deployment and reconfiguration. Using our design method, designers can take advantage of the complex, functional motions that multi-DOF systems provide while maintaining stability and avoiding collapse. Programming a set of stable paths and configurations can help limit the infinite possibilities for motion and result in a system that gravitates back to a desired path without external forcing. Programming of continuous equilibrium can greatly improve the design, fabrication, and operation of multi-DOF reconfigurable structures by ensuring efficient actuation, desired motions, and stability under gravity. The principles presented here are scale-independent and relevant to multiple disciplines with potential applications in robotics, architecture, consumer goods, vehicle systems, and more.

CHAPTER 4

Applications of Continuous Equilibrium to Physical Linkages and Origami Systems

The optimization method presented in Chapter 2 of this dissertation can be used to design large-scale deployable and reconfigurable structures with reduced forces needed for actuation. However, aspects beyond the potential energy curve need to be considered to inform the practical implementation of these systems. In this chapter, mechanical models of linkages and origami systems are used to study the reduction in actuation forces when optimized springs are added. Physical prototypes support the computational results and demonstrate the effectiveness of the design method. Preliminary experimental results verify the reduction in forces needed for reconfiguration.

4.1 Simulations for Mechanical Modeling

The design framework used to transform reconfigurable structures into systems with continuous equilibrium is based on the potential energy contributions of gravity and adding springs. In reality, other components of a system will have an effect on the forces, stability, and deformation behavior. In this section, we use mechanical models that take into account effects such as stretching and bending of the linkage elements. From these models, we obtain the actuation force required to reconfigure a structure throughout its kinematic path. The mechanical models are formulated for systems with and without springs, and the spring properties are set to the values obtained from the continuous equilibrium optimization.

4.1.1 Mechanical Modeling of Linkage Systems with Torsional Springs

A variety of methods can be used for the structural analysis of linkages [93, 94, 95, 96] and here we take a traditional structural engineering approach using the stiffness method. To use the stiffness method to analyze linkages with springs, we constructed a stiffness matrix **[K]** with an additional rotational DOF. The formulation of the stiffness matrix is an adaptation of the formulation for

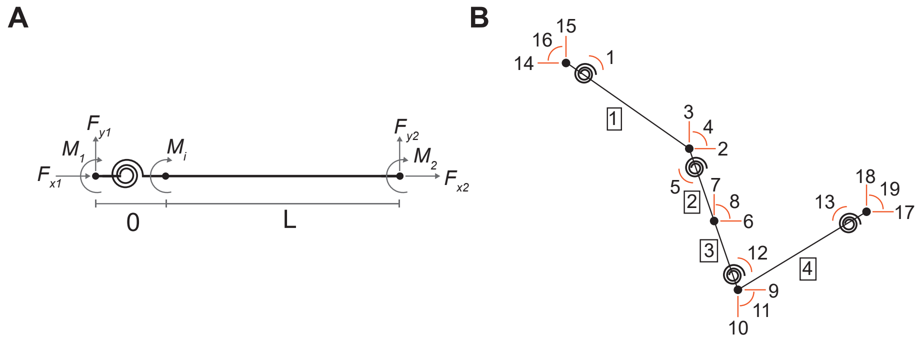

Figure 4.1: Using the stiffness method for modeling linkage systems. (A) To model the linkages with torsional springs, we use a frame member with an additional rotational degree of freedom (DOF) at one end. Each member has seven DOFs. (B) The DOFs for the Watt's linkage with four internal torsional springs. Members 1 and 2 have an additional rotational DOF at the i-node, and members 3 and 4 at the j-node.

flexible connections presented in McGuire et al [97]. Figure 4.1(A) shows the DOFs for one member with a flexible connection at the i-node. The dimensions of the local stiffness matrix for each member is 7x7. We use a de-coupled approach so that moments can be applied at the added rotational DOFs, representing the stress that is developed in the springs.

As an example, the DOFs of the Watt's linkage modeled with springs is shown in Figure 4.1(B). Say that member 1 has a spring at its i-node with stiffness k_A. The local stiffness matrix for member 1 is then:

$$
\begin{array}{r c}
\text{DOF :} & \begin{array}{ccccccc} 14 & 15 & 16 & 1 & 2 & 3 & 4 \end{array} \\
[\hat{k_1}] = & \begin{bmatrix}
\frac{EA}{L} & 0 & 0 & 0 & -\frac{EA}{L} & 0 & 0 \\
0 & \frac{12EI}{L^3} & 0 & \frac{6EI}{L^2} & 0 & -\frac{12EI}{L^3} & \frac{6EI}{L^2} \\
0 & 0 & k_A & -k_A & 0 & 0 & 0 \\
0 & \frac{6EI}{L^2} & -k_A & \frac{4EI}{L} + k_A & 0 & -\frac{6EI}{L^2} & \frac{2EI}{L} \\
-\frac{EA}{L} & 0 & 0 & 0 & \frac{EA}{L} & 0 & 0 \\
0 & -\frac{12EI}{L^3} & 0 & -\frac{6EI}{L^2} & 0 & -\frac{12EI}{L^3} & -\frac{6EI}{L^2} \\
0 & \frac{6EI}{L^2} & 0 & \frac{2EI}{L} & 0 & -\frac{6EI}{L^2} & \frac{4EI}{L}
\end{bmatrix}
\end{array}
$$

where E is the Young's Modulus, A is the member cross-sectional area, I is the moment of inertia, and L is the member length. For a member with a spring at its j-node, such as member 4, the additional DOF is included at that node. The local stiffness matrix for member 4 with a spring stiffness of k_D is then:

$$
\begin{array}{r c}
\text{DOF :} & \begin{array}{ccccccc} 9 & 10 & 11 & 17 & 18 & 19 & 13 \end{array} \\
[\hat{k_4}] = & \begin{bmatrix}
\frac{EA}{L} & 0 & 0 & -\frac{EA}{L} & 0 & 0 & 0 \\
0 & \frac{12EI}{L^3} & \frac{6EI}{L^2} & 0 & -\frac{12EI}{L^3} & 0 & \frac{6EI}{L^2} \\
0 & \frac{6EI}{L^2} & \frac{4EI}{L} & 0 & -\frac{6EI}{L^2} & 0 & \frac{2EI}{L} \\
-\frac{EA}{L} & 0 & 0 & \frac{EA}{L} & 0 & 0 & 0 \\
0 & -\frac{12EI}{L^3} & -\frac{6EI}{L^2} & 0 & \frac{12EI}{L^3} & 0 & -\frac{6EI}{L^2} \\
0 & 0 & 0 & 0 & 0 & k_D & -k_D \\
0 & \frac{6EI}{L^2} & \frac{2EI}{L} & 0 & -\frac{6EI}{L^2} & -k_D & \frac{4EI}{L} + k_D
\end{bmatrix}
\end{array}
$$

These local stiffness matrices are assembled into the global stiffness matrix **[K]** and used to solve for the nodal displacements and rotations $\{\delta\}$ = $[\mathbf{K}]^{-1}$$\{\mathrm{F}\}$, where $\{\mathrm{F}\}$ is a vector of applied loads. The external loads applied to the Watt's linkage are the gravity forces, which act downward at the center of mass of each of the bars, and the spring moments at each of the four spring locations. The total gravity force for a bar is $-mg$, where m is the mass of the bar and $g = 9.81$ m/s^2 is the acceleration due to gravity. The total gravity force on the bar is divided in two, where half of the force is applied at node i and half is applied at node j. The moment at spring j is equal to $k_j(\theta_j - \alpha_j)$, where k_j and α_j are found using optimization. The spring moment changes as the linkage moves through its the kinematic path, reflecting the spring moving toward or away from its rest angle.

The properties of the members are assumed to be $A = 0.0254$ m^2, $I = \frac{1}{12}(0.0254)(0.0254^3)$ m^4, and $E = 200$ GPa unless otherwise noted. For the Watt's linkage, members 1 and 4 have a length of 0.3 m, and members 2 and 3 have a length of 0.15 m.

4.1.2 Reduced Actuation Forces

We used the stiffness matrix formulation to compute the forces required to reconfigure the Scissor Mechanism and Watt's linkage. Since the stiffness method assumes small displacements, we use an iterative approach. First, we apply the gravity load and compute the resulting displacements. We then incrementally increase an external load (representing the actuation force) until the displacements are negligible. This external force is thus the force required for the system to be in equilibrium at the desired configuration. To obtain actuation force values for the systems without springs, we implement a small spring stiffness of 0.005 N-m/rad and use the same stiffness matrix formulation. This fictitious spring stiffness is much smaller than a typical spring stiffness used to enable continuous equilibrium.

We first investigate the actuation force needed to reconfigure the Scissor Mechanism, comparing the structure with no springs to the structure with four internal torsional springs at locations A, B, C, and D (Figure 4.2(A)). For the Scissor Mechanism, we apply an external actuation force F_x at the top right node (node 4 in Figure 4.2(B)). Gravity is modeled as two lumped forces at nodes 2 and 3. For the Scissor Mechanism without springs, we can calculate the analytical solution for F_x using equilibrium. First, setting the sum of the forces in the y-direction equal to zero, we see that $F_y = F_g/2$. Next, we can solve for F_x using the method of joints at node 1:

$$F_y + F_{12}\sin\phi = 0 \tag{4.1}$$

$$F_{12} = \frac{F_g}{2\sin\phi} \tag{4.2}$$

$$F_x + F_{12}\cos\phi = 0 \tag{4.3}$$

$$F_x = \frac{F_g}{2\tan\phi} \tag{4.4}$$

This analytical solution is plotted as the dashed line in Figure 4.2(C). Using the stiffness method, the computed F_x for the system without springs matches the expected force value. We compared the actuation force without springs to the force needed to reconfigure the Scissor Mechanism with four internal torsional springs, with properties equivalent to those given in Table 2.8. With the optimized springs, F_x is reduced by 45% on average compared to the case without springs (Figure 4.2(C)). For the Scissor Mechanism with and without springs, we confirmed that the force value matches with the first derivative of the potential energy ($F = -\delta\text{PE}/\delta\text{x}$) (Figure 4.3).

For the Watt's linkage, we apply a vertical actuation force F_y at the top node (location B in

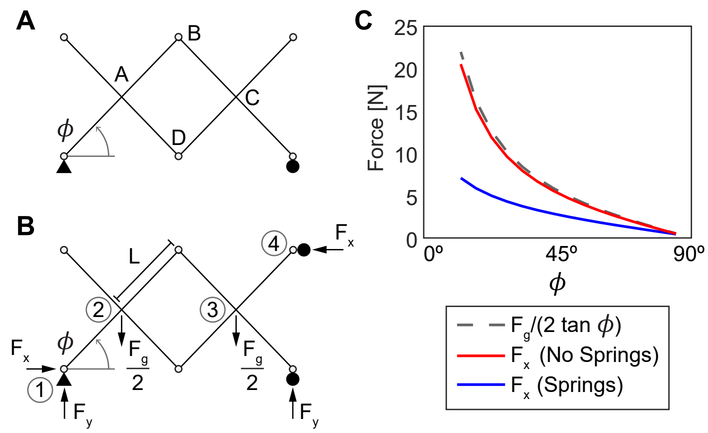

Figure 4.2: Actuation forces needed to reconfigure the Scissor Mechanism. (A) The Scissor Mechanism is modeled without springs and with internal torsional springs at locations A, B, C, and D. (B) Free-body diagram of the Scissor Mechanism. The actuation force is applied as an external horizontal load at node 4. (C) Actuation force for the Scissor Mechanism. The computed F_x for the system without springs matches the analytical solution derived from the free-body diagram. The F_x for the system with springs is reduced.

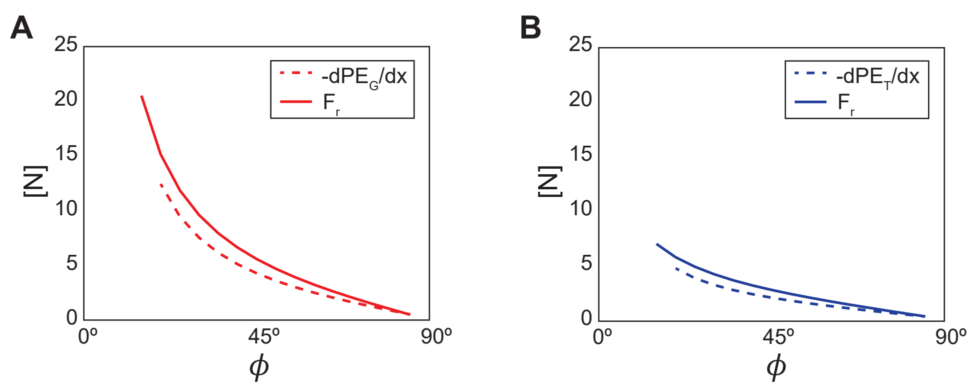

Figure 4.3: Force compared to differential of the potential energy for the Scissor Mechanism with (A) no springs, and (B) with springs.

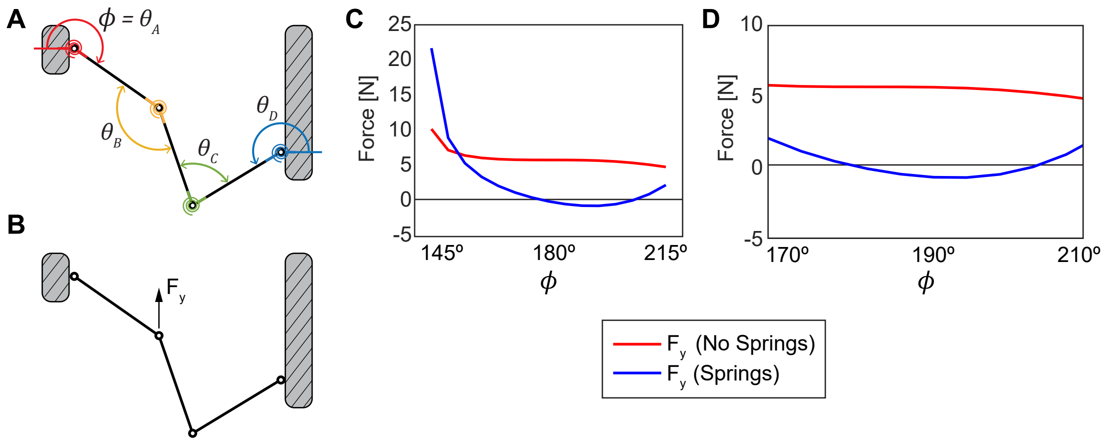

Figure 4.4: Actuation forces needed to reconfigure the Watt's linkage. (A) The Watt's linkage is modeled without springs and with itnernal torsional springs at locations A, B, C, and D. (B) The actuation force is applied as an external vertical load. (C) Actuation force for the Watt's linkage. With springs, F_y is reduced for most of the kinematic path. As ϕ approaches $145°$, the path of the Watt's linkage is no longer vertical and F_y approaches infinity. (D) For the center of the kinematic path, the actuation force is reduced by 59% on average for the system with springs.

Figure 4.4(A-B)). Gravity is modeled as a lumped force at each node. Using the stiffness method, we compare the actuation force needed to reconfigure the Watt's linkage without springs and with four internal torsional springs at locations A, B, C, and D. With springs, F_y is reduced for the majority of the kinematic path when compared to the system without springs. As ϕ approaches $145°$, F_y increases exponentially. This is because as $\phi \to 145°$, the center of the Watt's linkage deviates from a straight vertical path. For small ϕ, a vertical force is not sufficient to reconfigure the linkage, and a horizontal component (not captured in the model) is needed.In the center of the kinematic path ($\phi = 170°$ to $200°$, the actuation force is reduced by an average of 59%. For the Watt's linkage with and without springs, we confirmed that the force value matches with the first derivative of the potential energy (Figure 4.5).

4.1.3 Mechanical Modeling of Origami Systems

For the mechanical modeling of origami structures, we use the Sequentially Working Origami Multi-Physics Simulator (SWOMPS) package because it enables sequential loading with multiple numerical loading methods [98]. It is based on the bar and hinge model, which models origami and kirigami structures as pin-jointed assemblages [31]. It can capture in-plane deformations, crease folding, and panel bending seen in origami structures [99, 100, 101]. The stiffness of the system, used to formulate equilibrium equations and solve for a force or displacement response, is comprised of contributions from the following three components: bar elements that capture in-

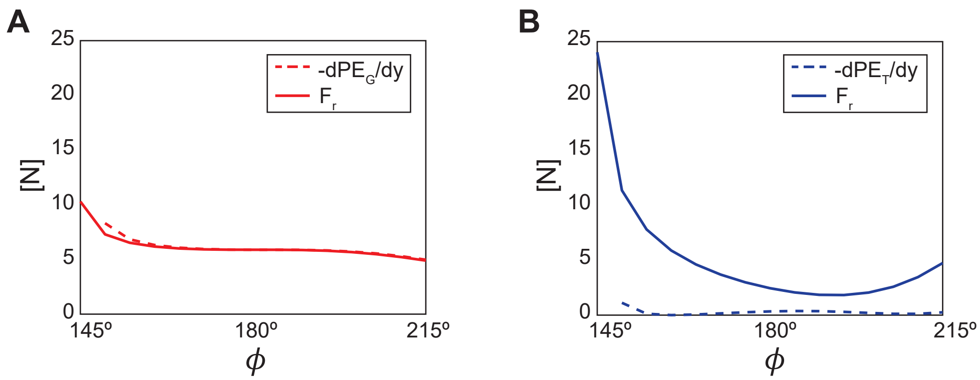

Figure 4.5: Force compared to differential of the potential energy for the Watt's Linkage with (A) no springs, and (B) with springs.

plane stretching and shearing deformations; folding hinges that capture folding at the crease lines; and bending hinges that capture bending in the origami panels. The total strain energy U of the system is a sum of these three contributions:

$$U = U_S + U_F + U_B,$$

where U_S is the strain energy due to bar stretching, U_F is the energy due to crease folding, and U_B is the energy due to panel bending. In this section, we use the bar and hinge model to confirm our findings from the optimization framework, where panels are assumed to be rigid. Additionally, we use the mechanical model to explore the forces required to reconfigure origami structures that have been designed to have continuous equilibrium. We are able to directly define the stiffness of the origami crease lines to equal the optimized stiffness of the springs. For a crease where a spring is added, the spring stiffness is incorporated by defining the crease thickness t as:

$$t = (4 * W * k/E)^{1/3},$$

where W = 0.01 m is the width of the crease, k is the spring stiffness (obtained from the optimization), and $E = 2$ GPA is the Young's modulus. The origami panels are modeled using the following material properties: E = 2 GPa, $\rho = 1200$ kg/m^3, and thickness = 0.0105 m. The rest angle α of a torsional spring is also specified in the bar and hinge model. Typically, the model assumes that crease lines have zero bending energy at the flat state, but any angle can be specified, so we set the rest angle to equal the value obtained from the optimization.

To capture the effects of both gravity and external loads, we use two loading phases. First, the entire structure is supported and gravity is applied using a Newton-Raphson iterative scheme.

Next, the reconfiguration is modeled using a displacement controlled method. The gravity load remains applied during this second step. The resultant force developed at the prescribed nodes during the second loading step is the force required for reconfiguration, or *actuation force*.

4.1.4 Reduced Actuation Forces

The first origami structure we investigated was a single origami crease (Figure 4.6). We model the crease as two panels with side length $L = 0.3$ m, connected by one crease line. One panel is pinned at four corners and the other is free to fold about the crease line (Figure 4.6(A)). A free-body diagram of the structure is shown in Figure 4.6(B). The gravity of the free panel can be represented as a lumped force F_g, acting at the top two nodes. As the displacement controlled scheme is used to move the free panel through its kinematic path (defined by ϕ), a moment develops at the crease line (M_s) and a resultant force F_r develops at the top nodes. With this simple example, we can solve analytically for F_r in the case where the crease line has no stiffness (i.e., a typical origami crease) and the case where it does have stiffness (when a spring is added). Setting the sum of the moments about the crease equal to zero, we can solve for equilibrium as

$$\circlearrowleft + \sum M_{\text{crease}} = 0 \tag{4.5}$$

$$M_s + F_r L \cos\phi - F_g L \cos\phi = 0. \tag{4.6}$$

If the crease line has no stiffness (no spring), then $M_s = 0$ and $F_r = F_g$; the resultant force is equal to gravity acting on the panel. If the crease line has some stiffness and $M_s > 0$, then $F_r < F_g$. We can interpret the resultant force F_r as the actuation force needed to reconfigure the structure through its kinematic path from $0° < \phi < 90°$.

We added a torsional spring along the crease line and used the optimization framework to design it to have continuous equilibrium. The spring stiffness is 1.42 N-m/rad and the rest angle is $90°$. These properties are specified in the bar and hinge model, so that the mechanical behavior of the structure includes the effect of the spring. Figure 4.6(C) shows F_r obtained using the SWOMPS package for the crease with and without a spring. When the system does not have a spring, the plot shows good agreement with the analytical solution, with $F_r = F_g$. When the spring is added, F_r is indeed lower than F_g; it is reduced by 90% on average. In addition to the displacement controlled method, we also used the Newton-Raphson solver for the second loading step (NR in Figure 4.6(C)) which gives the same result.

We can also extract the potential energy of the system from the bar and hinge model and compare it to the optimized potential energy curve (Figure 4.6(D)). The bar and hinge model computes

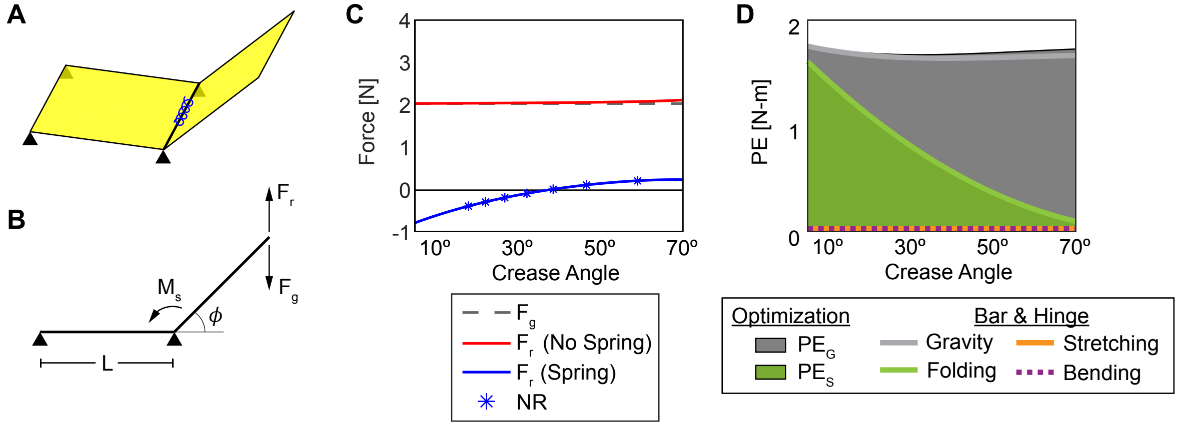

Figure 4.6: Mechanical simulation of a single origami crease. (A) Two panels with side length L are connected by one crease line. (B) The forces and moments acting on the free panel are gravity (F_g), the spring added to the crease line (M_s), and the resultant force F_r which develops as the panel is moved through its kinematic path ψ. (C) Without the spring, $F_r = F_g$. With the spring, $F_r < F_g$. Using a Newton-Raphson (NR) force controlled scheme gives the same result. (D) The potential energy breakdown of the single crease. There is good agreement between the optimization framework and bar and hinge model.

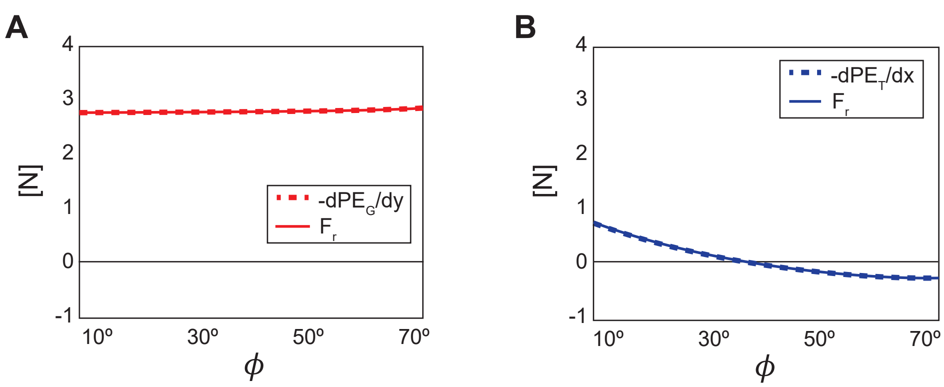

Figure 4.7: Force from the simulations compared to differential of the potential energy for an origami crease with (A) no springs, and (B) with springs.

energy due to bar stretching, crease folding, and panel bending. For the single origami crease with a spring, the model shows negligible energy due to stretching and bending, with the only energy (other than gravity) resulting from crease folding. These results match well with the optimized PE curve, even when taking into consideration the mechanical effects of a physical system. For the origami crease with and without springs, we confirmed that the force value matches with the first derivative of the potential energy (Figure 4.7).

The second origami structure we studied was the Miura-ori unit cell, the base of many origami structures [88]. The Miura-ori cell consists of four parallelogram panels with side lengths $L = 0.3$ m (Figure 4.8(A)). The structure begins as a flat sheet and can be folded into a second flat state (Figure 4.8(B)). Using the SWOMPS package, we use the displacement controlled scheme to apply a vertical displacement at the center node, where the resultant force F_r develops.

For continuous equilibrium, we add torsional springs to two crease lines of the Miura-ori cell. The springs are identical and have a stiffness of 0.62 N-m/rad and a rest angle of 0°, corresponding to a fully folded state. The force output from the bar and hinge model shows similar trends to those seen with the single crease origami. When no springs are added, $F_r = F_g$; the force required to move the structure through its kinematic path is equal to the force of gravity acting on it (Figure 4.8(C)). When springs are added with proper rest angles and stiffness, $F_r < F_g$. Thus, adding optimized springs reduces the actuation force required for reconfiguration. We again confirm these results with the Newton-Raphson (NR) solver. As the structure is folded there is no stretching or bending energy developed in the structure, and the potential energy output matches well with the optimized PE curve (Figure 4.8(D)). For the Miura-ori cell with and without springs, we confirmed that the force value matches with the first derivative of the potential energy (Figure 4.9).

4.2 Prototype Fabrication

In this section, we apply the continuous equilibrium design method to design and fabricate physical prototypes. In general, there are many sets of springs that can achieve the desired continuous equilibrium behavior for any one system. For example, using one spring with stiffness k has the same effect as using four springs with stiffness $k/4$ in a fully symmetric system, such as the Scissor Mechanism. All of the springs that were chosen for the prototypes in this chapter are one possible set and have properties that are approximate. In theory, custom springs with exact properties could be fabricated to perfectly achieve continuous equilibrium.

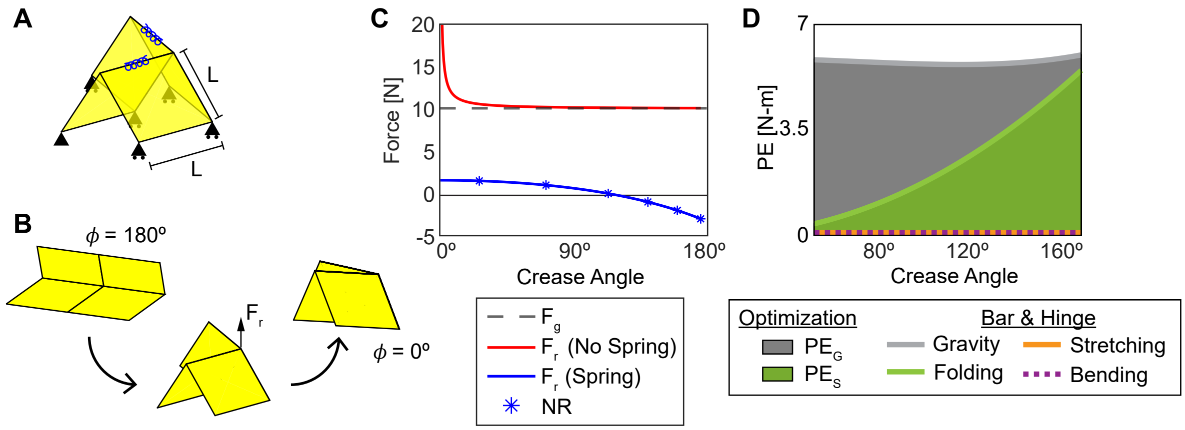

Figure 4.8: Mechanical simulation of the Miura-ori cell. (A) One vertex is pinned and five others have roller supports. (B) To reconfigure the Miura-ori cell from flat ($\phi = 180°$) to folded ($\phi = 0°$), a displacement is applied at the center node, and a resultant force F_r develops. (C) Without springs, $F_r = F_g$. With springs, $F_r < F_g$. Using a Newton-Raphson (NR) force controlled scheme gives the same result. (D) The potential energy breakdown of the Miura-ori cell. There is good agreement between the optimization framework and bar and hinge model.

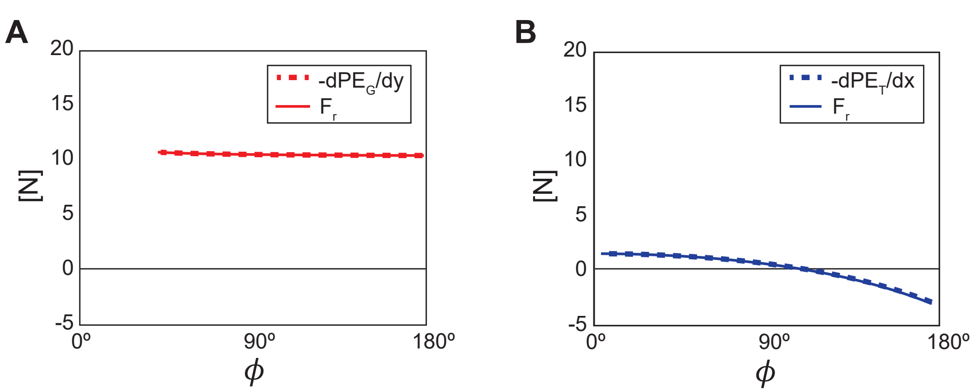

Figure 4.9: Force from the simulations compared to differential of the potential energy for a Miura-ori cell with (A) no springs, and (B) with springs.

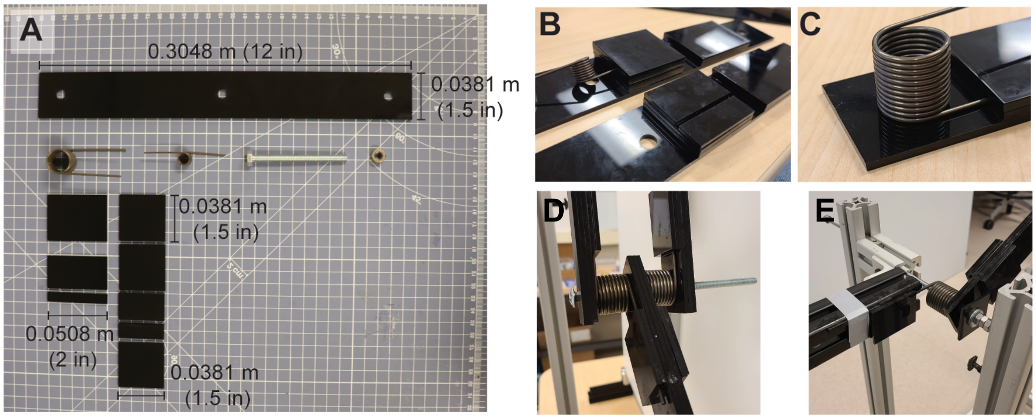

Figure 4.10: Linkage prototype fabrication. (A) Components of the Scissor Mechanism and Watt's linkage prototypes. The members and attachment pieces are cut from acrylic sheets. The members are connected using bolts. (B-C) Spring attachment methods for the Scissor Mechanism. (D) For the Watt's linkage, two springs were used at locations B, C, and D to achieve the required spring stiffness. (E) For the system that can be re-oriented, an external torsional spring was installed with one end connected to the Watt's linkage at location A and one end connected to a horizontal bar (shown in black). An internal spring was not used at location A, because it does not add a significant influence on the overall system behavior (see Figure 2.1)

4.2.1 Design Method

The following steps were used to implement the continuous equilibrium design method to design physical prototypes.

1. **Compute system kinematics.** First, obtain the system kinematics using geometric relationships. For systems with more complex motion, kinematics can be obtained by simulating the system using the bar and hinge model.

2. **Estimate potential energy due to gravity.** Based on the material properties and geometry, calculate the potential energy due to gravity (PE_G) due to the structure and springs.

3. **Run optimization to compute spring properties.** The inputs to the optimization problem are the system kinematics, spring locations, and PE_G. The outputs are the spring rest positions and stiffnesses.

4. **Compare optimized spring properties with available inventory and choose springs.** For the physical models shown in this chapter, the springs were purchased online from McMaster-Carr. Naturally, this limited the available spring properties. At this stage, if there is not a close match available in the inventory, return to step 2 and adjust the design. The

most common adjustment is to increase the weight of the system by adding more material to each component, or to utilize symmetry to increase or decrease the total number of springs.

5. Design spring connections. Once springs have been chosen, use the spring geometry (rest position, diameter, and wire thickness) to design connections. Estimate the weight of the springs and connections using material properties and geometry.

6. Refine design. Return to step 3, using the potential energy due to gravity including the weights of the springs and spring connections as the input to the optimization. Compare the new optimized spring properties with those of the springs chosen in step 4. If they are significantly different, repeat steps 4 and 5. If they are sufficiently similar, continue to step 7.

7. Assemble system with springs. At this point, the system can be reconfigured through its kinematic path and the quality of the continuous equilibrium behavior can be evaluated.

4.2.2 Linkage Prototype Fabrication

Physical prototypes of the Watt's linkage and Scissor Mechanism were fabricated as proof-of-concept 2D continuous equilibrium systems. Linkage members were cut from acrylic sheets. Torsion springs were purchased from McMaster-Carr and attached using acrylic pieces.

4.2.2.1 Scissor Mechanism

We fabricated two models of the Scissor Mechanism: one without springs and one with four internal torsional springs. The members of the linkages were fabricated using acrylic sheets with thickness = 2.7 mm (0.106"), length = 0.3048 m (12") and width = 0.0381 m (1.5") (Figure 4.10(A)). The sheets were glued together to create members with a total thickness of 0.0162 m (0.638"). Additional acrylic pieces were used to attach the springs. Members were connected using bolts and nuts and a low-friction frame was built to support the linkages. The computed optimized stiffness of the springs was 0.09 N-m/rad, and we used springs with a stiffness of 0.1 N-m/rad in the prototype. Two of the springs have a rest angle (optimized and used values) of $180°$ (Figure 4.10(B)) and two have a rest angle of $0°$ (Figure 4.10(C)). Note that although the dimensions of the two types of springs are different, they have equivalent torsional stiffness.

The potential energy analysis of the Scissor Mechanism (discussed in Section 2.5) showed that adding optimized springs reduces the fluctuation in potential energy by 88% (Figure 2.4). While the prototype without springs collapses due to gravity (Video A.1), the prototype with optimized springs can be reconfigured easily and is stable at any position along its kinematic path (Video A.2). From a practical perspective, the 88% improvement for the Scissor Mechanism is sufficient to improve stability.

Table 4.1: Spring properties (calculated and used values) for the physical model of the Watt's linkage with four internal torsional springs, optimized for $\psi = 0°$.

	Stiffness [N-m/rad]		Rest Angle	
Location	Calculated	Used	Calculated	Used
A	0.315	0.376	$192°$	$200°$
B	1.07	1.51	$142°$	$135°$
C	1.12	1.51	$158°$	$135°$
D	1.87	2.45	$139°$	$135°$

4.2.2.2 Watt's Linkage

We fabricated three versions of the Watt's linkage: one with no springs, one with four internal torsional springs, and one with four internal and one external torsional spring. The members of the linkages were fabricated using acrylic sheets with thickness = 2.7 mm (0.106"), length = 0.3048 m (12") and width = 0.0381 m (1.5"). The sheets were glued together to create members with a total thickness of 0.0081 m (0.329"). Additional acrylic pieces were used to attach the springs. Members were connected using bolts.

Without springs, the Watt's linkage collapses under gravity when a supporting force is removed (Video A.3). When the internal torsional springs with optimized properties are installed at locations A, B, C, and D, the linkage can be easily reconfigured into any position along its kinematic path (Video A.4). With springs, the linkage remains in the configuration in which it was placed and needs no additional forces to maintain its position. The spring properties for the model with four internal torsional springs are presented in Table 4.1. For the springs at locations B, C, and D, two springs of equal stiffness were used to create a composite spring with the total stiffness needed (Figure 4.10(D)).

The Watt's linkage can be reoriented by rotating the system about the left-side support, as discussed in Section 2.4. Without springs, the Watt's linkage at $\psi = 45°$ and $90°$ collapses under gravity when a supporting force is removed (Videos A.5 and A.6). At different orientations, the potential energy due to gravity changes, but the potential energy contributions of internal springs do not. Therefore, we add an external torsional spring to allow continuous equilibrium to be reached at orientations from $0°$ to $90°$. The spring parameters are presented in Table 4.2. Despite using springs with some deviation from the calculated parameters, our results show that the system with springs exhibits continuous equilibrium properties and the system remains stable throughout its kinematic path in different orientations (Figure 4.11, Videos A.7 and A.8).

Table 4.2: Spring properties (calculated and used values) for the physical model of the Watt's linkage with four internal torsional springs and one external torsional spring, optimized for $0^\circ \leq \psi \leq 90^\circ$.

	Stiffness [N-m/rad]		Rest Angle	
Location	Calculated	Used	Calculated	Used
A	0.267	-	187°	-
B	1.87	1.51	144°	135°
C	1.64	1.51	159°	135°
D	2.48	2.45	137°	135°
External	1.04	1.22	191°	135°

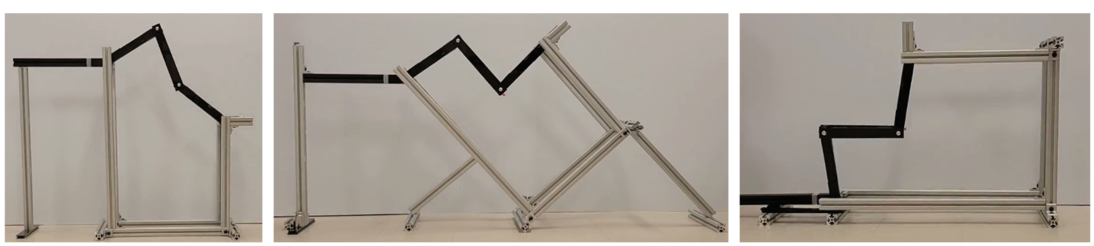

ψ = 0° ψ = 45° ψ = 90°

Figure 4.11: Physical prototype of the Watt's linkage. With internal and external torsional springs, the Watt's linkage can be reconfigured at $\psi = 0^\circ$, 45°, and 90° without collapsing.

4.2.3 Origami Prototype Fabrication

Physical prototypes of a single origami crease and a Miura-ori unit cell were fabricated as proof-of-concept 3D continuous equilibrium systems. Origami panels were cut from acrylic sheets and torsion springs were purchased from McMaster-Carr and attached using acrylic pieces. The crease lines are connected using tape to create an origami structure with flexible, frictionless creases.

4.2.3.1 Origami Crease

A single origami crease was fabricated using two panels (thickness = 1/8") with side lengths equal to 12" (Figure 4.12). Using the optimization framework presented in Chapter 2, we computed the stiffness and rest angle of the torsional spring added to the crease. The stiffness is 0.3 N-m/rad and the rest angle is $90°$. One panel is fixed and the other is free to rotate about the crease line. Without the spring, the crease has no stiffness and the panel collapses. With the spring, the panel can be easily reconfigured to any position and remains stable.

4.2.3.2 Miura-ori Cell

The origami panels are made from 1/8" thick acrylic sheets, with side lengths equal to 8". The crease lines are connected using tape, creating a crease line with negligible stiffness. We use a hinge shift technique [48] with added material along two crease lines in order to achieve the correct folding motions with the thick material and to give clearance for the spring attachments (Figure 4.13(A)). The springs are held in place using built-up acrylic pieces (Figure 4.13(B)).

Using the optimization framework, we computed the properties of the two identical springs added to the crease lines. The stiffness is 0.5 N-m/rad and the rest angle is $0°$. The full system assembled with springs has full mobility to reconfigure from a flat sheet to a folded state, remaining stable at all intermediate configurations (Figure 4.13(C)).

4.3 Experimental Testing

Preliminary experimental testing of several linkages and origami systems demonstrates the reduction in energy required to reconfigure systems which are in continuous equilibrium. In each case, a load cell is used to measure the force needed to move the system through a portion of its kinematic path.

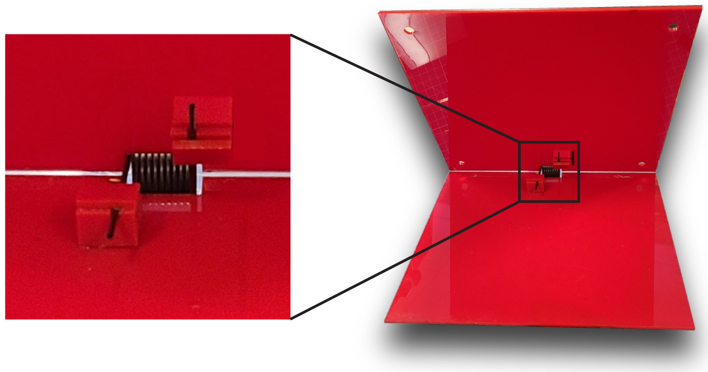

Figure 4.12: Physical prototype of a single origami crease. The spring was added to the crease and attached using built up acrylic pieces.

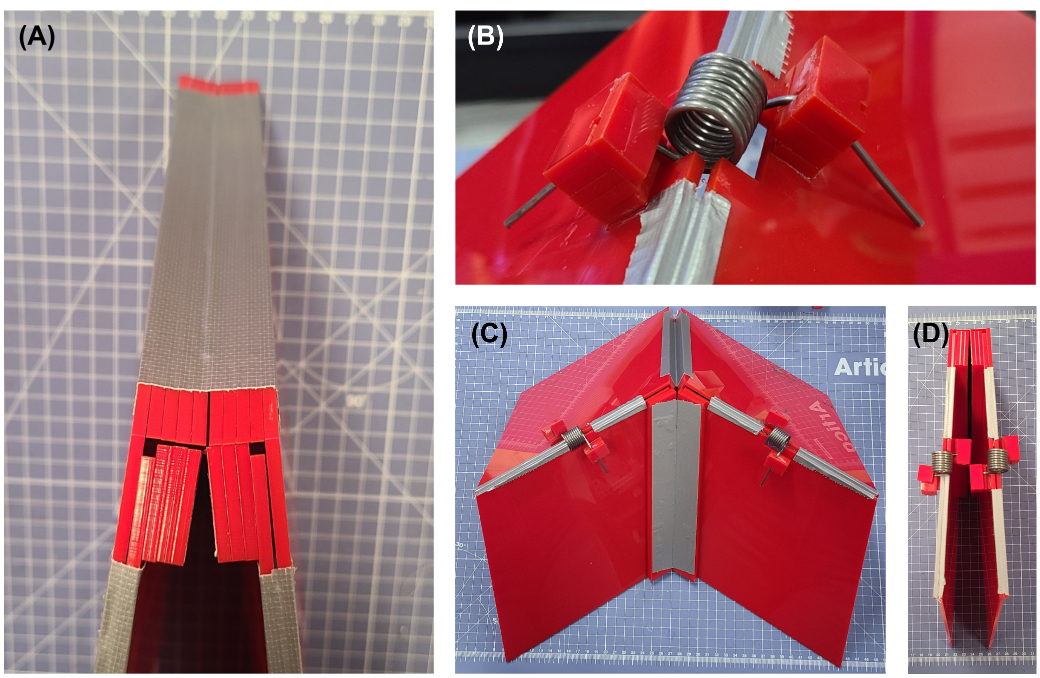

Figure 4.13: Physical prototype of the Miura-ori unit cell. (A) The Miura-ori was designed using a hinge shift method with added material along two crease lines. The creases are connected with tape. (B) Springs were added to two creases and attached with acrylic pieces. (C) The assembled Miura-ori cell with springs can reconfigure from a flat sheet to a fully folded state (D).

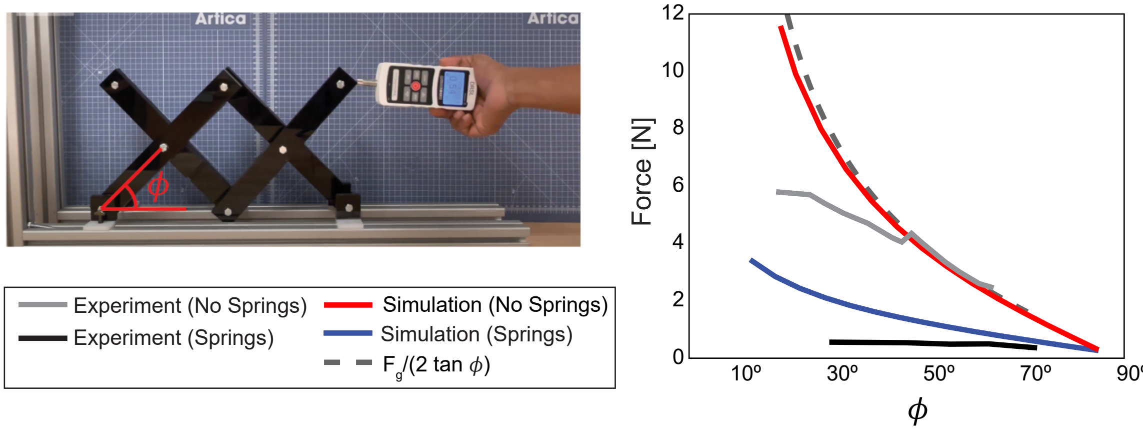

Figure 4.14: Testing of the Scissor Mechanism prototype. A force gauge was used to apply a horizontal force to reconfigure the Scissor Mechanism. The measured force of the system without springs matches the analytical solution $(F_g/(2\tan(\phi)))$ well for $\phi > 45°$. With springs, the actuation force is reduced even more than predicted by the computational model.

4.3.1 Scissor Mechanism

To reconfigure the Scissor Mechanism, we applied a horizontal force. The force required to reconfigure the model with springs are lower than those required to reconfigure the model without springs (Figure 4.14). We can calculate the analytical solution for the horizontal force required to prevent the Scissor Mechanism from collapsing: $F_x = \frac{F_g}{2\tan\phi}$ (dotted line in Figure 4.14). The data matches this solution well for $45° \leq \phi \leq 90°$. For $\phi < 45°$, the load cell is not able to capture the increase in F_x, which tends towards infinity as $\phi \longrightarrow 0$. In the physical testing of the system with no springs, we have to hold the load cell at an angle so that we can move the system, and this angle reduces the recorded force for $\phi < 45°$. The experimental results for the Scissor Mechanism with springs give lower forces for actuation than the simulation using the stiffness method.

4.3.2 Watt's Linkage

To reconfigure the Watt's linkage, we apply a vertical force (pulling or pushing). The direction of reconfiguration (up or down along the kinematic path) affects the magnitude of the force. The force increases as the Watt's linkage moves further from $\phi = 180°$ and the center point of the floating link no longer traces a vertical line. The force for the system with springs is nearly centered around 0 N, with higher forces developing at both ends of the kinematic path (positive force for pulling up, negative force for pushing down), where the linkage deviates from a straight vertical path. Friction in the system also contributes to the increase in force at the ends of the kinematic path; improved fabrication methods could minimize the effect of friction. On average, the forces

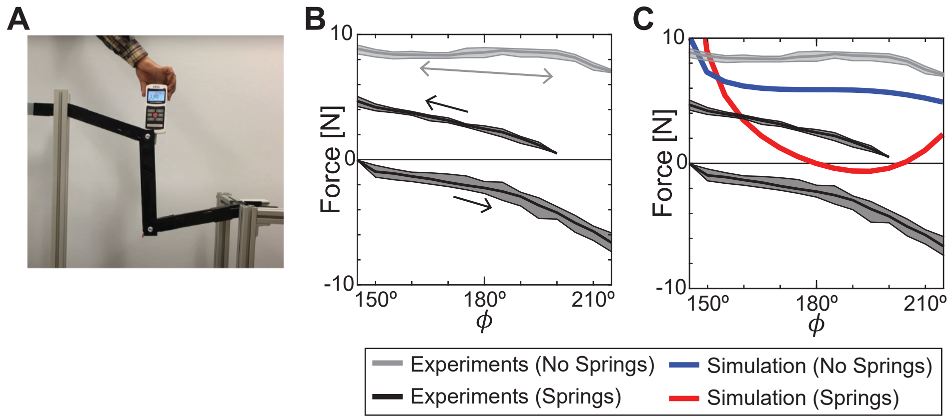

Figure 4.15: Testing of the Watt's linkage prototype. (A) To reconfigure the Watt's linkage, a vertical force was applied to the top node and the force was measured using a force gauge. (B) With springs, the force is reduced by approximately 70% on average compared to the case without springs. There is a hysteresis in the force with springs based on the movement direction. (C) The computational model and experimental results agree well for $160° \leq \phi \leq 200°$, where the computational model traces the average value for the system with springs.

for the system with springs are reduced by approximately 70% than the system without springs (Figure 4.15). The simulation results obtained from the stiffness method are shown along with the experimental results in Figure 4.15(C). For $160 \leq \phi \leq 200°$, the computational results trace the center of the hysteresis that occurs in physical testing of the system with springs. The simulation underestimates the forces required to actuate the system without springs. The higher forces in the physical prototype are likely due to friction and fabrication imperfections.

4.3.3 Origami Crease

To measure the actuation force required to reconfigure the origami crease, the bottom panel was fixed to a frame and the vertical force was applied to the top of the free panel (Figure 4.16(A)). Additional weight was added to the free panel of the crease in order to increase PE_G so that a spring from our available inventory could be used to achieve continuous equilibrium. The weight was added using black binder clips. The spring added to the prototype has a stiffness of 0.3 N-m/rad and rest angle of $90°$. The measured force to reconfigure the system with springs matches the force obtained from the SWOMPS simulation (Figure 4.16(B)).

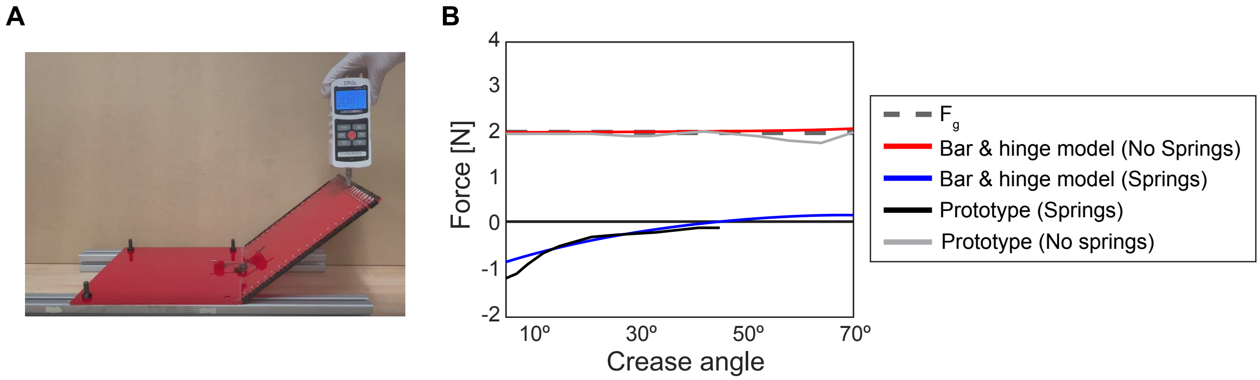

Figure 4.16: Testing the origami crease prototype. (A) A vertical force was applied to the free panel to reconfigure the crease. (B) The experimental results match well with the simulation results and are reduced compared to the gravity load.

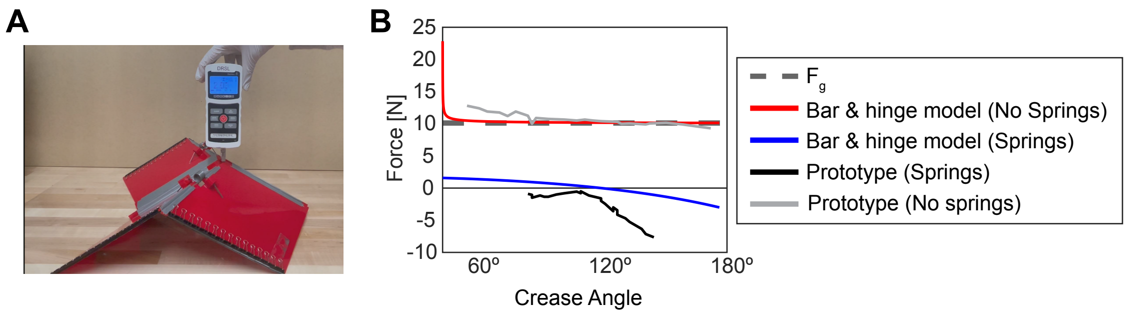

Figure 4.17: Testing the Miura-ori cell prototype. (A) A vertical force was applied to reconfigure the Miura-ori cell. (B) Although results were only obtained for a small portion of the kinematic path, the preliminary experiment shows reduced forces for the structure with springs.

4.3.4 Miura-ori Cell

The Miura-ori unit cell prototype was testing by applying a vertical force to the center node (Figure 4.17(A)). A low-friction surface was created by placing a sheet of Mylar plastic on the testing surface. The center node only moved in the z-direction during testing, and the six nodes in contact with the low-friction surface are free to move in the x- and y- directions. Two internal torsional springs were added to the prototype, each with stiffness 0.5 N-m/rad and rest angle equal to 0°. Additional weight was added to the prototype to accommodate the use of available springs. For testing, we were only able to capture a small portion of the kinematic path, but the forces required to actuate the system with springs are close to those predicted by the simulation (4.17(B)).

4.4 Stiffness and Locking

One possible use for continuous equilibrium structures is to provide stable deployment of load-bearing structures. Such structures could be fabricated off-site, transported, and assembled on site. Designing the assembly motion to be a continuous equilibrium path would be beneficial for improving the ease of construction and reduce the need for external supports. Once deployed, the structure could then be locked in place and be used in load-bearing applications.

We use the Watt's linkage as an example to explore the concept of deploying a continuous equilibrium structure and then locking its rotational DOFs to provide stiffness. To compute the stiffness of the Watt's linkage, we applied unit loads $P = 1.0$ to the centroid of the floating link, along with the gravity load and spring moments. Using the stiffness method described in Section 4.1.1, we solved for the resulting displacements $\{\delta\}$ and calculated a structural stiffness equal to $\{\delta\}/\{F\}$.

Figures 4.18(A) and (B) show the structural stiffness of the Watt's linkage in the horizontal and vertical directions, respectively. With the addition of springs, the linkage has high stiffness for a load perpendicular to its kinematic path. For a load parallel to its kinematic path, the Watt's linkage has low stiffness, and thus is easily reconfigured. The Watt's linkage without torsional springs has no structural stiffness and collapses under gravity.

Fixing all of the rotational DOFs of the Watt's linkage results in an increase in stiffness in both the horizontal and vertical directions (Figure 4.19(A) and (B)). When all rotational DOFs are locked, the horizontal stiffness of the Watt's linkage depends on both the member cross-sectional area (A) and the moment of inertia (I) (Figure 4.19(C)). This is because when the structure is locked, the load results in axial and bending deformations. The vertical stiffness, however, only depends on the moment of inertia when the Watt's linkage is fully locked (Figure 4.19(D)). The structure experiences bending as a result of the vertical load and there is no axial dependence. These results show that when the rotational DOFs are locked, external loads are transferred to the members of the linkage, rather than being resisted by the added springs.

The number and combination of locked nodes will also affect the structural stiffness. In the horizontal direction, locking locations BC, ABC, and BCD all result in the same stiffness as locking at all locations (Figure 4.20). In the vertical direction, locking more nodes always leads to a higher stiffness, although the structure remains more flexible than in the horizontal direction.

The most effective combination of rotational DOFs to lock varies along the kinematic path. For all configurations, locking all rotational DOFs (at locations A, B, C, and D) leads to a system with the highest stiffness in the vertical direction. For horizontal stiffness, however, locking at location combinations BC, ABC, or BCD lead to the same stiffness as combination ABCD for all configurations (Figure 4.20).

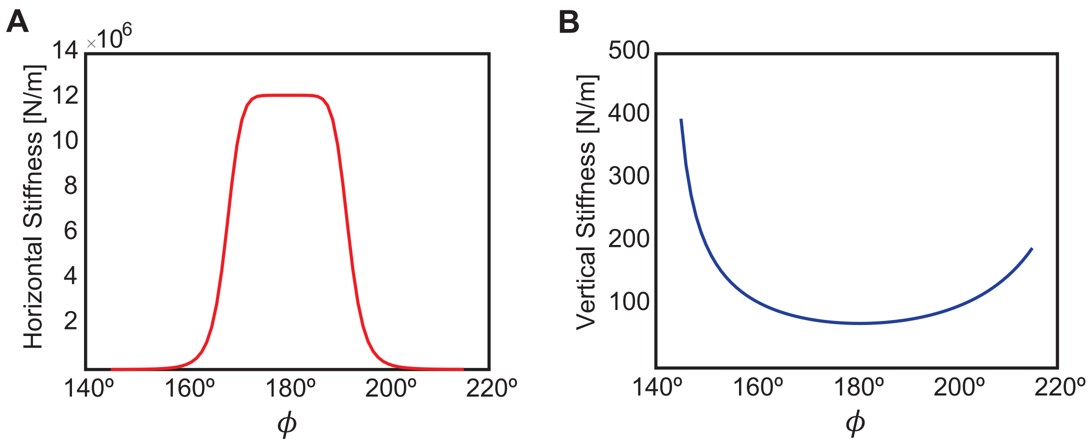

Figure 4.18: Structural stiffness of the Watt's linkage with optimized springs. (A) Stiffness of the Watt's linkage in the horizontal direction (perpendicular to the kinematic path). The linkage with springs has stiffness in the horizontal direction near the center of the kinematic path (at $\phi = 180°$), where the midpoint of the floating bar traces a straight line. Towards the ends of the kinematic path, the stiffness nears zero. (B) Stiffness in the vertical direction (parallel to the kinematic path) is several orders of magnitude lower than in the horizontal direction.

4.5 Concluding Remarks

Designing reconfigurable structures is a complex task, and one important aspect is to investigate the forces and displacements that develop as they reconfigure. In this chapter we used the traditional stiffness method to study the actuation of linkage systems, with a modified stiffness matrix that takes the effects of torsional springs into account. The results from this method confirm that the forces required for reconfiguration are reduced when optimized springs are added. For origami systems, we utilize the well-established bar and hinge model to compute the forces required for actuation and confirm that, even with optimized springs, the effects of bending and stretching are not significant.

We also explore physical prototype fabrication in this chapter. The design fabrication method is discussed and videos of the systems are provided in Appendix A. Preliminary tests of linkage and origami systems show that real reconfigurable structures can be designed to have continuous equilibrium and require lower actuation forces.

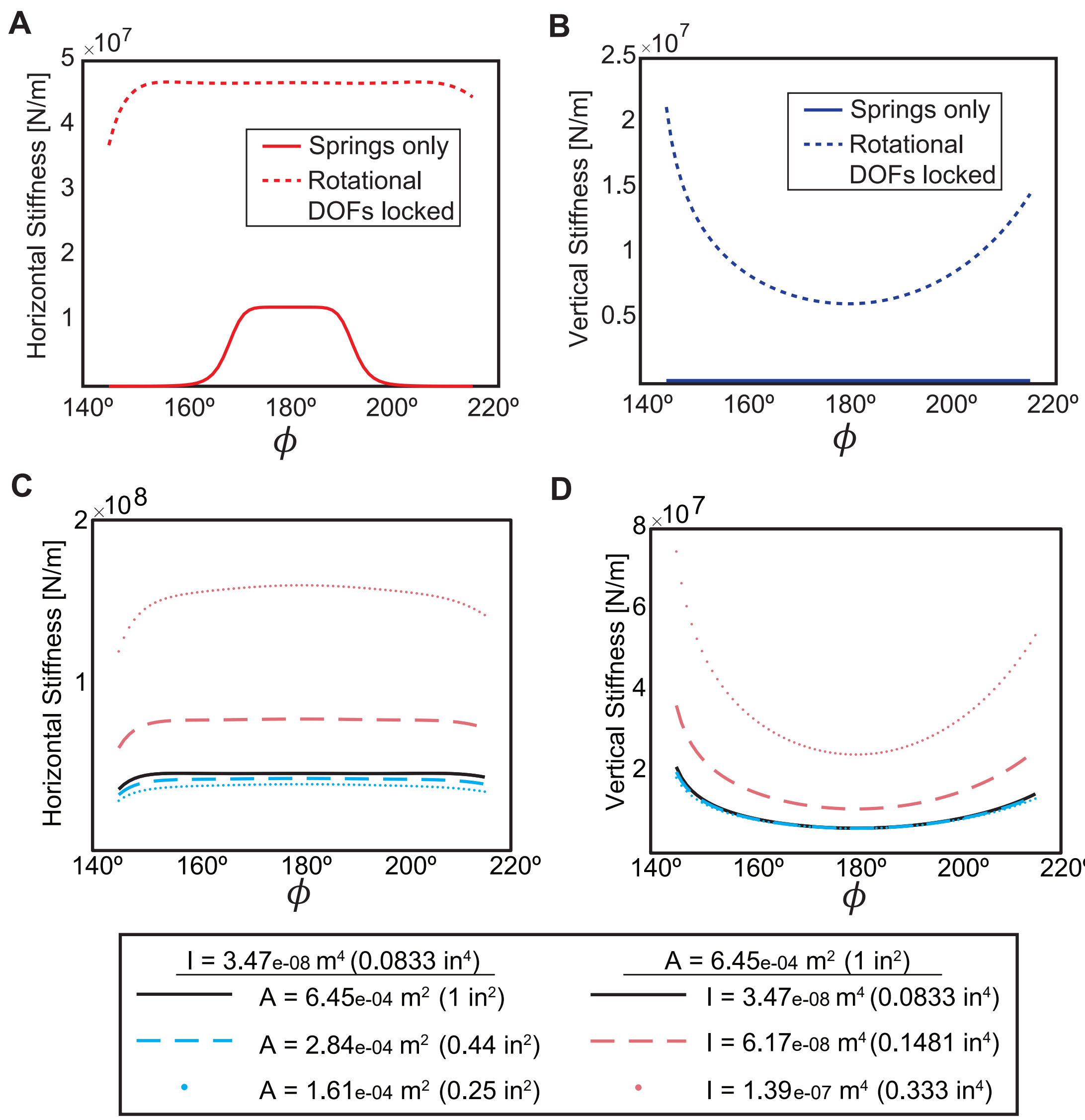

Figure 4.19: Structural stiffness of the Watt's linkage, with locking. (A) The stiffness of the Watt's linkage in the horizontal direction is increased when all rotational DOFs are locked. (B) In the vertical direction, locking increases the stiffness by several orders of magnitude. (C) The horizontal stiffness of the Watt's linkage depends on the member cross-sectional area (A) and the moment of inertia (I) when all rotational DOFs are locked. (D) The vertical stiffness of the Watt's linkage depends on the moment of inertia and does not depend on the cross-sectional area when all rotational DOFs are locked.

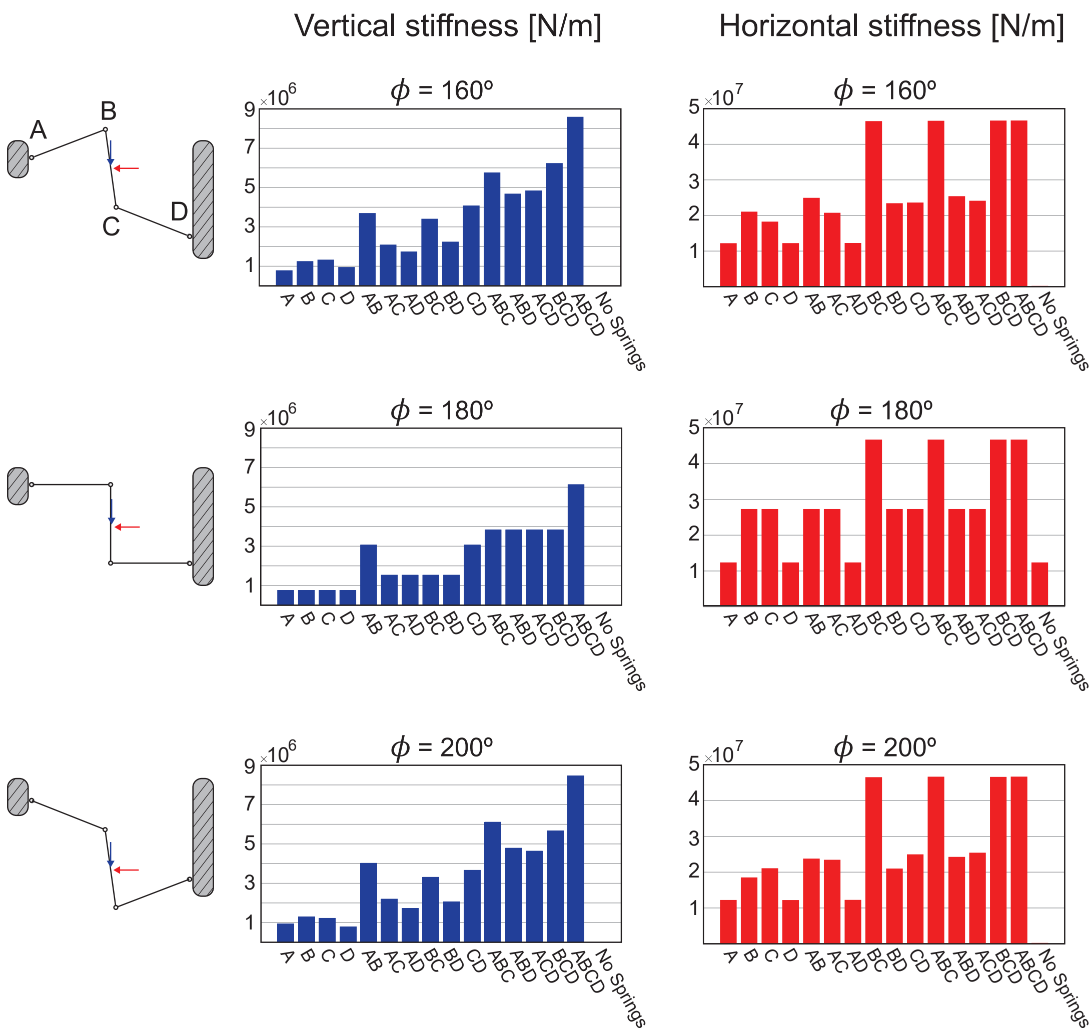

Figure 4.20: Stiffness of the Watt's linkage at $\psi = 0°$ for different locking combinations. The stiffness of the Watt's linkage can be increased by locking one or more rotational DOFs, at locations A, B, C, and D. The stiffness also changes as the structure reconfigures along its kinematic path. The highest vertical stiffness can be obtained by locking rotations at all locations (ABCD). The largest horizontal stiffness, however, can be achieved by locking location combinations BC, ABC, ACD, or ABCD.

CHAPTER 5

Pop-up Kirigami for Stiff, Dome-like Structures

This chapter presents a culminating example that addresses many of the challenges that arise when designing a reconfigurable structure for use at a civil engineering scale: it has high stiffness, can be fabricated using material with thickness, and has stable deployment when it is transformed into a system with continuous equiibrium. In architecture and engineering, curved surfaces such as arches and domes make excellent structural systems due to their high stiffness to weight ratio and efficiency in enclosing a volume. Domes made using material systems such as block masonry, poured concrete, and prestressed cables have been used for centuries as efficient roofs that can enclose large areas [102, 103, 104, 105]. Such surfaces can be used to focus, refract, or attenuate signals, making them useful in the design of antenna reflectors, solar thermal systems, and auditoriums [106, 107, 108, 109]. These curved shapes are difficult to create due to time-consuming or scale-limited processes. In recent years, origami and kirigami have risen as viable routes for the rapid fabrication of complex surfaces from flat sheets; however, these methods typically lead to systems that are overly flexible due to their high number of degrees of freedom.

This chapter presents a novel design for a pop-up kirigami system that achieves dome-like curvature and high stiffness by taking advantage of an internal infinitesimal mechanism. The system is fabricated from flat sheets using a hexagonal pattern, and the sheets remain flat locally as the system deforms into a doubly curved shape. The internal mechanism and deformation modes of the system are computed, revealing the flexible mode that creates dome-like curvature. Next, a parametric study based on changing the geometry of the system illustrates the possible shapes that result from changing the initial pattern. Finally, the high stiffness of the system in its final, dome-like shape is demonstrated. The proposed pop-up kirigami system offers a novel method for fabricating doubly curved surfaces with potential applications as deployable enclosures, concave reflectors, and more.

The work presented in this chapter is adapted from [46].

5.1 Introduction

It is a well-known phenomenon that adding curvature to a thin, flat sheet greatly increases its stiffness [110]. Any surface created from a flat sheet without stretching or tearing has zero Gaussian curvature; such surfaces are classified as developable [111]. It follows that introducing double curvature to a developable surface would be desirable; however, achieving positive Gaussian curvature from a flat sheet is difficult because it requires stretching, shrinking, crumpling, or tearing the sheet [112, 113]. Instead, doubly curved surfaces are typically fabricated using processes such as casting, molding, additive manufacturing, or assembly from individual pieces. These processes have several drawbacks: casting materials such as concrete is a slow process and often relies on extensive formwork; molding and additive manufacturing are limited by scale and material while also requiring internal support; and assembling a structure from individual pieces leads to complicated and expensive construction requirements.

Several origami methods have been explored to approximate curved surfaces, as reviewed by Callens and Zadpoor (2008). Periodic tesselations, such as the Miura-ori pattern, can be deformed out-of-plane into surfaces with nonzero Gaussian curvature if the flat facets of the sheet, or *panels*, are allowed to bend [87, 114]. Variations on the Miura-ori pattern have been designed to approximate complex curvatures while maintaining rigid folding characteristics, but the resulting structure remains flexible because of the possibility for bending [115]. Concentric pleating, as seen in the origami hypar, can also result in negative Gaussian curvature (saddle shape), but this technique also requires panels to bend and twist [116, 117]. Tachi's origami bunny [118, 119] uses a tucking technique to achieve highly complex surfaces with nonzero Gaussian curvature, but this method is only possible with extremely thin materials and quickly becomes untenable as systems are scaled up. Kirigami methods, which allow for cutting of material, have been explored as well. Curved kirigami surfaces often require a nonuniform tesselation pattern [120] and do not lead to a structurally robust system [121]. In summary, creating surfaces with curvature, especially double curvature, from a flat sheet is a unique challenge that often requires significant panel deformation, infinitesimally thin materials, or nonuniform cutting and folding patterns.

In this chapter, we present a novel pop-up kirigami system that deforms into a doubly curved surface while the panels remain nearly flat. The system begins as a kirigami structure with many flexible modes and stiffens as it deforms into a shape with positive Gaussian curvature. We show that the pop-up kirigami can accommodate thickness, lending it to future exploration as a system that can be built at a civil engineering scale. The structure's pattern is a repeating array of hexagons and trapezoids, beginning from two flat sheets that have been cut and fastened together. Its ability to achieve a doubly curved shape is due to an intrinsic infinitesimal mechanism that leads to *synclastic* (dome-forming) behavior.

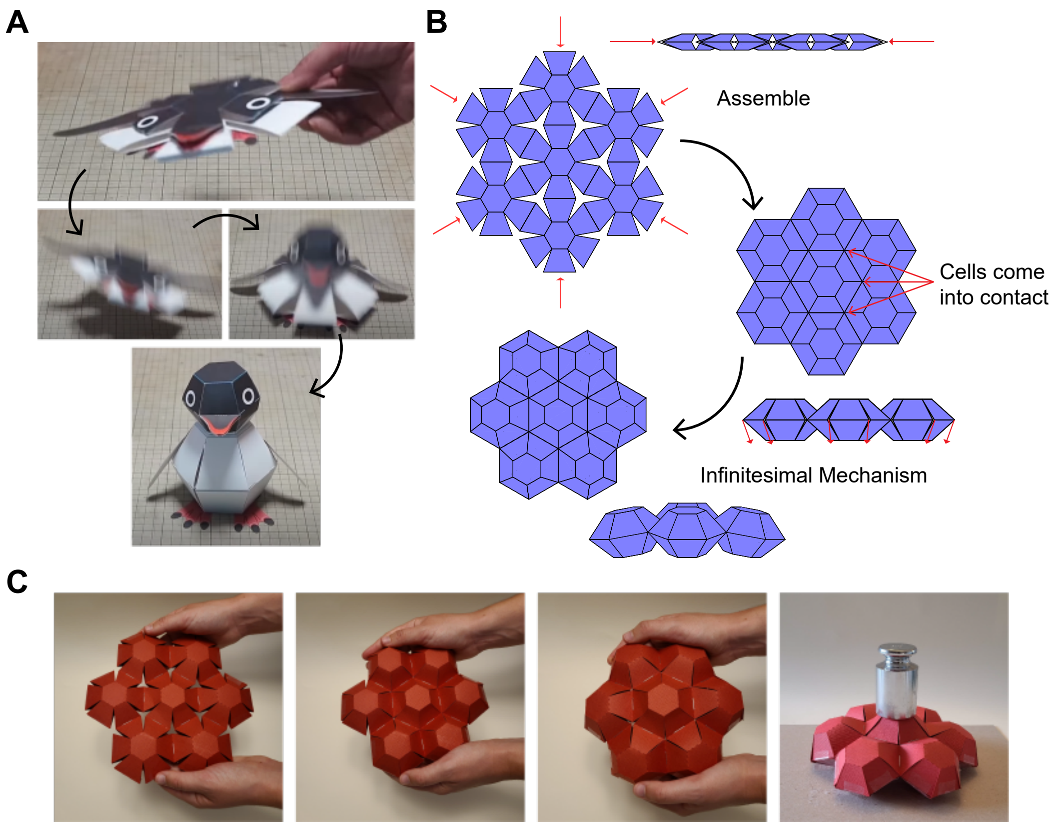

Figure 5.1: A novel pop-up kirigami structure that assembles and forms a dome-like shape. (A) The pop-up kirigami penguin by Haruki Nakamura inspired the structure presented in this chapter (Images used with permission of the artist). (B) Pop-up kirigami structure in flat state, assembling into 3D array, and deforming into a dome-like structure. (C) Paper prototype of pop-up structure, shown in flat, assembled, and curved states. The prototype has a mass of 17 grams and supports a 500 g load with no noticeable deformation.

This chapter introduces and explores the properties of the pop-up structures and is organized as follows: In Section 5.2, we define the system geometry, including how thickness can be incorporated for practical designs. The intrinsic properties of the system, including the infinitesimal mechanism that allows for the positive double curvature deformation, are discussed in Section 5.3. Next, we explore the possible geometric variations of the system and the effects of the pattern geometry on the resulting shape (Section 5.4). Finally, in Section 5.5 we demonstrate the stiffening properties of the resulting structure.

5.2 Geometric Definition

The inspiration for this novel system is a pop-up kirigami penguin toy made by Japanese artist Haruki Nakamura (Figure 5.1(A)) [122]. In his work, simple internal springs (usually made of rubber bands) are prestretched and locked when the toy is flat and are released when the toy is dropped, making the toy pop up into its 3D shape. We were intrigued by the structure of these toys because they begin as flat sheets and pop up into a 3D structure, a feature that is widely sought after in origami and kirigami engineering, especially for self-assembly at small scales [60, 123, 124]. The penguin body (which holds the internal spring mechanism) is a cell constructed from two sheets of paper cut into a central hexagonal panel and six surrounding trapezoidal panels, which are fastened together along their outer edges [125]. Our design is an array made up of these cells connected along those same outer edges, so that in places, four trapezoidal panels meet along one crease line. The result is a structure that can "pop up" into 3D as shown as the assembly step in Figure 5.1(B). In Section 5.6, we explore how this structure can be designed to have continuous equilibrium paths that aid with deployment.

5.2.1 Planar Geometric Definition

The base of the pop-up system presented in this chapter is a single cell made of two sheets cut into hexagonal and trapezoidal panels and connected along the bottom trapezoid edges. The pattern geometry of a cell is determined by the panel angle, γ and the panel length, L (Figure 5.2(A)). We assume the hexagon side length is always equal to 1 and scale all other units from this value. The possible range of the panel angle γ is $0 \leq \gamma < 30°$. The assembled (3D) shape of a single cell is defined by the folding angle between two trapezoidal panels, θ, along with the trapezoid dimensions γ and L. The range of θ depends on γ; a pattern with a larger γ has a smaller range of θ (Figure 5.2(B)). When $\gamma = 30°$, the pattern cannot assemble into a 3D shape and remains a flat sheet. We define the folding angle when the cell is closed as the closed angle θ_c. The closed angle can be computed from the panel angle as: $\theta_c = 2\cos^{-1}(\tan(\pi/3)\tan(\gamma))$.

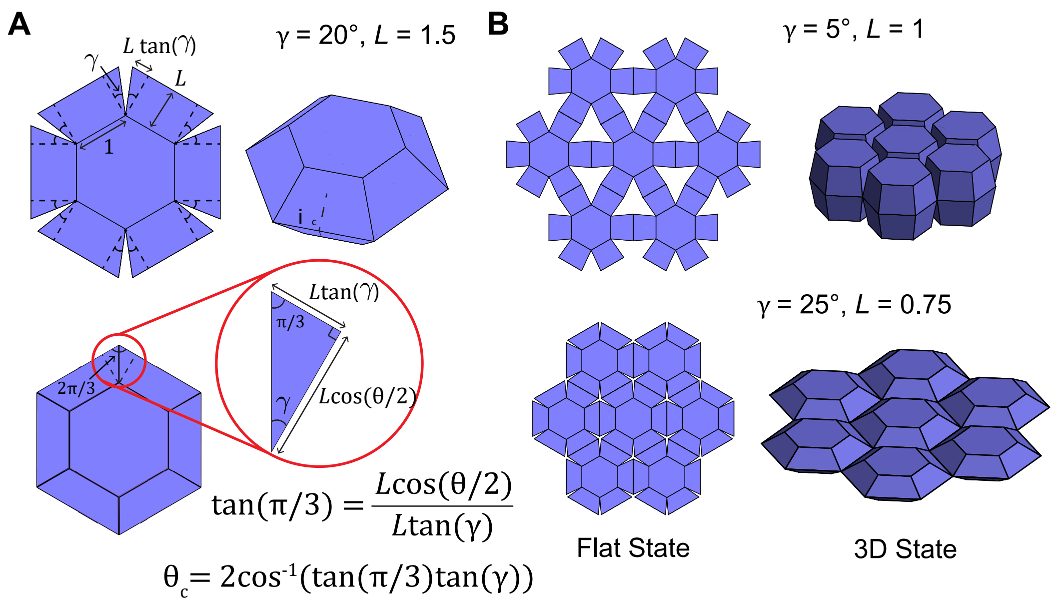

Figure 5.2: Geometric properties of the pop-up structure. (A) Geometry of a unit cell with $\gamma = 20^\circ$ and $L = 1.5$. The angle between two trapezoidal panels connected along their bottom edges is the folding angle θ, and when the cell becomes closed it is defined as θ_c. (B) Two examples of the seven cell structure with different geometries.

Individual cells are tessellated to create a larger cellular structure. The smallest of these structures has seven cells, and larger structures (with nineteen cells, thirty-seven cells, etc.) are made by adding cells radially outward from the center cell. In this and the following section, we primarily focus on the properties and behavior of a sample geometry of the seven-cell structure where $\gamma = 20^\circ$ and $L = 1.5$; in Section 4, we explore variations in γ, L, and the number of cells.

5.2.2 Modified Design of the Pop-up Kirigami Structure with Thickness

In this subsection, we introduce a modified design of the pop-up kirigami structure that can accommodate finite thickness. The design adds thickness on both sides of the initially flat planes of the panels. To allow for folding without restricting the kinematics, we implemented a hinge-shift technique, which moves the rotational hinges to the edges of the panels [48] (Figure 5.3(A)). The structure with thickness can fully assemble from flat into 3D with the addition of an angled cut along the bottom edge of each trapezoidal panel, as shown in Figure 5.3. The angle of the cut β depends on the panel angle as: $\beta = \tan^{-1}[\tan[\pi/2 - \cos^{-1}(\sqrt{3}\tan\gamma)]\cos\gamma]$. This modification with an angled cut applies for any thickness and any geometric definition of the cell. The angled cut allows for uninhibited rigid folding kinematics, where the adjacent cells come into contact only when the cell is fully closed.

We fabricated a prototype with thickness using foam board (Figure 5.3(C)). The geometric

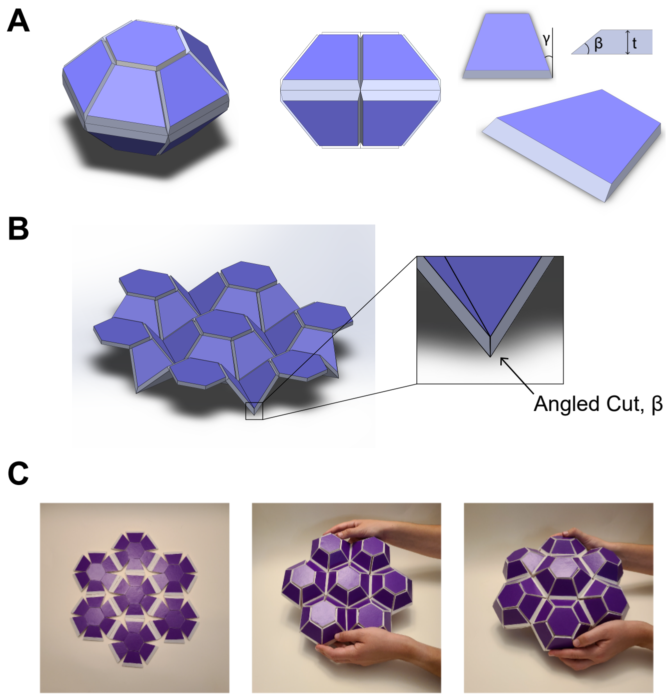

Figure 5.3: Modified design with thickness. (A) A 3D model of a single cell with the angled cut β shown on the trapezoidal panels. (B) A subset of the seven-cell system modeled with thickness. The angled cut β allows for the cells to fully assemble. (C) A prototype of the pop-up structure fabricated with foam board (thickness = 3/16”).

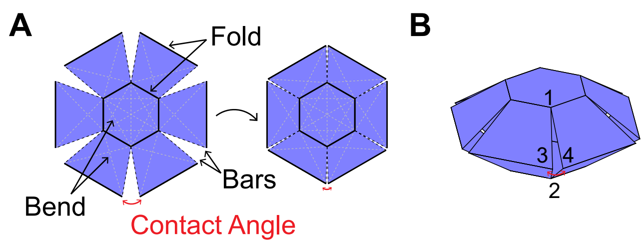

Figure 5.4: Bar and hinge model used to simulate the pop-up dome-like structure. (A) Bars are used to capture the in-plane stiffness of the trapezoidal and hexagonal panels. Bending hinges (shown in dashed gray lines) capture bending stiffness of the panels. Folding hinges (black lines) represent the folding stiffness of the crease lines. The additional bars included on the sides of the trapezoidal panels (dashed black lines) are the only ones that do not overlap with bending or folding hinges. (B) Contact angle used in bar and hinge simulations. As the distance between nodes 3 and 4 approaches zero, the contact energy and stiffness grow toward infinity.

parameters of the prototype are $\gamma = 20°$, hexagon side length $= 1$", $L = 1.5$", and thickness $t = 3/16$". The angled cut allows for the cells to fully assemble into the 3D shape, and the structure can deform into a dome-like shape, similar to the paper prototypes.

5.3 Intrinsic Properties of Pop-Up Kirigami System

In this section, we used the bar and hinge method to simulate the pop-up system and explore several interesting intrinsic properties. We first investigated the internal mechanism of the seven-cell structure (Section 5.3.2). Next, we utilized the bar and hinge method to simulate the system assembling from flat to 3D and deforming into a doubly curved shape (Section 5.3.3). Finally, we conducted an eigenvalue analysis to confirm the existence of an infinitesimal mechanism and explore other modes of deformation (Section 5.3.4).

5.3.1 Bar and Hinge Model for Pop-Up System

We use the bar and hinge model to simulate the structure as it assembles from a flat state and deforms into a dome-like shape. The bar and hinge model used in this chapter is based on the MERLIN 2 origami modeling package because it can perform large-displacement, highly nonlinear analyses [101]. We model bars using a material with Young's modulus $E = 10^8$, thickness $t = 0.01$, and Poisson ratio $\nu = 1/3$. We use these arbitrary units of realistic relative magnitudes to demonstrate the fundamental characteristics of the pop-up structures. The panel bending stiffness K_B depends on the material parameters E, t, ν and the panel geometry, as follows:

$$K_B = \big(0.55 - 0.42\frac{\Sigma\alpha}{\pi}\big)\frac{Et^3}{12(1-\nu^2)}\big(\frac{D_S}{t}\big)^{1/3}, \tag{5.1}$$

where $\Sigma\alpha$ is the sum of the internal angles of the panels and D_S is the length of the shortest diagonal bar [100]. We use average values of $\Sigma\alpha = 0.9\pi$ and $D_S = \sqrt{2}$ for all panels.

The stiffness of the fold lines K_F is defined as $K_B/1000$ in order to simulate a structure with panels that are stiff and folds that provide near zero contribution to the rigidity of the structure. The axial (stretching) bar stiffness K_S is EA/L, where A is the bar cross-sectional area and L is the bar length. Formulations of bar cross-sectional areas for quadrilateral panels, including skewed (parallelogram) panels, have been established in the literature [100], and a general approximation for polygonal panels has also been proposed [101]. Our novel system includes hexagonal and trapezoidal panels, which require new bar area definitions for accurate modeling of their in-plane stiffness. We derive appropriate bar areas and present them in Sections 5.3.1.1 and 5.3.1.2 for hexagonal and trapezoidal panels, respectively.

An important and challenging aspect of origami modeling is capturing when panels come into contact [126]. To avoid panel intersections, we implement a simplified contact model using a penalty function applied to a rotational spring [99]. Contact rotational springs were defined between adjacent trapezoidal panels (Figure 5.4(A)). Six of these springs were defined per cell, with axes spanning between the top and bottom sheets. The hinges connect nodes 1, 2, 3, and 4 shown in Figure 5.4(B) to measure the contact angle, such that as nodes 3 and 4 approach each other, contact is engaged. The initial stiffness of the contact hinge is $K_C = 20 * K_F$ and the stiffness increases toward infinity as the distance between nodes 3 and 4 approaches zero. This increase in stiffness avoids panel intersection and simulates the effect of the panels coming into contact.

5.3.1.1 Bar Area Formulations for Hexagonal Panels

The hexagonal panels are modeled using the bar and hinge method with 15 bars, shown in Figure A.1. Six bars connect the nodes along the perimeter of the panels and have bar cross-sectional area A_{ext}. Three bars with area A_{int1} connect the major diagonals of the hexagon, and six bars with area A_{int2} connect the shorter diagonals of the hexagon.

The bar areas were chosen such that the stretching and shearing behavior of the hexagonal panel matches the behavior of a block of material with length and width s, the side length of the hexagonal panel. The theoretical stretching stiffness of the block of material is $K = EA/L = Est/s = Et$. The theoretical shear stiffness is $K_{sh} = Gst/s = Gt$, where $G = E/(2(1+\nu))$. We assume the following material properties: Young's modulus $E = 10^8$, thickness $t = 0.01$, and Poisson's ratio $\nu = 1/3$.

We found the stretching and shearing behavior of the hexagonal panel by assembling a stiff-

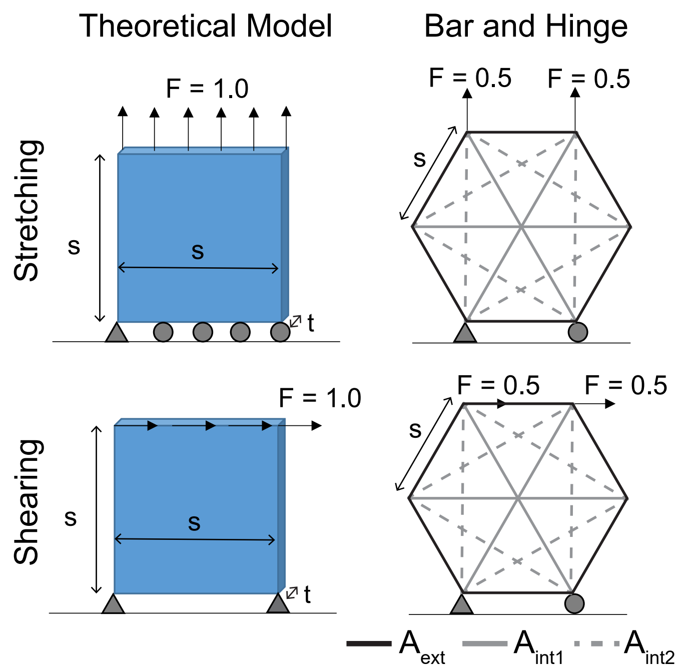

Figure 5.5: Bar area formulation for hexagonal panels. The stretching and shearing stiffness of the hexagonal panels was defined to match the stiffness of a square block of material with comparable dimensions.

ness matrix, applying a force of 0.5 on the top two nodes (vertical for stretching, horizontal for shearing), and solving for the nodal displacements Δ. The stiffness of the bar and hinge panel is then calculated as $K_{B\&H} = 1.0/\Delta$. Conducting this process where we systematically varied the bar areas, we found that the following definitions led to stretching and shearing behaviors that matched the theoretical solutions:

$$A_{ext} = 0.13 * t * s \tag{5.2}$$

$$A_{int1} = 0.13 * 0.5 * t * s \tag{5.3}$$

$$A_{int2} = 0.13 * 60 * t * s \tag{5.4}$$

These definitions allow the bar areas to be scaled with the side length of the hexagonal panel and panel thickness.

5.3.1.2 Bar Area Formulations for Trapezoidal Panels

Trapezoidal panels were modeled using the bar and hinge method with 6 bars. Four of the bars connect the nodes around the panel perimeter and two diagonal bars connect opposite corner nodes.

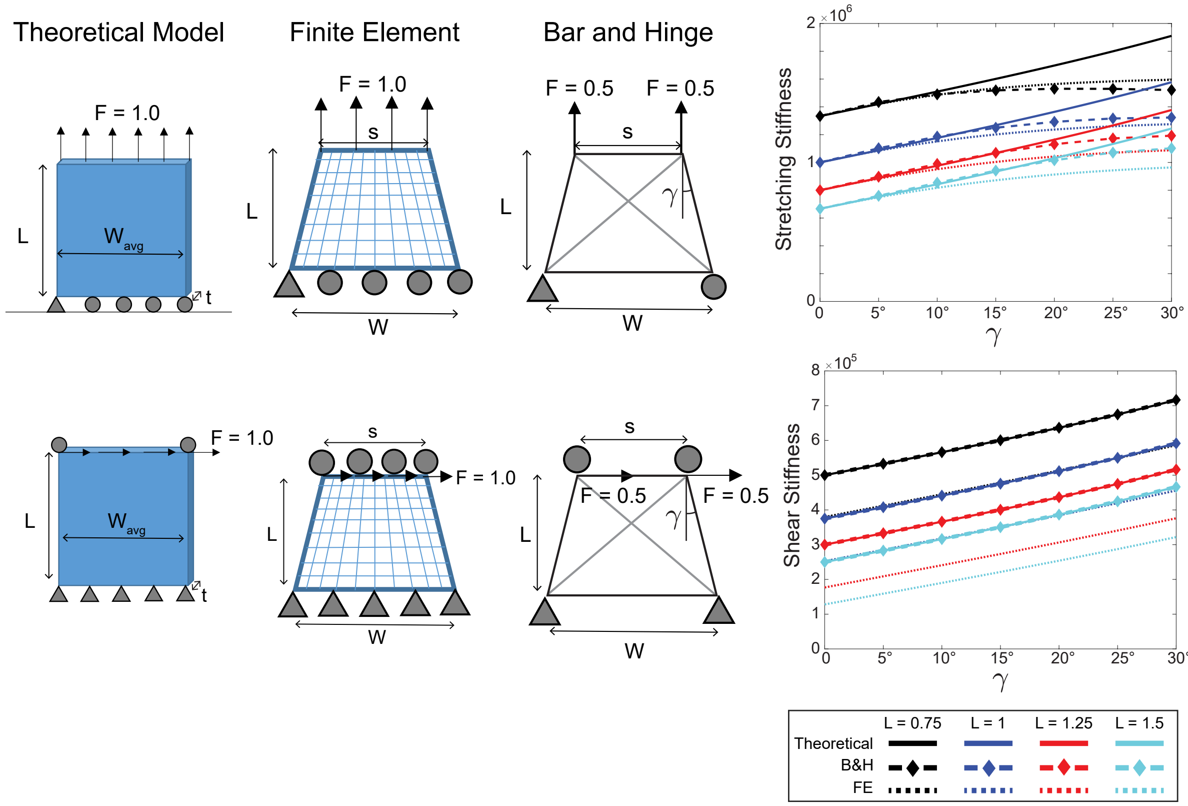

Figure 5.6: Bar area formulation for trapezoidal panels. The stretching and shearing stiffness of the trapezoidal panels was defined to match the stiffness of a rectangular block of material with the same total area. The plots on the right show the performance of different models for different panel angles γ.

We calculated cross-sectional areas for the bars that match the stretching and shearing behavior of the panel to the theoretical stretching and shearing of a block of material. As an additional check, we also compared the bar and hinge model results to a discretized finite element model using S4 elements. The following material properties were used for all 3 models: Young's modulus $E = 10^8$, thickness $t = 0.01$, and Poisson's ratio $\nu = 1/3$.

We started with a block of material with a height of L, thickness t, and width $W_{avg} = (W+s)/2$, where L is the length of the trapezoidal panel and W is its bottom width. We applied an upward force $F_y = 1.0$ on the top surface of the block. The resulting vertical displacement Δ_y can be calculated using stress-strain relationships:

$$\sigma_y = \frac{F_y}{W_{avg}t} \qquad \epsilon_y = \frac{\sigma_y}{E} = \frac{F_y}{EW_{avg}t} \qquad \Delta_y = \epsilon_y L = \frac{F_y L}{EW_{avg}t}$$

The horizontal displacement Δ_x and strain ϵ_x are found using the Possion's ratio, ν:

$$\Delta_x = -\nu \Delta_y \frac{W_{avg}}{L} \qquad\qquad \epsilon_x = \frac{\Delta_x}{W_{avg}}$$

We applied these displacements and strains to the bars of the trapezoidal panel and found the change in length Δ of each bar. Next we found the forces in each bar: $F = K\Delta = EA\Delta/L$, with the bar cross-sectional area A still unknown. From this stretching case, we obtained two independent equilibrium equations by summing the forces in the x- and y-directions at the nodes.

Using a similar process to the stretching case, we also applied a horizontal shear force to the top surface of the block of material, calculated the displacements and strains, applied them to the bars and nodes, and solved for the bar forces. The shearing case led to one additional independent equilibrium equation after summing the forces at the nodes. We obtain the fourth independent equation needed to solve for the 4 bar areas by assuming that the top and bottom bar areas are equal.

Solving the 4 equations gives expressions for the bar cross-sectional areas in terms of geometric dimensions of the trapezoid (W, L, s, t) and material parameters (E, ν). The expressions for the bar areas are lengthy; we encourage interested readers to contact the authors for the full formulations. We performed a patch test to compare the behavior of the bar and hinge trapezoidal panel with the theoretical solution and a discretized FE model. The results (shown in Figure A1) show that the bar and hinge model with the calculated areas matches the behavior of the theoretical and FE models well. The bar and hinge model follows the same trends as the FE results, and only slightly overestimates the shear stiffness. The bar and hinge model cannot capture the local deformations that make the realistic shear case more flexible.

5.3.2 Mechanism Analysis

Through informal experimentation with paper models of the pop-up structure, we observed that the system has the ability to deform into a shape with dome-like curvature (Figure 5.1(C)). While initially flexible, the models begin to stiffen as the curvature develops. Using the bar and hinge method along with several resources on the analysis of internal mechanisms, we verified that this stiffening does occur and is the result of a single infinitesimal mechanism.

Pin-jointed assemblages (such as a structure modeled using bars and hinges) can be described mechanically in terms of the number of inextensional mechanisms (m) and states of self-stress (s) that are possible for the structure [4]. A mechanism is defined as a displacement that does not cause internal forces to develop in the structure (excluding rigid body motions of the full system in space). A state of self-stress is a condition where nonzero internal forces in a structure can exist in equilibrium without the application of external forces. The quantities m and s are also referred to as the degrees of kinematic (m) and static (s) indeterminacy [127, 128, 129]. In certain cases, activating a structure's state of self-stress leads to a stiffening effect in one or more of its mechanisms. These cases are known as *infinitesimal mechanisms,* in contrast to finite mechanisms, which allow for large nodal displacements with no stiffening [3].

The equilibrium and kinematic equations of a pin-jointed structure involve the following quantities: the internal bar forces **t**, the external loads applied at the joints **f**, the joint displacements **d**, and the bar elongations **e**. These quantities are related to each other by the equilibrium matrix **A**:

$$\mathbf{At} = \mathbf{f},$$

and its transpose, the compatibility matrix $\mathbf{B} = \mathbf{A^T}$:

$$\mathbf{Bd} = \mathbf{e}.$$

The quantities m and s are related to the number of bars (b), non-support joints (j), and support reactions (k) in a structure through an extension of Maxwell's rule, which is typically used to determine a structure's degree of static indeterminancy: $s - m = b - 3j + k$ [3]. However, the exact values of m and s for a given structure cannot be found simply by counting the bars and joints. They require computing the four vector subspaces of the structure's equilibrium matrix: the null space, left null space, column space, and row space. The null space of the equilibrium matrix contains the structure's independent states of self-stress (and therefore s), and the left null space gives the mechanism displacements **D** (and therefore the number of mechanisms m). The column space identifies the non-redundant bars of a structure, essentially describing the statically determinate structure that would result if the redundant bars were removed. The row space gives the set of geometrically compatible bar elongations.

Pellegrino and Calladine developed an algorithm that evaluates whether a pin-jointed structure's internal mechanisms are infinitesimal or finite [3, 4]. The algorithm involves constructing a modified equilibrium matrix **A'** comprised of the structure's original equilibrium matrix and the product force vectors ($\mathbf{A'} = [\mathbf{A}|\mathbf{P}]$) and evaluating whether the new matrix is full rank. The product force vectors **P** give the loads that occur at the joints as the structure moves into a mechanism displacement and is no longer in equilibrium under zero external load. An additional check for positive definiteness verifies the stability of the infinitesimal mechanism.

Following the algorithm approach, we discovered that the seven-cell pop-up kirigami structure has one infinitesimal mechanism. Using the bar and hinge model, we obtained the structure's equilibrium matrix and its four vector subspaces. The left null space contains one set of mechanism displacements, thus giving a value of $m = 1$. When the mechanism displacements **D** are applied

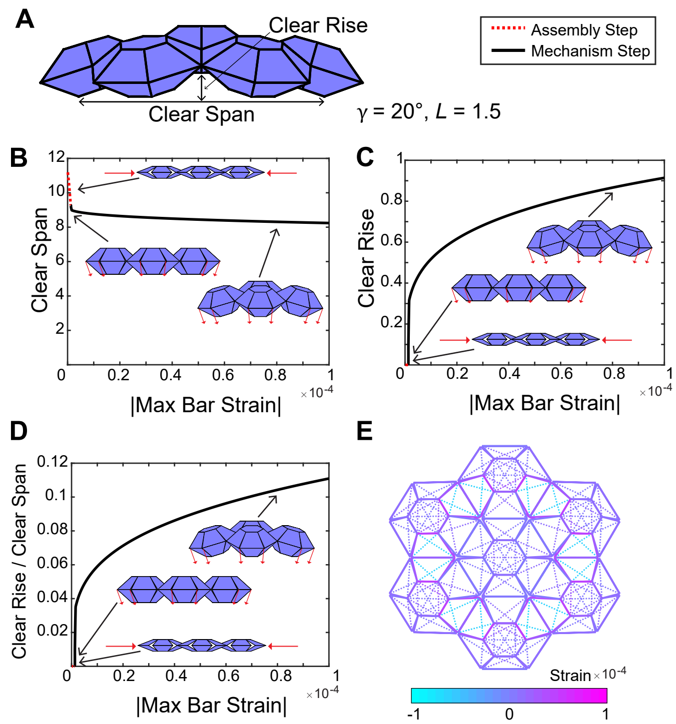

Figure 5.7: Analysis of the pop-up structure using the bar and hinge model. (A) We use two metrics to quantify the change in geometry of the system during the two-step analysis: clear rise and clear span. We define the clear rise as the vertical distance from the bottom nodes of the outer cells to the bottom nodes of the center cell, and the clear span as the horizontal distance between bottom nodes of opposite outer cells. (B)-(C) As bar strains increase during the analysis, the clear span decreases and the clear rise increases. (D) The ratio of clear rise to clear span is used to describe the increasing curvature of the structure during the analysis. (E) Distribution of bar strains at the end of the two-step analysis.

to the structure, the resulting shape resembles a dome, as we expected and as shown in Figure 5.1. We then followed the procedure outlined in the literature to compute the product force vectors and assemble the modified equilibrium matrix **A'**, we verified that it is full rank, and performed the stability check. The seven-cell structure has 432 degrees of freedom and 18 of them are restrained at the bottom center hexagonal panel. The structure has 714 bars, and the equilibrium matrix **A** has dimensions (714 x 432). The modified equilibrium matrix **A'** has dimensions (414 x 413), and there are 301 possible independent states of self-stress ($s = 301$). These quantities, along with $m = 1$ for the structure, satisfy the extension of Maxwell's rule. The result of the algorithm confirms that the mechanism is infinitesimal, indicating that as the structure develops positive double curvature, the assemblage stiffens.

5.3.3 Achieving Double Curvature

The mechanism analysis presented in Section 5.3.2 reveals that the pop-up system has the ability to achieve positive double curvature, thanks to an internal infinitesimal mechanism. In this section, we study the system as it follows the infinitesimal mechanism and deforms into a doubly curved shape. We used the bar and hinge method described in Section 5.3.1 to perform a two-step, displacement controlled analysis to simulate the structure as it assembles from flat and subsequently deforms. The first step (assembly) runs until the contact angle between the trapezoidal panels is sufficiently small ($< 3°$). This angle limit ensures that the spaces between cells are nearly closed and that adjacent trapezoidal panels are engaging the contact hinges. The second step (mechanism) deforms the structure into a doubly curved shape using a follower displacement applied at the 12 nodes along the outer perimeter of the structure and runs until the maximum bar strain (regardless of whether in tension or compression) exceeds 0.01%. This threshold was chosen to emulate realistic strain values that structural materials can experience without failure. The structure has the ability to curve more if higher strains are allowed.

Figure 5.7 illustrates the two-step analysis for the pop-up structure. We use two metrics to quantify how the geometry of the structure changes during the analysis (shown in Figure 5.7(A)): the *clear rise*, defined as the vertical distance from the bottom nodes of the outer cells to the bottom nodes of the center cell, and the *clear span*, the horizontal distance between bottom nodes of opposite outer cells. During the assembly step, the clear rise remains zero and the clear span shortens as the structure comes together into its 3D shape. Bar strains remain near zero during this step. During the mechanism step, the system takes on the curved shape of the infinitesimal mechanism discussed in Section 5.3.2. As the bar strains increase, the clear span decreases and the clear rise increases. A more descriptive parameter that we use to understand the curvature of the structure is the ratio of clear rise to clear span. The ratio increases during the mechanism step as the structure becomes more curved.

For the seven-cell system with $\gamma = 20°$ and $L = 1.5$, the clear span shortens from 11 to 8 during the two-step analysis. During the mechanism step, the clear rise grows to 0.9, resulting in a final clear rise to clear span ratio of 0.11. As the clear rise increases and the clear span decreases during the deformation, the structure begins to take the shape of a spherical cap. A practical limit to the clear rise to clear span ratio is 0.5, corresponding to a hemisphere.

The mechanism displacements can occur without significant panel bending, as can be shown using the two-step analysis. During the analysis, the bending angles of all panels remain less than $3°$ while the majority of the bending angles remain below $1°$ (Figure 5.8). These small bending angles confirm that the panels remain nearly flat, especially when the infinitesimal mechanism is first applied. As the analysis progresses, small stretching and bending energies develop in the

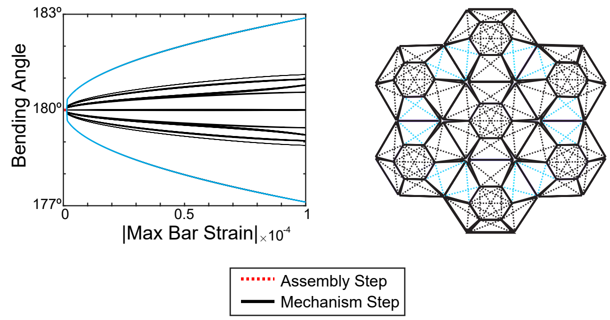

Figure 5.8: Small bending angles develop in the structure during the two-step analysis. Most of the angles are less than $1°$. Some panels experience bending angles up to $\approx 3°$ (highlighted in blue).

panels and lead to the observed stiffening effect.

5.3.4 Eigenvalue Analysis

In addition to the mechanism analysis, we investigated the eigenvalues and eigenmodes of the pop-up structure. The eigenmodes provide information on the structure's infinitesimal mechanism, deformation characteristics, and self-stiffening property. The eigenvalues and modes are found using the equation $\mathbf{K}\phi_i = \lambda_i\phi_i$, where $\mathbf{K}$ is the structure's full stiffness matrix, ϕ_i is the i^{th} eigenmode vector, and λ_i is the i^{th} eigenvalue. The magnitude of an eigenvalue λ scales directly with the energy required to deform a structure into the shape described by the corresponding eigenmode. A higher eigenvalue indicates a stiffer (more energetically expensive) deformation. An eigenvalue of zero indicates a deformation that does not produce any internal forces in a structure – either a rigid body motion or an internal mechanism.

The eigenvalues and eigenmodes of the pop-up structure in various configurations are shown in Figure 5.9. In addition to the flat structure, we conducted the eigenvalue analysis for the assembled structure (Figure 5.9(B)) and curved structure (Figure 5.9(D)). These geometries were found using the two-step analysis described in Section 5.3.3. We also explored how the eigenvalues of these configurations change when the nodes of adjacent cells are connected (Figure 5.9(C) and (E)). For the connected cases, the nodes that come into contact during assembly are connected by bars with high stiffness. The connected design represents a practical scenario where the individual cells of the structure are connected after assembly. This scenario accounts for the increased stiffness due to contact which can be captured by the large displacement analyses (Figure 5.7), but is not captured in the infinitesimal eigenvalue simulations without connections.

The first six eigenvalues of the flat (unassembled) structure are zero, and they represent the six

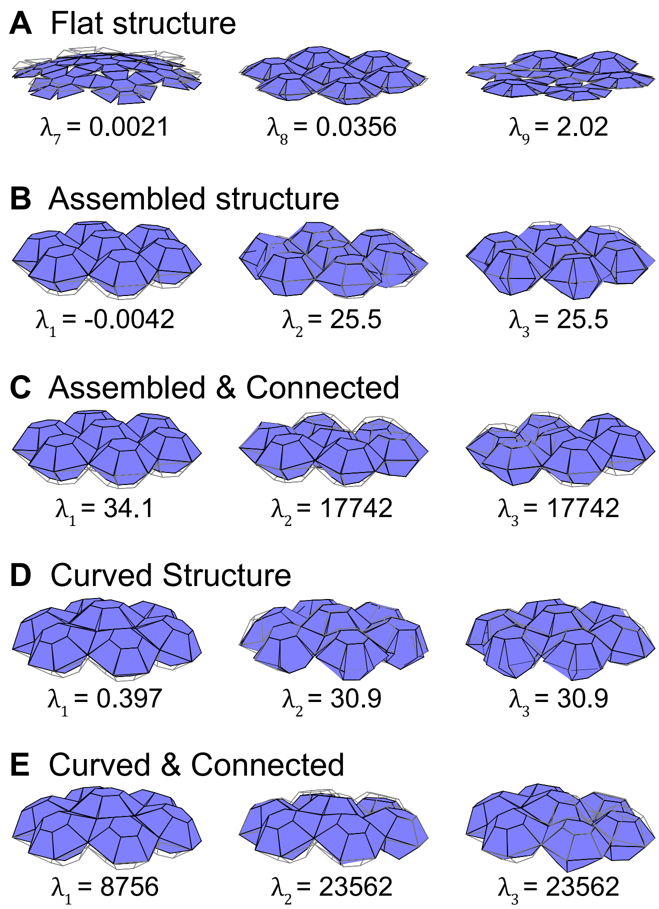

Figure 5.9: Eigenvalues and eigenmodes of the pop-up structure. (A) Modes of the flat, unassembled structure. Eigenvalues $\lambda_1 - \lambda_6$ of this configuration are the rigid body motions in space. The next eigenvalue λ_7 is ≈ 0, indicating that it is an internal mechanism. (B) Modes of the assembled structure with the outer perimeter constrained. The eigenvalue corresponding to the infinitesimal mechanism λ_1 remains near zero. (C) Connection bars are added to the nodes which come into contact for the assembled structure, increasing the eigenvalues. The first eigenvalue λ_1 remains small compared to λ_2 and λ_3. (D) Modes of the structure after it is deformed into a dome-like shape. The first eigenvalue λ_1 is again near zero, reflecting the infinitesimal mechanism, and the other modes remain relatively flexible. (E) Modes of the curved structure with connections. All eigenvalues are high, indicating a stiff structure.

rigid body motions in space. The next eigenvalue (λ_7) is very close to zero, meaning it is an internal mechanism. The 7th eigenmode of the flat structure is the doubly curved shape, as we found in the mechanism analysis (Section 5.3.2). The 8th eigenmode is the assembly motion, where the structure "pops up" from flat to 3D. The 9th eigenvalue is representative of the energy of a higher mode, where some cells are squeezed.

For all configurations other than flat, additional boundary constraints were included to restrict the structure's rigid body motions in space; thus, in Figure 5.9(B) - (E) the eigenvalues begin at λ_1. For these configurations, the first eigenvalue λ_1 is significantly lower than λ_2 and λ_3. The jump between eigenvalues indicates a large increase in stiffness between the modes; the first eigenmode (which resembles the dome-like shape) is significantly more flexible than other modes. The first eigenvalues λ_7 and λ_1 in parts (A)-(D) of Figure 5.9 represent the infinitesimal mechanism and are much lower than the subsequent eigenvalues. These eigenmodes require only folding along the crease lines and minor bending in the panels. In contrast, some of the eigenvalues for the connected structures are several orders of magnitude higher because they require stretching and shearing of the sheet. By itself, deforming the structure into the curved shape only results in a modest increase in eigenvalues because the infinitesimal eigenmodes can still exhibit self-intersection and local squeezing deformations (λ_2 and λ_3 of Figure 5.9(D)). When we place a perimeter boundary and internal connections (representing adjacent panels in contact) in the structure, all eigenmodes are significantly stiffened as shown in Figure 5.9(E). These eigenvalue simulations show that the flexible infinitesimal mechanism can be used to assemble the kirigami into the dome-like shape which can then be stiffened by internal contacts and perimeter constraints.

5.4 Geometric Properties from Parameter Variations

We use several metrics in addition to the clear rise and clear span defined in Section 5.3.3 to compare the final deformed shapes of the kirigami structures with different parameters (illustrated in Figure 5.10(A)). The *clear volume* is the volume underneath the structure, calculated using the volume of a spherical cap ($V = 1/6\pi h(3a^2 + h^2)$) where the height *h* is equal to the clear rise and the base radius *a* is equal to half of the clear span. The *enclosed volume* is the volume within all cells of the structure, and the *% clear volume* is the ratio of the clear volume to the total volume (clear plus enclosed). We compared these metrics as we varied γ, L, and the number of cells.

5.4.1 Changing Panel Angle and Panel Length

The two-step analysis described in Section 5.3.3 was conducted for structures with various panel angles (γ = 10°-25°) and panel lengths ($L = 0.75, 1, 1.25, 1.5$). Shown in Figure 5.10, these parameters drastically influence the final appearance and geometric properties of the final shape. We found that the clear rise depends on the panel length L, with larger L resulting in a larger clear rise. As γ increases, the clear rise stays fairly constant for a given L, with a small decrease as γ approaches 25° (Figure 5.10(B)). The clear span increases with both γ and L (Figure 5.10(C)). This increase in clear span is somewhat intuitive, because we increase the overall pattern size by increasing L and make a shallower assembled structure by increasing γ. The clear rise to clear span ratio of all geometries ranges between 0.07 and 0.14 (Figure 5.10(D)). Many classical domes used in architecture have a clear rise to clear span ratio near to 0.5. One way to increase the clear rise to clear span ratio of the proposed kirigami structures is to add more cells, as discussed in Section 5.4.2.

Geometries with larger γ and L result in structures with larger clear volume, and for larger panel lengths an increase in γ leads to a more dramatic increase in clear volume (Figure 5.10(E)). Interestingly, the relationship between $\%$ clear volume and L is flipped; a larger L gives a *smaller* % clear volume. This relationship indicates that we can construct a structure with a higher fraction of usable space to total occupied volume (larger % clear volume) using less material (smaller L).

5.4.2 Adding Cells

In addition to the seven-cell system, we also studied a larger system with 19 cells. The nineteen-cell structure assembles and deforms into a doubly curved surface in the same manner as the seven-cell version, as demonstrated by the bar and hinge simulations and physical prototypes (Figure 5.11(A)). We were interested in whether adding cells would result in a more curved structure, and we use the clear rise to clear span ratio as a measurement of curvature for comparison. Figure 5.11(B) shows that for a structure with $\gamma = 20^\circ$ and $L = 1.5$, when deformed to reach the same bar strains, the nineteen-cell system reaches a higher clear rise to clear span ratio: 0.15 up from 0.11. This increase is a good indication that by continuing to add cells, our design could reach the curvature levels of typical domes found in architecture and structural engineering. Additionally, this structure has a clear volume of 214 in comparison to the clear volume of 24 for the seven-cell structure with the same geometric parameters. This is about a nine (8.9) times increase in usable clear volume for only about a three (2.7) times increase in the total material used to construct the structure.

5.5 Dome Stiffness

To investigate the stiffness of the pop-up kirigami structure, we constrained the structure along the outer perimeter in the *x*-, *y*-, and *z*-directions and applied small vertical displacements ($\Delta = -0.1$)

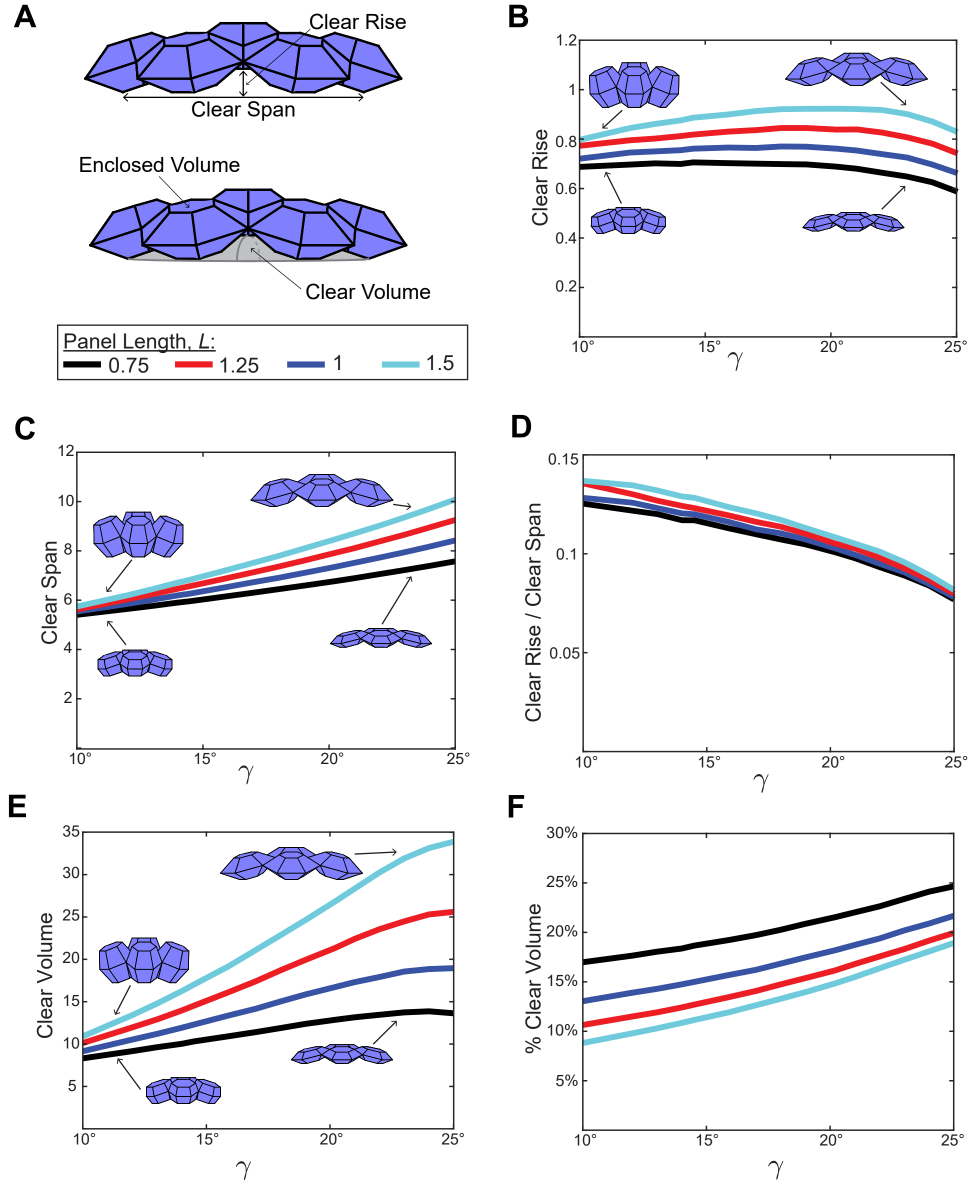

Figure 5.10: Parametric study of the pop-up kirigami structure. (A) Geometric properties measured for the curved pop-up kirigami structures: clear rise, clear span, clear volume, and enclosed volume. (B) Larger panel lengths result in systems with larger clear rise. Clear rise is less influenced by the panel angle γ. (C) Larger clear spans result from systems with larger L and γ. (D) The ratio of clear rise to clear span decreases as γ increases, and is mostly independent of L. (E) Larger L and γ result in structures with larger clear volumes. (F) Interestingly, structures with smaller L results in higher % clear volumes.

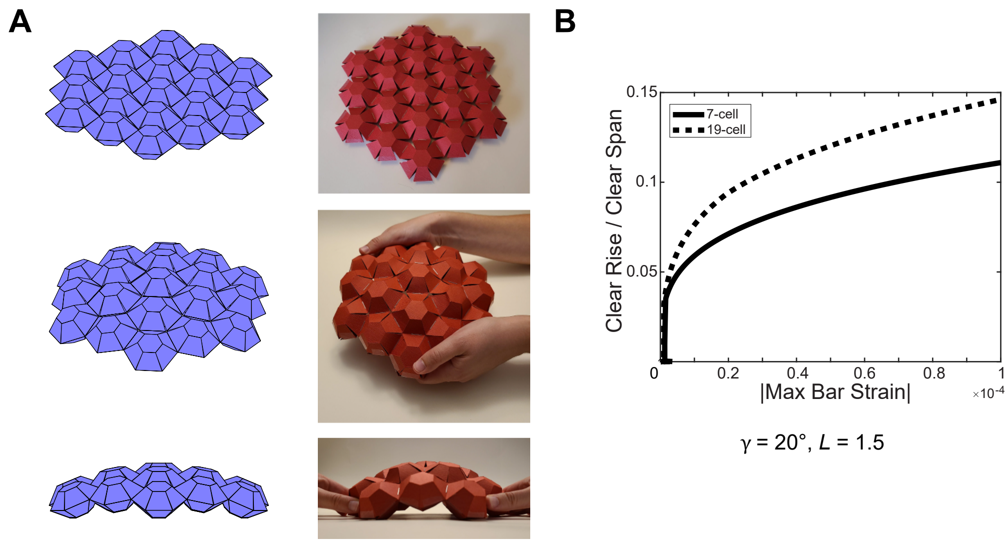

Figure 5.11: Adding cells to create a larger pop-up structure. (A) A nineteen-cell variant of the pop-up system, modeled with the bar and hinge method and as a paper prototype. (B) The clear rise to clear span ratio of the nineteen-cell system is larger than that of the seven-cell system with the same geometry when curved to reach the same magnitude of bar strains.

at the interior points where the cells meet (Figure 5.12(A)). The bar and hinge method was used to apply the displacement in 10 steps and calculate the resulting vertical forces (F) at the supports. The force-displacement relationship was linear in this range of deformation. A stiffness value representing the full structure was found using the relationship $K = \Sigma F/\Delta$.

Overall, we found that the stiffness of the curved structures mostly depends on γ, and the stiffness varies less significantly with L (Figure 5.12(C)). To better understand the characteristics of the pop-up kirigami, we compare its stiffness with a curved sheet restrained on two edges with clear rise and clear span values averaged from the results in Section 4 and twice the material thickness of the kirigami panels (to account for the two sheets used in the pop-up structures). An analytical approximation for the stiffness of the curved sheet is found using Castigliano's theorem and provides a base point comparison for the stiffness values, as discussed in Section 5.5.1.

The comparison shows that our structures, with any γ or L, are as stiff as a curved sheet made of material with 10 to 17.5 times the total pop-up kirigami thickness ($t_c = 10*2*t$ to $t_c = 17.5*2*t$). Because the bending rigidity of the sheet scales with t_c^3, the pop-up kirigami is in fact $\approx$ 1,000 to 5,000 times stiffer than a simple sheet supported only along two edges. These results demonstrate the stiffening from the internal infinitesimal mechanism and the doubly curved shape which allow for high stiffness to be achieved using panels made from thin sheets.

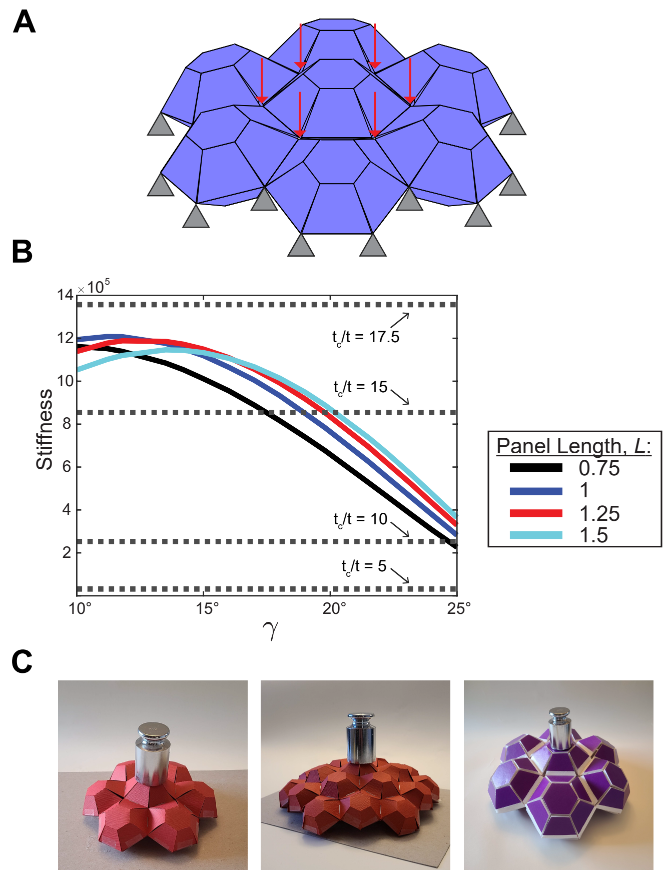

Figure 5.12: Stiffness analysis of the pop-up kirigami dome. (A) In the stiffness analysis, the outer perimeter was pinned and small vertical displacements were applied to the interior nodes of the structure. (B) The stiffness of the pop-up kirigami structures decreases as γ increases. For comparison, the stiffness of curved sheets with thickness t_c are shown in dashed lines, where t is the thickness of the pop-up kirigami. (C) From left to right: 7-cell paper structure (mass = 17 g), 19-cell paper structure (mass = 28 g), and 7-cell foam board structure (mass = 57 g). Each holds a 500 g load without a noticeable deformation.

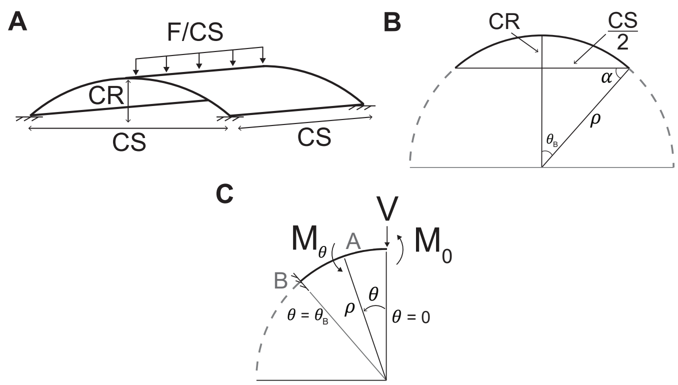

Figure 5.13: The analytical stiffness of a curved sheet used to compare out-of-plane stiffness. (A) The sheet was restrained along two edges and a load was applied at the center. (B) The sheet dimensions CR and CS, related to the radius of curvature ρ. (C) Free-body diagram of half of the curved sheet.

5.5.1 Analytical Solution for Stiffness of a Curved Sheet

The analytical solution for the stiffness of a curved sheet restrained along two edges (5.13(A)) can be calculated using Castigliano's Theorem. The theorem states that the displacement (or rotation) at a point on a beam due to a load (or moment) Q is calculated as:

$$\delta_q = \frac{\delta U}{\delta Q} = \int_0^l \frac{M}{EI}\frac{\delta M}{\delta Q}\mathrm{d}x \tag{5.5}$$

where U is the potential energy, M is the bending moment, E is the Young's modulus, and x is the distance along the beam. We can use Castigliano's Theorem in cylindrical coordinates to solve for the vertical displacement of a curved sheet due to a load applied at the centerline (Figure 5.13(A)). Due to symmetry, we look at only half of the sheet subjected to a vertical force F and compute the shear at the free end to be $V = F/2$. We consider a curved sheet with a height equal to the average clear rise of the pop-up structures (= 0.7), denoted as CR. We assume the width and length of the sheet is equal to the average clear span of the structures, CS (= 7). To transform into cylindrical coordinates, we need to relate these quantities to the radius of curvature (ρ) of the sheet (Figure 5.13(B)).

$$\rho^2 = (\rho - \mathrm{CR})^2 + \Big(\frac{\mathrm{CR}}{2}\Big)^2 \tag{5.6}$$

$$\rho = \frac{1}{2}\mathrm{CR} + \frac{1}{8}\frac{\mathrm{CS}^2}{\mathrm{CR}} \tag{5.7}$$

We need expressions for $\frac{\delta M_\theta}{\delta V}$ and $\frac{\delta M_\theta}{\delta M_0}$ to use Castigliano's Theorem, so we sum the moments at point A:

$$-M_\theta + V\rho\sin\theta - M_0 = 0 \tag{5.8}$$

$$M_\theta = V\rho\sin\theta - M_0 \tag{5.9}$$

$$\frac{\delta M_\theta}{\delta V} = \rho\sin\theta \qquad \frac{\delta M_\theta}{\delta M_0} = -1 \tag{5.10}$$

Now we can use the theorem to get an expression for the rotation due to the end moment M_0. We integrate from $\theta = 0$ to $\theta = \theta_B$, where θ_B is the angle at the support: $\theta_B = \pi/2 - \sin^{-1}((\rho - \text{CR})/\rho)$. The expression for the rotation due to M_0 is

$$\delta_{M_0} = \int_0^{\theta_B} \frac{V\rho(\sin\theta - M_0)}{EI}(-1)\rho\,\mathrm{d}\theta = \frac{V\rho^2}{EI}\big[\cos\theta_B - 1\big] + \frac{M_0\rho}{EI}\theta_B, \tag{5.11}$$

and the expression for the displacement due to the end force V is

$$\delta_V = \int_0^{\theta_B} \frac{(V\rho\sin\theta - M_0)}{EI}\rho^2\sin\theta\mathrm{d}\theta = \frac{V\rho^3}{2EI}\big[\theta_B - \sin\theta_B\cos\theta_B\big] + \frac{M_0\rho^2}{EI}\big[\cos\theta_B - 1\big]. \tag{5.12}$$

Due to symmetry, the rotation due to the moment M_0 is zero at the free end:

$$\frac{V\rho^2}{EI}[\cos\theta_B - 1] + \frac{M_0\rho}{EI}\theta_B = 0 \tag{5.13}$$

$$\frac{-V\rho}{\theta_B}[\cos\theta_B - 1] = M_0 \tag{5.14}$$

We can plug Equation 5.14 into Equation 5.12 to solve for the end displacement in terms of $V, \rho, E, I,$ and θ_B, all of which are known geometric or material properties. The stiffness of the curved sheet is found using $K = F/\Delta$, where $F = 1$ and $\Delta = \delta_V$.

5.5.2 Changing the Loading Direction

We also investigated the stiffness of the seven-cell structure with $\gamma = 20°$ and $L = 1.5$ for different loading directions (Figure 5.14). The loads were applied at the same six interior nodes as the previous analysis, and the load direction was changed in the *x-z* and *x-y* planes. The structure exhibits the highest stiffness in response to horizontal loads in the *x-y* plane. While there are three axes of radial symmetry for the structure, the stiffness is uniform in all *x-y* directions, meaning there

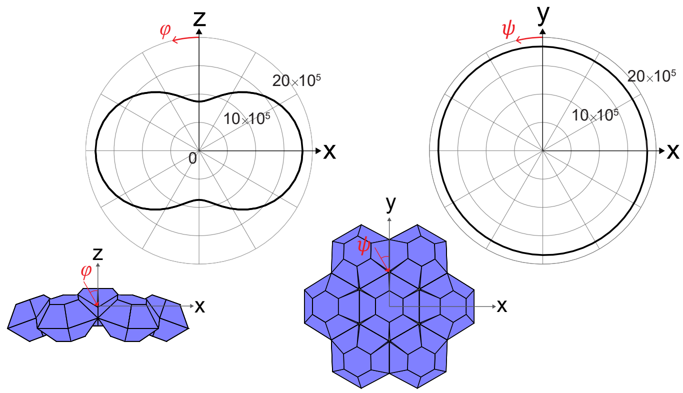

Figure 5.14: The stiffness of the pop-up structure in the *x*-*z* and *x*-*y* planes shown as radial plots where the distance from the center indicates the stiffness magnitude. The angles ϕ and ψ represents the loading direction in a given plane. The structure exhibits the largest stiffness in the *x*-*y* plane (horizontal loading).

will be a high stiffness regardless of how horizontal loads are applied. When loaded vertically in the z-direction, the structure has about half the stiffness in comparison to the horizontal directions, but this stiffness is still high, as shown in Figure 5.14. These results indicate that the pop-up structures are adaptable to loads that change directions, such as wind loads.

5.6 Continuous Equilibrium for Pop-up Kirigami Domes

The pop-up dome structure has two DOFs, one corresponding to each step: assembly from a flat sheet (defined by ϕ_1) and a dome-forming motion (ϕ_2) (Figure 5.15(A)). Under gravity, the structure would collapse to a flat state where $\phi_1 = 0°$ and $\phi_2 = 0°$. To aid in deployment, we can program a specific set of motions using springs using the framework presented in Chapters 2 and 3. The desired motion that we focus on is to first fully assemble the structure (increasing ϕ_1 while ϕ_2 remains at 0) and then forming a dome shape (increasing ϕ_2). We assume that the panels are made from a material with uniform thickness and mass density equal to 1 kg/m. The panel dimensions are given in Figure 5.15(B).

We used a set of torsional springs placed within the hexagonal cells (Spring 1 Figure 5.15(C)) to program the desired motion of full assembly and torsional springs placed between the cells for the dome-forming step (Spring 2). Since the assembly step must be completed before the dome-forming step begins, we programmed two sequential paths: the assembly path which ends with a stable state, and the dome-forming path which is designed to have continuous equilibrium. To enforce that the dome-forming path will be stable, we used a constraint that requires $\nabla \mathrm{PE_T}$ to be aligned with a desired gradient.

$$\nabla_d = \begin{cases} [-1, 0], & \phi_1 < 100°. \end{cases} \tag{5.15}$$

This constraint inherently requires there to be a local potential energy minimum at the end of path 1. To ensure that the local minimum is a stable state, we introduce an additional constraint to control the concavity of $\mathrm{PE_T}$ along path 1.

$$-\frac{d^2\mathrm{PE}_{\mathrm{T}_{\text{path 1}}}}{d\phi_1^2} \leq 0 \tag{5.16}$$

Figure 5.15(D) shows the potential energy of the system. Without springs, the pop-up structure collapses to the configuration where $\phi_1 = 0°$ and $\phi_2 = 0°$ (minimum in $\mathrm{PE_G}$). With springs, there is a potential energy valley at the end of the assembly step (Path 1, Figure 5.15(E)). The fluctuation in potential energy along the dome-forming step (Path 2) has been reduced by 95.7%; without springs, the fluctuation is 519 N-m and with springs it is 22.3 N-m. The optimized spring properties are L_{01} = 2.65 m, k_1 = 197 N/m; L_{02} = 2.3 m, k_2 = 149 N/m; α_3 = 3.68, k_3 = 200 N-m/rad.

We also investigated the actuation force needed to reconfigure the structure into its dome-like shape (moving along path 2). External forces are required to keep the structure in its dome-like shape; with the implementation of continuous equilibrium, lower forces will be required. We used the method described in Chapter 4 to move the structure through path 2 and obtain the resultant force (F_r in Figure 5.15(F)). Roller supports were added at the outer nodes of the bottom hexagonal panels (excluding those of the center cell) and the nodes of the top center hexagonal panel. With the addition of optimized springs, F_r is reduced by 82% on average.

5.7 Concluding Remarks

In this chapter, we presented a novel design for a pop-up structure that achieves dome-like curvature from flat panels. The system starts with a kirigami-inspired pattern of two sheets, cut into hexagonal and trapezoidal panels and fastened to create an array of cells that assemble into a 3D structure. We demonstrated that the system can accommodate finite thickness and maintain nearly rigid panels as it deforms into a structure with positive Gaussian curvature. With this design, we have the potential to create large, dome-like structures from flat sheets, taking advantage of the simplified fabrication and rapid deployment that are made possible by origami and kirigami designs.

We identified the internal mechanism that leads to the formation of a doubly curved shape and showed that the higher deformation modes of the structure become restricted as the curvature increases. We studied geometric variations of the structure by changing the panel angle γ and panel

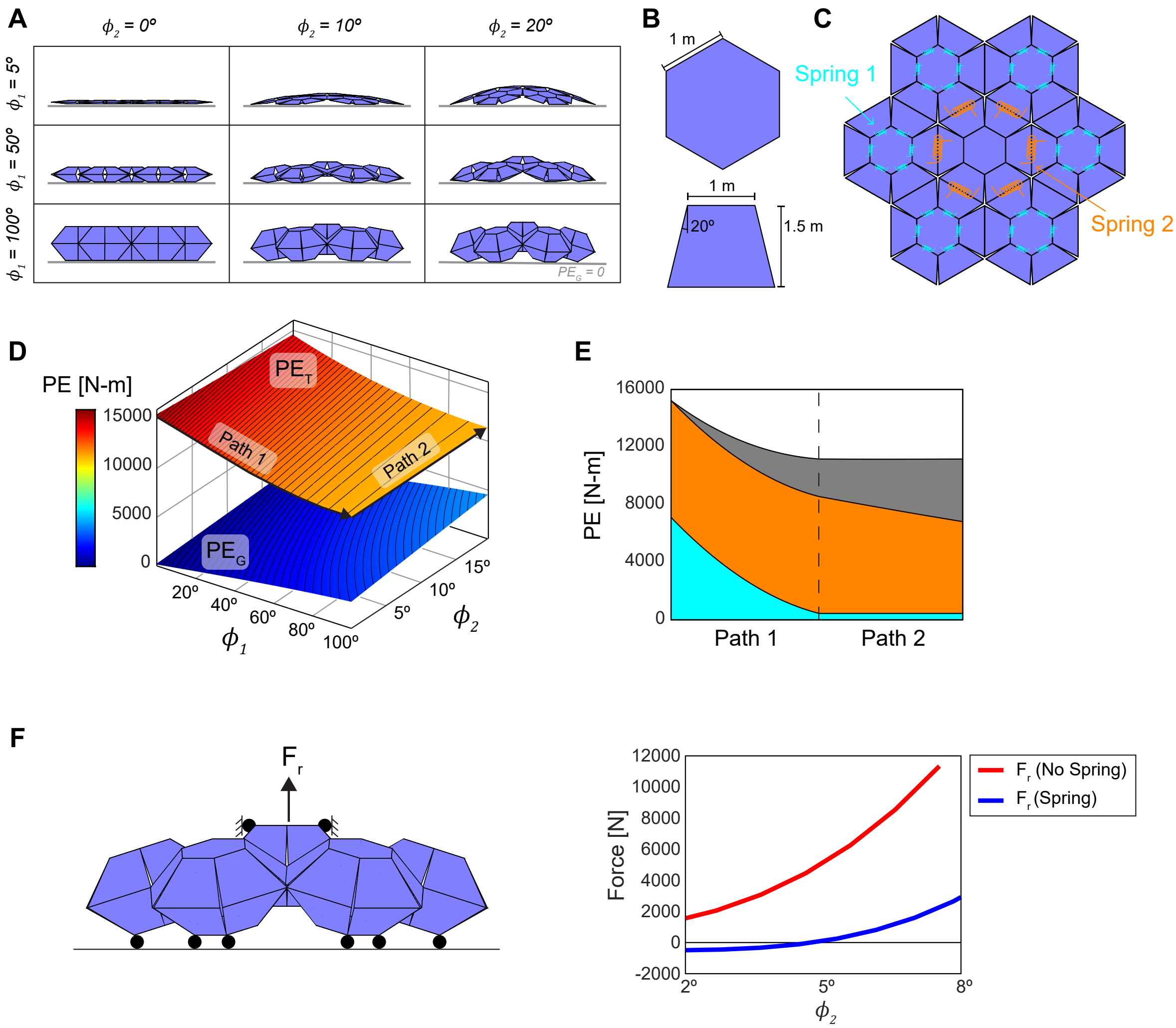

Figure 5.15: Designing the pop-up kirigami dome to have continuous equilibrium. (A) The pop-up kirigami dome has two DOFs: an assembly motion, defined by ϕ_1, and a dome-forming motion, defined by ϕ_2. (B) Dimensions of the panels used in the pop-up kirigami dome. (C) We added two sets of torsional springs: one set within each of the six outer cells for the assembly step, and one set connecting the cells for the dome-forming step. (D) The first path (assembly) is moving to a stable state at $\phi_1 = 100°$, where the cells are fully closed. The second path (dome-forming) is designed to have continuous equilibrium, where ϕ_2 increases to 20° (contour line interval = 100 N-m). (E) Potential energy of the structure along the paths. At the end of path 1, there is a local minimum in potential energy, indicating a stable state. Along path two, the fluctuation in potential energy is reduced by 95.7%. (F) Force analysis of the pop-up structure. To investigate the actuation force required in the dome-forming step, we applied a vertical force F_r on the center cell and applied roller supports. The actuation force for the system with springs is reduced by 82% on average when compared to the system without springs.

length L. Structures with smaller γ result in a higher clear rise to clear span ratio, a metric we use to describe curvature. When studying the volume of the systems, we found that structures with large γ and small panel length L result in more geometrically efficient designs that can enclose a larger volume for a smaller volume of total structure. We also found that by adding more cells, the shape trends towards the classic dome shape used in architecture. A stiffness analysis showed that the dome-like shape and infinitesimal mechanism makes the pop-up kirigami structure 1,000 to 5,000 times stiffer than a curved sheet with the same total thickness that is supported only along two edges. We also showed that the structure has high stiffness regardless of the loading direction.

Finally, we implement the design framework presented in Chapters 2 and 3 to program desired motions into the pop-up kirigami structure. The resulting design reduces the fluctuation in potential energy during the dome-forming step by 95.7%. This system is the first self-stiffening kirigami structure that can deform into a dome-like shape. By integrating continuous equilibrium properties into the design, the structure has potential to be used for rapidly deployable enclosures, reflectors, architectural components, and other robust structures with positive double curvature.

CHAPTER 6

Conclusions and Future Work

The purpose of this dissertation is to present a framework for designing reconfigurable structures to have continuous equilibrium such that they are stable and can be efficiently actuated. This chapter highlights the main contributions of the dissertation as well as several areas for future work.

In Chapter 2, we introduced a framework for transforming reconfigurable structures into systems with continuous equilibrium. Using simple four-bar linkages, we demonstrate how an optimization scheme can design the addition of springs that minimize the fluctuation in potential energy throughout the kinematic path of a structure. We explore several types of springs and discuss how symmetry affects which spring types are most effective at obtaining continuous equilibrium. We are able to design systems to have continuous equilibrium even as they are reoriented with respect to a global reference frame, thus maintaining functionality at multiple orientations. The framework can be used to design more complex structures as well, such as linkages that carry external loads or three-dimensional structures.

Chapter 3 extends the work of Chapter 2 to reconfigurable systems with more than one degree of freedom. We begin by optimizing springs to achieve continuous equilibrium throughout the potential energy space of multi-DOF systems. We demonstrate how springs can enable continuous equilibrium for a one-, two-, and three-DOF Watt's linkage. Next, we discuss how the framework can be adapted to program specific motions in multi-DOF systems, including adding stable paths and stable configurations. We apply these methods to an excavator linkage system and a five-fold origami vertex to show how more complex, practical structures can be designed.

The applications of continuous equilibrium to physical systems are explored in Chapter 4. Mechanical models of both linkage systems and origami systems are used to compute the forces required to actuate reconfigurable structures through their kinematic path. The computational results show that by adding optimized springs, we can reduce the actuation forces needed to reconfigure the structures. We then discuss the methods used for physical prototype fabrication and testing. The preliminary results show good agreement with the computational models. We conclude this chapter with a brief discussion of the stiffness and locking of continuous equilibrium structures.

Chapter 5 presents a novel pop-up kirigami structure that deploys into a dome-like shape and has high stiffness. The structure starts as two flat sheets, assembles into 3D, and deforms into a shape with dome-like curvature thanks to an internal infinitesimal mechanism. Changing the initial kirigami pattern has a dramatic effect on the final shape, and these properties were explored through a parametric study. The bar and hinge method is used to investigate the stiffness of the structure, and it is shown to have high stiffness in its doubly curved shape. Finally, we apply the continuous equilibrium framework to the dome-like structure and design it to have sequential stable paths to aid with deployment.

6.1 Key Contributions of this Dissertation

The following items are the key contributions of the research presented in this dissertation.

Universal design framework for systems with continuous equilibrium. The design framework presented in this dissertation can be applied to any two- or three-dimensional reconfigurable system. The inputs to the optimization problem are simply the system kinematics and spring locations. Any number of springs can be used in the design problem, and the optimization can handle combinations of different types of springs in one structure. The optimization framework was written in MATLAB and is made open-access on GitHub at (https://github.com/mariared-DRSL/Continuous-equilibrium-examples).

Reorientation. The framework can be used to design reconfigurable structures that stay in continuous equilibrium even as they are reoriented with respect to a global reference frame. Even as the effect of gravity changes, the system will remain stable and can be easily moved through its kinematic path. This ability to maintain functionality at multiple orientations extends the benefits of continuous equilibrium to systems with complex ranges of motion.

Efficient actuation under gravity. For applications in civil engineering, gravity has a major effect on reconfiguration and stability. Typically, large forces are required to move a reconfigurable structure when gravity is acting on it. By adding springs that put the system in continuous equilibrium, the forces needed for actuation are significantly reduced. We verify this phenomenon through computational mechanical models and physical prototypes.

Programming stable motion in multi-DOF systems. Many real-life reconfigurable structures have more than one degree of freedom (DOF). Using the design framework, optimized springs can be used in multi-DOF systems to create motion paths that are in continuous equilibrium and are globally stable. Sequential paths can be programmed so that desired motions take place in a specific order, enabling multi-functionality.

Dome-like kirigami structures with high stiffness. Origami and kirigami structures made from flat sheets are inherently flexible, due to their high number of DOFs. One way to improve stiffness of a flexible sheet is to add positive Gaussian (dome-like) curvature, but this phenomenon is difficult to achieve using origami and kirigami methods. In this dissertation, we introduce a novel pop-up, dome-like structure that is made from a flat kirigami pattern and has high stiffness. When the design framework is used to program a sequential set of motion paths, the dome can be assembled and deployed in a stable manner and the actuation forces are reduced. The pop-up kirigami dome is just one example of the functional reconfigurable structures that can be designed using the framework presented in this dissertation.

6.2 Future Work

This dissertation leads to several avenues for future work.

Multi-objective optimization. The results presented in this dissertation are largely based on ideal cases where the design is focused only on obtaining continuous equilibrium. For real-world applications, limitations on material and cost would have a significant impact on the design and could be incorporated into the optimization scheme. It would be beneficial to utilize multi-objective optimization to weigh factors such as cost, material weight, stiffness, actuation force, spring type, and spring locations. We envision that such a tool could be integrated into our design framework to make it more applicable to real systems.

Systematic experimental testing with actuators. The preliminary experimental results shown in Chapter 4 and Appendix A could be expanded upon. This work would benefit from more systematic experimental testing to quantify the deviation from the idealized computational results. Friction plays a large role in physical reconfigurable structures, so further investigation into the friction caused by springs and spring attachments - as well as solutions for mitigating its effects - would be beneficial. Different methods of attaching springs could be explored as well. Installing actuators onto physical prototypes would be a major step towards the actualization of civil engineering-scale continuous equilibrium reconfigurable structures. Systems could be reconfigured using linear actuators which apply a force or torsional actuators which apply a moment. With actuators installed, data could be collected about the forces, range of motion, and actuation energy required for motion. This presents a fruitful area of research for quantifying the benefits of transforming structures into continuous equilibrium systems. Additionally, the techniques used to install the actuators is an area in need of further study.

Nonlinear and custom springs. The potential energy formulation used in the design framework is based on the assumption that all springs have a linear stiffness, i.e., that the force required to deform the spring scales linearly with the amount of deformation. It is possible to use nonlinear springs, where the force required to deform the spring follows a desired nonlinear relationship with the deformation [130]. If the force-deformation relationship of nonlinear springs were tailored precisely, it could allow the spring potential energy to directly offset the potential energy due to gravity. This may result in a system which needed multiple linear springs to obtain continuous equilibrium to instead only require one nonlinear spring, thus reducing the complexity and cost of a system. We envision that the design framework could be adapted to compute the nonlinear spring stiffness behavior as a function of the system kinematics. Custom springs could then be fabricated to match the optimized nonlinear stiffness. For the physical prototypes shown in this dissertation, we purchased springs from an online retailer and often had to choose springs that did not perfectly match the optimized properties that were obtained using the design framework. A possibility for improvement is to fabricate custom springs with properties tailored to a specific system. This could aid in designing sleeker spring attachments and minimize the difference between computational and experimental results.

Application to bi- and multi-stable structures. The optimization problem used to minimize the fluctuation in potential energy could be used to reduce the forces that bi-stable structures experience during snap-though instabilities. Rather than minimizing the fluctuation in potential energy due to gravity, the strain energy fluctuation could be minimized, leading to shallower energy valleys. A similar method to adding a stable configuration in Chapter 3 could also be implemented to program the precise locations of the energy valleys. Utilizing the optimization method could enable the design of shape changing structures with more controlled motion while still taking advantage of multi-stability.

Scaling up. The physical prototypes of systems with springs provide a starting point for the fabrication of larger structures designed to have continuous equilibrium. At a larger scale, adding discrete torsional springs may not be feasible. Other ways to incorporate programmable stiffness at the joints or hinges of a structure, such as material deformation, could be explored. The effect of coulomb friction also increases as systems scale up in size and weight, and the effect of friction on continuous equilibrium behavior could be studied. Finally, designers are more likely to see a nonlinear structural response when larger systems reconfigure through their kinematic path under gravity. It may be possible to harness this nonlinear response to aid with achieving continuous equilibrium.

APPENDIX A

Continuous Equilibrium Videos

The PDF version of this document contains videos which can also be accessed at www.youtube.com/@deployableandreconfigurabl988.

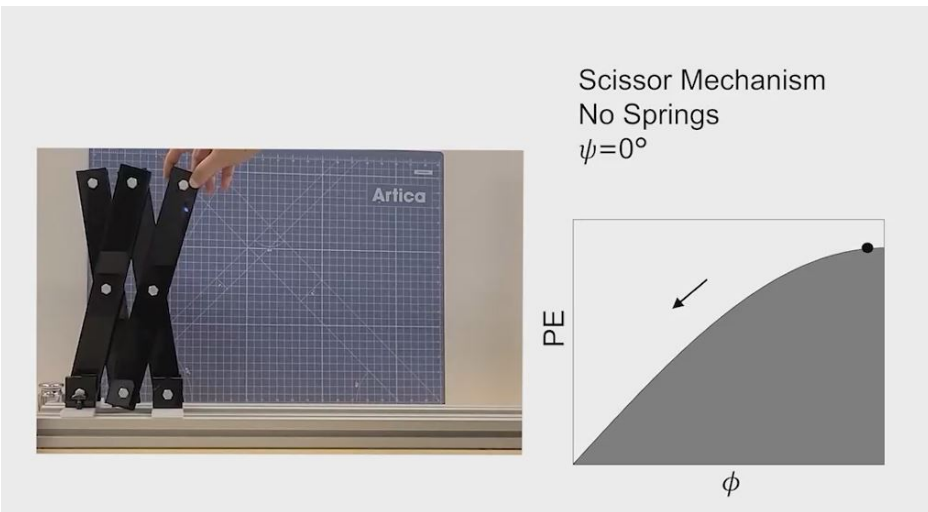

Video A.1: Scissor Mechanism at $\psi = 0°$ with no springs. The system requires a constant force to avoid collapse due to gravity.

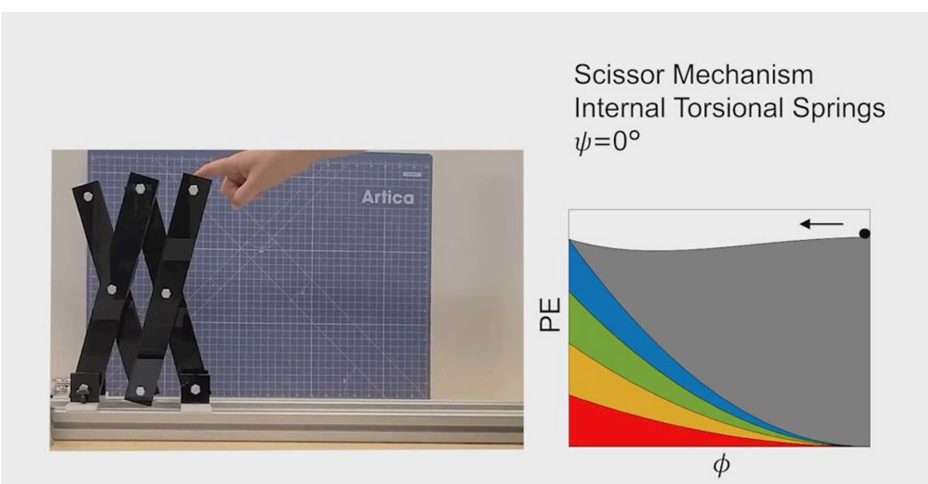

Video A.2: Scissor Mechanism at $\psi = 0°$ with internal torsional springs. This system exhibits continuous equilibrium system behavior and remains stable at all configurations.

Video A.3: Watt's linkage prototype at $\psi = 0°$ with no springs. The system requires a constant force to avoid collapse due to gravity.

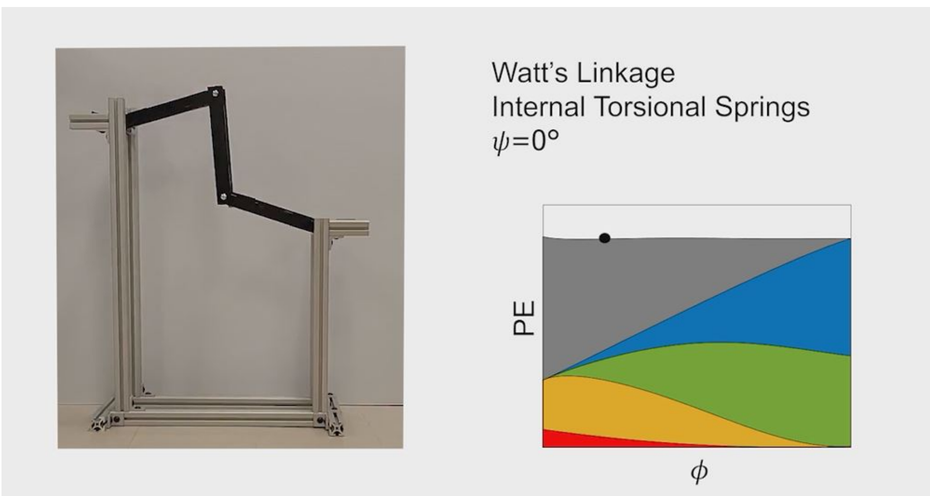

Video A.4: Watt's linkage prototype at $\psi = 0°$ with internal torsional springs. This system exhibits continuous equilibrium system behavior and remains stable at all configurations.

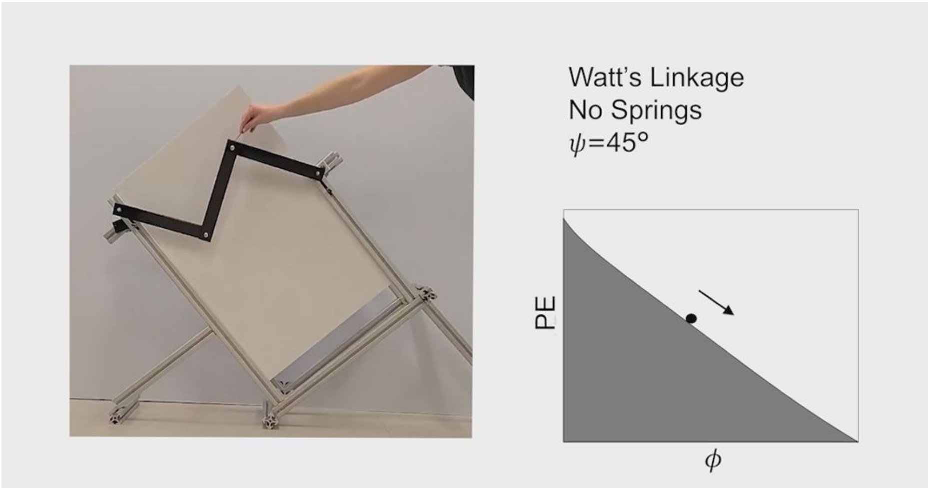

Video A.5: Watt's linkage prototype at $\psi = 45°$ with no springs. This system requires a constant force to avoid collapse due to gravity.

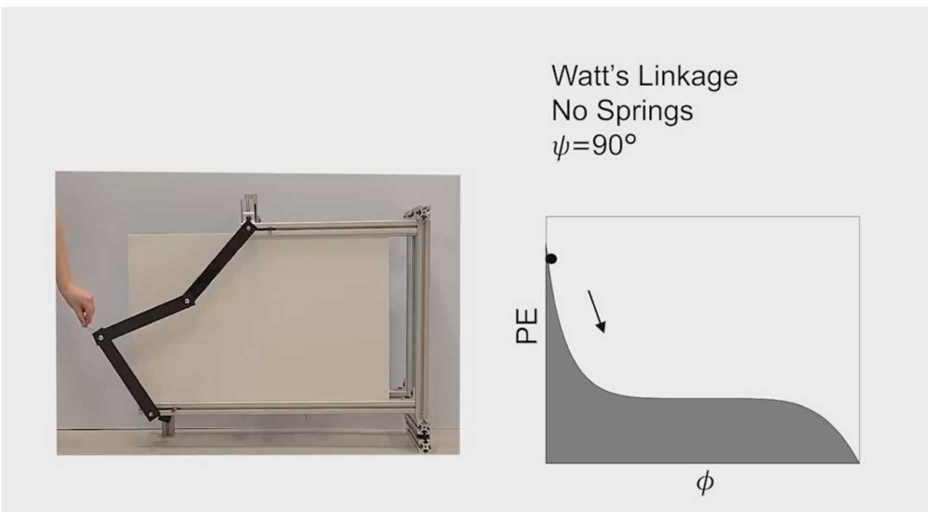

Video A.6: Watt's linkage prototype at $\psi = 90°$ with no springs. This system is in continuous equilibrium in a small range in the center of the kinematic path, but collapses when moved outside of this range.

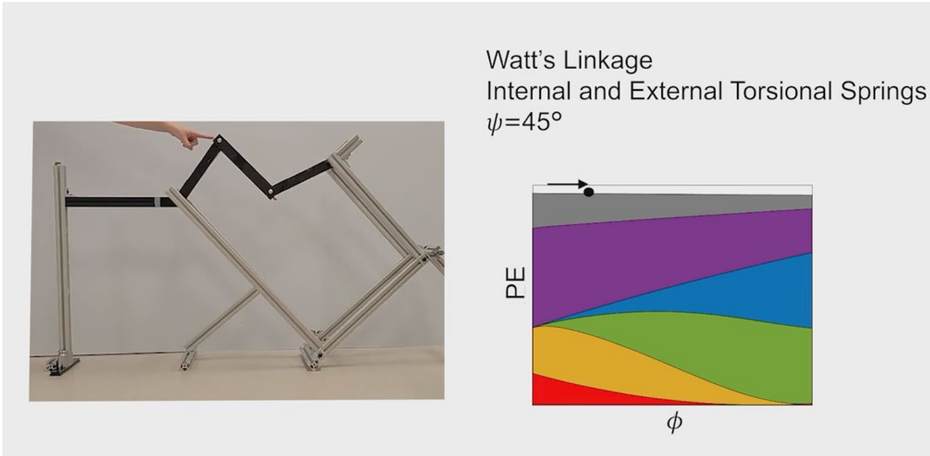

Video A.7: Watt's linkage prototype at $\psi = 45°$ with internal and external torsional springs. This system has been reoriented and maintains continuous equilibrium, and remains stable at all configurations.

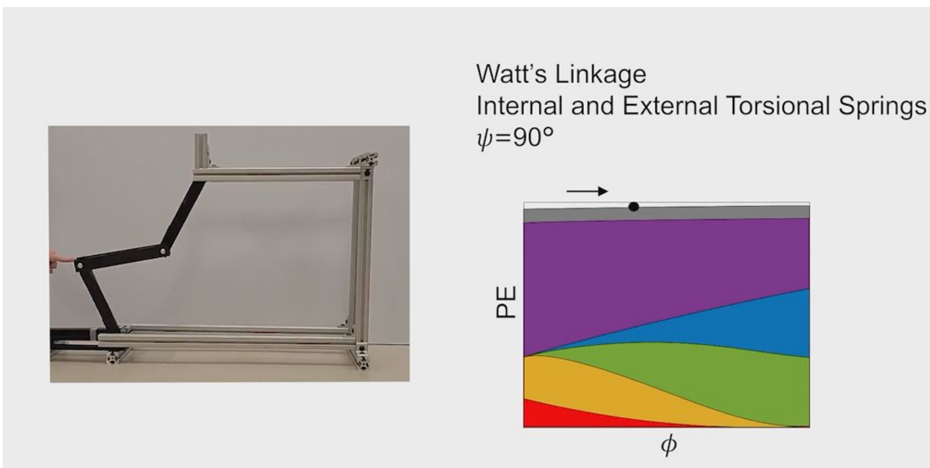

Video A.8: Watt's linkage prototype at $\psi = 90°$ with internal and external torsional springs. This system has been reoriented and maintains continuous equilibrium, and remains stable at all configurations.

BIBLIOGRAPHY

[1] Y. Chen, J. Feng, and Y. Zhang. A necessary condition for stability of kinematically indeterminate pin-jointed structures with symmetry. *Mechanics Research Communications*, 60:64–73, 2014.

[2] Y. Chen, J. Feng, and Y. Liu. A group-theoretic approach to the mobility and kinematic of symmetric over-constrained structures. *Mechanism and Machine Theory*, 105:91–107, 2016.

[3] S. Pellegrino and C. R. Calladine. Matrix analysis of statically and kinematically indeterminate frameworks. *International Journal of Solids and Structures*, 22:409–428, 1986.

[4] C. R. Calladine and S. Pellegrino. First-order infinitesimal mechanisms. *International Journal of Solids and Structures*, 27:505–515, 1991.

[5] Image licensed under CC BY-SA 2.0 (Loz Pycock). `https://www.flickr.com/photos/99245765@N00/5002172010`.

[6] M. A. A. Wahit, S. A. Ahmad, M. H. Marhaban, C. Wada, and L. I. Izhar. 3d printed robot hand structure using four-bar linkage mechanism for prosthetic application. *Sensors (Switzerland)*, 20:1–22, 2020.

[7] G. Roos, H. Leysen, S. Van Wassenbergh, A. Herrel, P. Jacobs, M. Dierick, P. Aerts, and D. Adriaens. Linking morphology and motion: A test of a four-bar mechanism in seahorses. *Physiological and Biochemical Zoology*, 82:7–19, 2009.

[8] E. Steinhardt, N. S. P. Hyun, J. S. Koh, G. Freeburn, M. H. Rosen, F. Z. Temel, S. N. Patek, and R. J. Wood. A physical model of mantis shrimp for exploring the dynamics of ultrafast systems. *Proceedings of the National Academy of Sciences of the United States of America*, 118, 2021.

[9] R. Z. Bikowski, C. Galinski, and C. B. Pedersen. Four-bar linkage mechanism for insectlike flapping wings in hover: Concept and an outline of its realization. *Journal of Mechanical Design*, 127:817–824, 2005.

[10] P. A. Simionescu and D. Beale. Optimum synthesis of the four-bar function generator in its symmetric embodiment: The ackermann steering linkage. *Mechanism and Machine Theory*, 37:1487–1504, 2002.

[11] T. Essomba. Design of a five-degrees of freedom statically balanced mechanism with multi-directional functionality. *Robotics*, 10:1–21, 2021.

[12] J. K. Pickard, J. A. Carretero, and J. P. Merlet. Appropriate analysis of the four-bar linkage. *Mechanism and Machine Theory*, 139:237–250, 2019.

[13] J. M. McCarthy and G. S. Soh. *Geometric Design of Linkages*. Springer Science and Business Media, 2nd edition, 2010.

[14] S. Wu, Q. Ze, J. Dai, N. Udipi, G. H. Paulino, and R. Zhao. Stretchable origami robotic arm with omnidirectional bending and twisting. *Proceedings of the National Academy of Sciences of the United States of America*, 118:1–9, 2021.

[15] T. Yamamoto, N. Iwatsuki, and I. Ikeda. Automated kinematic analysis of closed-loop planar link mechanisms. *Machines*, 8, 2020.

[16] R. Yang and P. S. Krishnaprasad. On the geometry and dynamics of floating four-bar linkages. *Dynamics and Stability of Systems*, 9:19–45, 1994.

[17] Y. Tang, Z. Chang, X. Dong, Y. Hu, and Z. Yu. Nonlinear dynamics and analysis of a four-bar linkage with clearance. *Frontiers of Mechanical Engineering*, 8:160–168, 2013.

[18] H. S. Yan and R. C. Soong. Kinematic and dynamic design of four-bar linkages with variable input speed and external applied loads. *Transactions of the Canadian Society for Mechanical Engineering*, 26:281–310, 2002.

[19] M. R. Smith and L. Maunder. Inertia forces in a four-bar linkage. *Journal of Mechanical Engineering Science*, 9:218–225, 1967.

[20] R. S. Berkof. Complete force and moment balancing of inline four-bar linkages. *Mechanism and Machine Theory*, 8:397–410, 1973.

[21] T. Wongratanaphisan and M. O.T. Cole. Analysis of a gravity compensated four-bar linkage mechanism with linear spring suspension. *Journal of Mechanical Design, Transactions of the ASME*, 130:1–8, 2008.

[22] P. Y. Lin, W. B. Shieh, and D. Z. Chen. Design of perfectly statically balanced one-dof planar linkages with revolute joints only. *Journal of Mechanical Design, Transactions of the ASME*, 131:0510041–0510049, 2009.

[23] G. Radaelli, J. A. Gallego, and J. L. Herder. An energy approach to static balancing of systems with torsion stiffness. *Journal of Mechanical Design, Transactions of the ASME*, 133, 2011.

[24] J. Zhao, Z. Yan, and L. Ye. Design of planar four-bar linkage with n specified positions for a flapping wing robot. *Mechanism and Machine Theory*, 82:33–55, 2014.

[25] J. J. Moy, C. S. Tan, S. Mohammad, and A. Abidin. State-of-art review on deployable scissor structure in construction. *Structures*, 42:160–180, 2022.

[26] Image licensed under CC BY-SA 2.0 DE. https://en.wikipedia.org/wiki/Aerial_work_platform#/media/File:Hebebuehne_Scissorlift.jpg.

[27] Image copyright Joseph Xu. Image used with permission.

[28] Z. You. Motion Structures extend their reach. *Materials Today*, 10(12):52–57, 2007.

[29] Image licensed under CC BY-SA 3.0. https://en.wikipedia.org/wiki/Ackermann_steering_geometry#/media/File:Ackermann_simple_design.svg.

[30] E. T. Filipov, T. Tachi, and G. H. Paulino. Origami tubes assembled into stiff, yet reconfigurable structures and metamaterials. *Proceedings of the National Academy of Sciences of the United States of America*, 112:12321–12326, 2015.

[31] M. Schenk and S. D. Guest. Origami folding: A structural engineering approach. *Origami 5: Fifth International Meeting of Origami Science, Mathematics, and Education*, pages 291–303, 2016.

[32] Y. Zhu, M. Birla, K. R. Oldham, and E. T. Filipov. Elastically and plastically foldable electrothermal micro-origami for controllable and rapid shape morphing. *Advanced Functional Materials*, 2003741:1–10, 2020.

[33] T. G. Leong, B. R. Benson, E. K. Call, and D. H. Gracias. Thin film stress driven self-folding of microstructured containers. *Small*, 4:1605–1609, 2008.

[34] E. Hawkes, B. An, N. M. Benbernou, H. Tanaka, S. Kim, E. D. Demaine, D. Rus, and R. J. Wood. Programmable matter by folding. *Proceedings of the National Academy of Sciences of the United States of America*, 107:12441–12445, 2010.

[35] K. Kuribayashi, K. Tsuchiya, Z. You, D. Tomus, M. Umemoto, T. Ito, and M. Sasaki. Self-deployable origami stent grafts as a biomedical application of ni-rich tini shape memory alloy foil. *Materials Science and Engineering A*, 419:131–137, 2006.

[36] E. T. Filipov, G. H. Paulino, and T. Tachi. Deployable sandwich surfaces with high out-of-plane stiffness. *Journal of Structural Engineering*, 145:04018244, 2019.

[37] A. E. Del Grosso and P. Basso. Adaptive building skin structures. *Smart Materials and Structures*, 19, 2010.

[38] Samuel Felton, Michael Tolley, Erik Demaine, Daniela Rus, and Robert Wood. A method for building self-folding machines. *Science*, 345(6197):644–646, 2014.

[39] S. A. Zirbel, B. P. Trease, M. W. Thomson, R. J. Lang, S. P. Magleby, and L. Howell. Hanaflex: a large solar array for space applications. *Micro- and Nanotechnology Sensors, Systems, and Applications VII*, 2015.

[40] A. P. Thrall and C. P. Quaglia. Accordion shelters: A historical review of origami-like deployable shelters developed by the us military. *Engineering Structures*, 59:686–692, 2014.

[41] T. U. Lee and J. M. Gattas. Geometric design and construction of structurally stabilized accordion shelters. *Journal of Mechanisms and Robotics*, 8:1–8, 2016.

[42] S. A. Zirbel, R. J. Lang, M. W. Thomson, D. A. Sigel, P. E. Walkemeyer, B. P. Trease, S. P. Magleby, and L. Howell. Accommodating thickness in origami-based deployable arrays. *Journal of Mechanical Design, Transactions of the ASME*, 135:1–11, 2013.

[43] Y. Li. A method of designing a prescribed energy landscape for morphing structures. *International Journal of Solids and Structures*, 242, 2022.

[44] A. Rafsanjani, Y. Zhang, B. Liu, S. M. Rubinstein, and K. Bertoldi. Kirigami skins make a simple soft actuator crawl. *Science Robotics*, 3:1–8, 2018.

[45] L. Jin, A. E. Forte, B. Deng, A. Rafsanjani, and K. Bertoldi. Kirigami-inspired inflatables with programmable shapes. *Advanced Materials*, 32, 2020.

[46] M. Redoutey, A. Roy, and E. T. Filipov. Pop-up kirigami for stiff, dome-like structures. *International Journal of Solids and Structures*, 229:111–140, 2021.

[47] T. Tachi. Rigid-foldable thick origami. *Origami 5: Fifth International Meeting of Origami Science, Mathematics, and Education*, pages 253–263, 2016.

[48] R. J. Lang, K. A. Tolman, E. B. Crampton, S. P. Magleby, and L. L. Howell. A review of thickness-accommodation techniques in origami-inspired engineering. *Applied Mechanics Reviews*, 70:1–20, 2018.

[49] S. J.P. Callens and A. A. Zadpoor. From flat sheets to curved geometries: Origami and kirigami approaches. *Materials Today*, 21:241–264, 2018.

[50] J. T.B. Overvelde, T. A. De Jong, Y. Shevchenko, S. A. Becerra, G. M. Whitesides, J. C. Weaver, C. Hoberman, and K. Bertoldi. A three-dimensional actuated origami-inspired transformable metamaterial with multiple degrees of freedom. *Nature Communications*, 7:1–8, 2016.

[51] D. Shi, W. Zhang, W. Zhang, and X. Ding. A review on lower limb rehabilitation exoskeleton robots. *Chinese Journal of Mechanical Engineering (English Edition)*, 32:1–11, 2019.

[52] H. Li, R. Hu, I. Alhashim, and H. Zhang. Foldabilizing furniture. *ACM Transactions on Graphics*, 34, 2014.

[53] S. Barbarino, O. Bilgen, R. M. Ajaj, M. I. Friswell, and D. J. Inman. A review of morphing aircraft. *Journal of Intelligent Material Systems and Structures*, 22:823–877, 2011.

[54] Image licensed under CC BY-SA (Matthew T. Rader). MatthewTRader.com. https://commons.wikimedia.org/wiki/File:Caterpillar_330_Excavator.jpg.

[55] Image licensed under CC BY-SA 3.0 (Katy Lancaster). https://commons.wikimedia.org/wiki/File:AMiBA_1.jpg.

[56] Image licensed under CC BY 4.0.

[57] J. Greenwood, A. Avila, L. Howell, and S. Magleby. Conceptualizing stable states in origami-based devices using an energy visualization approach. *Journal of Mechanical Design, Transactions of the ASME*, 142:1–11, 2020.

[58] M. T. Tolley, S. M. Felton, S. Miyashita, D. Aukes, D. Rus, and R. J. Wood. Self-folding origami: Shape memory composites activated by uniform heating. *Smart Materials and Structures*, 23, 2014.

[59] T. van Manen, S. Janbaz, M. Ganjian, and A. A. Zadpoor. Kirigami-enabled self-folding origami. *Materials Today*, 32:59–67, 2020.

[60] N. Bassik, G. M. Stern, and D. H. Gracias. Microassembly based on hands free origami with bidirectional curvature. *Applied Physics Letters*, 95:1–4, 2009.

[61] T. G. Leong, C. L. Randall, B. R. Benson, N. Bassik, G. M. Stern, and D. H. Gracias. Tetherless thermobiochemically actuated microgrippers. *Proceedings of the National Academy of Sciences*, 106:703–708, 2009.

[62] J. H. Na, A. A. Evans, J. Bae, M. C. Chiappelli, C. D. Santangelo, R. J. Lang, T. C. Hull, and R. C. Hayward. Programming reversibly self-folding origami with micropatterned photo-crosslinkable polymer trilayers. *Advanced Materials*, 27:79–85, 2015.

[63] C. Coulais, A. Sabbadini, F. Vink, and M. van Hecke. Multi-step self-guided pathways for shape-changing metamaterials. *Nature*, 561:512–515, 2018.

[64] Y. Mao, K. Yu, M. S. Isakov, J. Wu, M. L. Dunn, and H. J. Qi. Sequential self-folding structures by 3d printed digital shape memory polymers. *Scientific Reports*, 5:1–12, 2015.

[65] J. Zhang, Y. Guo, W. Hu, and M. Sitti. Wirelessly actuated thermo- and magneto-responsive soft bimorph materials with programmable shape-morphing. *Advanced Materials*, 33, 2021.

[66] S. Xu, Z. Yan, K. Jang, W. Huang, H. Fu, J. Kim, Z. Wei, Matthew Flavin, Joselle McCracken, Renhan Wang, Adina Badea, Yuhao Liu, Dongqing Xiao, Guoyan Zhou, Jungwoo Lee, Ha Uk Chung, Huanyu Cheng, Wen Ren, Anthony Banks, Xiuling Li, Ungyu Paik, Ralph G. Nuzzo, Yonggang Huang, Yihui Zhang, and John A. Rogers. Assembly of micro/nanomaterials into complex, three-dimensional architectures by compressive buckling. *Science*, 347:154–159, 2015.

[67] X. Xu, A. Jagota, S. Peng, D. Luo, M. Wu, and C. Hui. Gravity and surface tension effects on the shape change of soft materials. *Langmuir*, 29(27):8665–8674, 2013.

[68] S. Kok, G. Radaelli, A. A. Nobaveh, and J. Herder. Neutrally stable transition of a curved-crease planar shell structure. *Extreme Mechanics Letters*, 49:101469, 11 2021.

[69] T. Tarnai. Zero stiffness elastic structures. *International Journal of Mechanical Sciences*, 45:425–431, 2003.

[70] M. Schenk and S. D. Guest. On zero stiffness. *Proceedings of the Institution of Mechanical Engineers, Part C: Journal of Mechanical Engineering Science*, 228:1701–1714, 2014.

[71] Image licensed under CC BY-SA 4.0.

[72] Image licensed under CC BY-SA 4.0 (Steven Pavlov). https://commons.wikimedia.org/wiki/File:Seattle_%E2%80%94_Fremont_Bridge_%E2%80%94_%282016-06-12%29,_01.jpg.

[73] Infinity zero gravity chair. https://www.caravancanopy.com/product/zero-gravity-chair-7/.

[74] M. Schenk, S. D. Guest, and J. L. Herder. Zero stiffness tensegrity structures. *International Journal of Solids and Structures*, 44:6569–6583, 2007.

[75] G. Chaudhary, S. G. Prasath, E. Soucy, and L. Mahadevan. Totimorphic assemblies from neutrally-stable units. *Proceedings of the National Academy of Sciences of the United States of America*, pages 1–6, 2021.

[76] S. D. Guest, E. Kebadze, and S. Pellegrino. A zero-stiffness elastic shell structure. *Journal of Mechanics of Materials and Structures*, 6:203–212, 2011. Image first published in Journal of Mechanics of Materials and Structures in Vol. 6 (2011) published by Mathematical Sciences Publishers.

[77] G. Radaelli. Reverse-twisting of helicoidal shells to obtain neutrally stable linkage mechanisms. *International Journal of Mechanical Sciences*, 202-203:106532, 2021.

[78] Y. Li and S. Pellegrino. A theory for the design of multi-stable morphing structures. *Journal of the Mechanics and Physics of Solids*, 136, 2020.

[79] M. J. French and M. B. Widden. The spring-and-lever balancing mechanism, george carwardine and the anglepoise lamp. *Proceedings of the Institution of Mechanical Engineers, Part C: Journal of Mechanical Engineering Science*, 214:501–507, 2000.

[80] D. N. Becker. Development of the chicago type bascule bridge. *Transactions of the American Society of Civil Engineers*, 109:995–1025, 1944.

[81] A. P. Thrall, S. Adriaenssens, I. Paya-Zaforteza, and T. P. Zoli. Linkage-based movable bridges: Design methodology and three novel forms. *Engineering Structures*, 37:214–223, 2012.

[82] W. Hamouche, C. Maurini, S. Vidoli, and A. Vincenti. Multi-parameter actuation of a neutrally stable shell: A flexible gear-less motor. *Proceedings of the Royal Society A: Mathematical, Physical and Engineering Sciences*, 473, 2017.

[83] T. Liu, S. Bi, Y. Yao, Z. Dong, Q. Yang, and L. Liu. Research on zero-stiffness flexure hinge (zsfh) based on spring four-bar linkage (4bsl). *Mechanism and Machine Theory*, 143:103633, 2020.

[84] A. Baumann, A. Sánchez-Ferrer, L. Jacomine, P. Martinoty, V. Le Houerou, F. Ziebert, and I. M. Kulić. Motorizing fibres with geometric zero-energy modes. *Nature Materials*, 17:523–527, 2018.

[85] J. P. Stacey, M. P. O'Donnell, and M. Schenk. Thermal prestress in composite compliant shell mechanisms. *Journal of Mechanisms and Robotics*, 11, 2019.

[86] M. Redoutey and E.T. Filipov. *Scientific Reports*, 2023. Accepted.

[87] M. Schenk and S. D. Guest. Geometry of miura-folded metamaterials. *Proceedings of the National Academy of Sciences of the United States of America*, 110:3276–3281, 2013.

[88] J. M. Gattas, W. Wu, and Z. You. Miura-base rigid origami: Parameterizations of first-level derivative and piecewise geometries. *Journal of Mechanical Design, Transactions of the ASME*, 135:1–11, 2013.

[89] T. Zegard and G. H. Paulino. Grand3 — ground structure based topology optimization for arbitrary 3d domains using matlab. *Structural and Multidisciplinary Optimization*, 52:1161–1184, 2015.

[90] M. Redoutey and E.T. Filipov. Programming stable motions in multi-dof systems. Submitted.

[91] V. Arakelian, J. P. Le Baron, and P. Mottu. Torque minimisation of the 2-dof serial manipulators based on minimum energy consideration and optimum mass redistribution. *Mechatronics*, 21:310–314, 2011.

[92] A. J. Koivo. Kinematics of excavators (backhoes) for transferring surface material. *Journal of Aerospace Engineering*, 7:17–32, 1994.

[93] L. Alegria Mira, R. Filomeno Coelho, A. P. Thrall, and N. De Temmerman. Parametric evaluation of deployable scissor arches. *Engineering Structures*, 99:479–491, 2015.

[94] W. Shan. Computer analysis of foldable structures. *Computers & Structures*, 42:903–912, 3 1992.

[95] A. Kaveh and A. Davaran. Analysis of pantograph foldable structures. *Computers & Structures*, 59:131–140, 4 1996.

[96] A. S. K. Kwan and S. Pellegrino. Matrix formulation of macro-elements for deployable structures. *Computers and Structures*, 1994.

[97] W. McGuire, R. H. Gallagher, and R. D. Ziemian. *Matrix Structural Analysis*. Wiley, 2nd edition, 2000.

[98] Y. Zhu and E. T. Filipov. Sequentially working origami multi-physics simulator (SWOMPS): A versatile implementation. *Proceedings of the ASME Design Engineering Technical Conference*, 8B-2021(December), 2021.

[99] K. Liu and G. H. Paulino. Nonlinear mechanics of non-rigid origami: An efficient computational approach. *Proceedings of the Royal Society A: Mathematical, Physical and Engineering Sciences*, 473, 2017.

[100] E. T. Filipov, K. Liu, T. Tachi, M. Schenk, and G. H. Paulino. Bar and hinge models for scalable analysis of origami. *International Journal of Solids and Structures*, 124:26–45, 2017.

[101] K. Liu and G. H. Paulino. Highly efficient nonlinear structural analysis of origami assemblages using the merlin2 software. *Origami*, 7:1167–1182, 2018.

[102] S. Huerta. Oval domes: History, geometry and mechanics. *Nexus Network Journal*, 9:211–248, 2007.

[103] R. Pedreschi and D. Theodossopoulos. The double-curvature masonry vaults of eladio dieste. *Proceedings of the Institution of Civil Engineers: Structures and Buildings*, 160:3–11, 2007.

[104] S. Pellegrino. A class of tensegrity domes. *International Journal of Space Structures*, 7:127–142, 1992.

[105] X. Yuan, L. Chen, and S. Dong. Prestress design of cable domes with new forms. *International Journal of Solids and Structures*, 44:2773–2782, 2007.

[106] T. Wulfrank, Y. Jurkiewicz, and E. Kahle. Design-focused acoustic analysis of curved geometries using a differential raytracing technique. *Building Acoustics*, 21:87–95, 3 2014.

[107] C. V. Girija Vallabhan and R. Panneer Selvam. A computer model for stress analysis of spherically curved solar panels. *Journal of Solar Energy Engineering, Transactions of the ASME*, 107:281–285, 1985.

[108] A. G. Tibert and S. Pellegrino. Deployable tensegrity reflectors for small satellites. *Journal of Spacecraft and Rockets*, 39:701–709, 2002.

[109] N. J.G. Fonseca, E. Girard, and H. Legay. Doubly curved reflector design for hybrid array fed reflector antennas. *IEEE Transactions on Antennas and Propagation*, 66:2079–2083, 2018.

[110] V. Pini, J. J. Ruz, P. M. Kosaka, O. Malvar, M. Calleja, and J. Tamayo. How two-dimensional bending can extraordinarily stiffen thin sheets. *Scientific Reports*, 6:1–6, 2016.

[111] W. S. Massey. Surfaces of gaussian curvature zero in euclidean 3-space. *Tohoku Mathematical Journal*, 1962.

[112] S. J.P. Callens and A. A. Zadpoor. From flat sheets to curved geometries: Origami and kirigami approaches. *Materials Today*, 21:241–264, 2018.

[113] C. D. Modes, K. Bhattacharya, and M. Warner. Gaussian curvature from flat elastica sheets. *Proceedings of the Royal Society A: Mathematical, Physical and Engineering Sciences*, 467:1121–1140, 2011.

[114] L. H. Dudte, E. Vouga, T. Tachi, and L. Mahadevan. Programming curvature using origami tessellations. *Nature Materials*, 15:583–588, 2016.

[115] F. Feng, X. Dang, R. D. James, and P. Plucinsky. The designs and deformations of rigidly and flat-foldable quadrilateral mesh origami. *Journal of the Mechanics and Physics of Solids*, 142:104018, 2020.

[116] E. D. Demaine, M. L. Demaine, V. Hart, G. N. Price, and T. Tachi. (non)existence of pleated folds: How paper folds between creases. *Graphs and Combinatorics*, 27:377–397, 2011.

[117] E. T. Filipov and M. Redoutey. Mechanical characteristics of the bistable origami hypar. *Extreme Mechanics Letters*, 25:16–26, 2018.

[118] T. Tachi. Origamizing polyhedral surfaces. *IEEE Transactions on Visualization and Computer Graphics*, 16:298–311, 2010.

[119] E. D. Demaine and T. Tachi. Origamizer: A practical algorithm for folding any polyhedron. *33rd International Symposium on Computational Geometry*, 77:1–16, 2017.

[120] A. G Martin. A basketmaker's approach to structural morphology. *Proceedings of the International Association for Shell and Spatial Structures*, 2015, 2015.

[121] Y. Cho, J. H. Shin, A. Costa, T. A. Kim, V. Kunin, J. Li, S. Yeon Lee, S. Yang, H. N. Han, I. S. Choi, and D. J. Srolovitz. Engineering the shape and structure of materials by fractal cut. *Proceedings of the National Academy of Sciences of the United States of America*, 111:17390–17395, 2014.

[122] H. Nakamura. *Karakuri Kamikara*. Nihon Bungeisha, 2016.

[123] J. P. Whitney, P. S. Sreetharan, K. Y. Ma, and R. J. Wood. Pop-up book mems. *Journal of Micromechanics and Microengineering*, 21, 2011.

[124] Y. Zhang, Z. Yan, K. Nan, D. Xiao, Y. Liu, H. Luan, H. Fu, X. Wang, Q. Yang, J. Wang, W. Ren, H. Si, F. Liu, L. Yang, H. Li, J. Wang, X. Guo, H. Luo, L. Wang, Y. Huang, and J. A. Rogers. A mechanically driven form of kirigami as a route to 3d mesostructures in micro/nanomembranes. *Proceedings of the National Academy of Sciences of the United States of America*, 112:11757–11764, 2015.

[125] J. Maker. Penguin paper bomb, 2017. https://jennifermaker.com/penguin-paper-bomb.

[126] Y. Zhu and E. T. Filipov. An efficient numerical approach for simulating contact in origami assemblages. *Proceedings of the Royal Society A: Mathematical, Physical and Engineering Sciences*, 475, 2019.

[127] T. Tarnai. Infinitesimal and finite mechanisms. *Deployable Structures*, pages 113–142, 2001.

[128] S. Pellegrino. on the rigidity of triangulated hyperbolic paraboloids. *Proceedings of The Royal Society of London, Series A: Mathematical and Physical Sciences*, 418:425–452, 1988.

[129] R. D. Kangwai and S. D. Guest. Detection of finite mechanisms in symmetric structures. *International Journal of Solids and Structures*, 36:5507–5527, 1999.

[130] C. V. Jutte and S. Kota. Design of nonlinear springs for prescribed load-displacement functions. *Journal of Mechanical Design*, 2008.